

TECHNISCHE UNIVERSITÄT MÜNCHEN

Lehrstuhl für Technische Physik  
E19 Interfaces and Energy Conversion

# **Scanning Probe Microscopy Analysis of New Battery Materials**

Maximilian P. B. Herpich

Vollständiger Abdruck der von der Fakultät der Physik  
der Technischen Universität München  
zur Erlangung des akademischen Grades eines  
Doktors der Naturwissenschaften (Dr. rer. nat.)  
genehmigten Dissertation.

Vorsitzender: apl. Prof. Dr. Norbert Kaiser  
Prüfer der Dissertation: 1. Prof. Dr. Ulrich Stimming  
2. Prof. Dr. Aliaksandr Bandarenka

Die Dissertation wurde am 09.01.2018 bei der Technischen Universität München  
eingereicht und durch die Fakultät für Physik am 05.02.2018 angenommen.



## Table of Contents

<b>1</b>	<b>Introduction</b>	<b>1</b>
<b>2</b>	<b>Fundamental Knowledge</b>	<b>5</b>
<b>2.1</b>	<b>Electrochemistry</b>	<b>5</b>
2.1.1	Definition of Fermi Level and Potentials	5
2.1.2	The Electrochemical Double Layer	8
2.1.3	Electrochemical Double Layer in Ionic Liquids	12
2.1.4	Electrode Reactions	16
<b>2.2</b>	<b>Electrochemical Methods</b>	<b>19</b>
2.2.1	Cyclic Voltammetry	20
2.2.2	Electrochemical Impedance Spectroscopy	20
<b>2.3</b>	<b>Scanning Probe Microscopy</b>	<b>22</b>
2.3.1	Scanning Tunneling Microscopy	23
2.3.2	Electrochemical Scanning Tunneling Microscopy	24
2.3.3	Scanning Electrochemical Potential Microscopy	25
2.3.4	Atomic Force Microscopy	26
<b>3</b>	<b>Materials and Experimental Setup</b>	<b>29</b>
<b>3.1</b>	<b>Microscope Setup</b>	<b>29</b>
3.1.1	Experimental Setup for EC-STM and SECPM	29
3.1.2	Tip Preparation	32
3.1.3	Experimental Setup for AFM and EC-AFM	33
<b>3.2</b>	<b>Electrochemical Impedance Spectroscopy</b>	<b>35</b>
<b>3.3</b>	<b>Materials</b>	<b>36</b>
3.3.1	Ionic Liquids	36
3.3.2	Polyoxometalates	38
3.3.3	HOPG	40
3.3.4	Au(111) Single Crystal	41
3.3.5	List of Materials	43
<b>4</b>	<b>Image Generation in SECPM</b>	<b>45</b>
<b>4.1</b>	<b>Influence of Parameter Variations</b>	<b>46</b>
4.1.1	Electrolyte Composition	46
4.1.2	Atomic Resolution	50
<b>4.2</b>	<b>Step Edge Oscillations</b>	<b>51</b>
4.2.1	Size and Shape	51
4.2.2	Influence of Measurement Parameters	53
4.2.3	Line Profile Analysis	57
<b>5</b>	<b>Influence of Water on the Double Layer Capacitance of an Ionic Liquid</b>	<b>63</b>
<b>5.1</b>	<b>Water in Ionic Liquids</b>	<b>63</b>
<b>5.2</b>	<b>Electrochemical Measurements</b>	<b>65</b>
5.2.1	Reference Electrode Stability	65
5.2.2	Cyclic Voltammetry	66
5.2.3	Electrochemical Impedance Spectroscopy	68
<b>5.3</b>	<b>Scanning Tunneling Microscopy</b>	<b>71</b>
<b>5.4</b>	<b>Mean Field Theory</b>	<b>73</b>
<b>5.5</b>	<b>Interpretation</b>	<b>75</b>
<b>6</b>	<b>Polyoxometalate Adsorption on HOPG</b>	<b>79</b>
<b>6.1</b>	<b>POM Interactions</b>	<b>79</b>
<b>6.2</b>	<b>Potential Dependence of POM Adsorption</b>	<b>83</b>

6.2.1	Comparison of $\text{Mn}^{\text{II}}\text{SiW}_9$ and $\text{Mn}^{\text{III}}\text{SiW}_9$ .....	83
6.2.2	Cyclic Voltammetry and AFM.....	84
6.2.3	In-situ Imaging of $\text{SiV}_3\text{W}_9$ .....	86
6.2.4	Cyclic Voltammetry .....	87
6.2.5	EC-AFM During Potential Steps.....	88
6.2.6	Ordered Linear Structures .....	91
<b>6.3</b>	<b>Influence of Electrolyte Composition and POM Charge .....</b>	<b>95</b>
6.3.1	Experimental.....	96
6.3.2	Different POMs .....	96
6.3.3	Different Solvents.....	98
6.3.4	Analysis of the Results .....	101
<b>7</b>	<b>Discussion and Conclusions .....</b>	<b>103</b>
7.1	Improving the Understanding of SECPM.....	103
7.2	Influence of Water on the Double Layer Capacitance of Ionic Liquids .....	105
7.3	POM Adsorption .....	105
7.4	Concluding Remarks.....	107
<b>8</b>	<b>Bibliography .....</b>	<b>109</b>
<b>Appendix.....</b>		<b>121</b>
A1	Abbreviations .....	121
A2	Symbols .....	123
A3	Publications .....	126
A4	Acknowledgements .....	127

# 1 Introduction

Energy storage is undoubtedly one of the most important current research areas, fueled by several rapidly growing fields of application. On the one hand, a gigantic new market for portable electronic devices has sprung up in the last decade, initiated by the remarkable success of smartphones. The resulting development of increasingly powerful mobile computer hardware led to the design of completely new product families from smart wearable devices such as watches and glasses to tablet computers. A common denominator for all these products is their requirement for small and light batteries. Therefore, their most important property is a high energy density. And because these devices are usually carried or worn almost continuously battery safety is another key factor.

On the other hand, the growing acceptance of the fact that the activities of humanity have an influence on global warming has instigated many countries to begin replacing CO<sub>2</sub> emitting fossil energy sources such as coal and gas with renewable sources such as solar, wind and water power. However, while conventional coal and nuclear power plants can deliver electricity continuously or, in case of gas, can be kept on stand-by, the electricity generation of renewable sources is much less constant and depends on mostly uncontrollable external factors. With their portion of the total generated electricity increasing, it is becoming important to store excess electricity when the generated amount exceeds the demand and to release it into the grid when the demand is higher. The requirements for batteries to store this energy are very different from the previous example. They have to be able to store large amounts of energy in one place and therefore, size and weight are generally not important factors. Cheaper batteries with a lower energy density can be employed. On the other hand, these storage solutions need a long lifetime over many charge-discharge cycles to reduce the cost of the stored energy. Because of the lower energy densities, safety is a less critical issue.

Another large contribution to CO<sub>2</sub> emissions comes from the combustion engines of most cars, planes, ships and other modes of transportation. Furthermore, several cities are beginning to ban certain types of cars from their centers to combat air pollution. A solution to both of these problems is a switch to electrically powered vehicles. While their numbers on the roads are still relatively small compared to conventional cars, the market has been growing steadily in recent years. A major shortcoming of the current generation is the still limited range before the battery needs to be recharged, combined with long charging times. To establish a viable alternative to combustion engines, the batteries must be improved in several areas. The most critical factor here is a high energy density, which

will increase the car's range. Safety, affordability, a long lifetime and short charging times are also significant factors.

When comparing these three examples, it becomes evident that each area of energy storage has very different requirements for batteries. It is questionable that a single ideal battery can be realized as the solution for all applications. Instead, highly specialized batteries must be developed that fulfill all requirements of a single type of application. To achieve this, improvements have to be made in electrode and electrolyte materials, which is only possible if their physical and electrochemical properties are understood on a fundamental level. While many different methods are available for an electrochemical analysis of these materials, they can usually only obtain general information about electrodes and electrolytes. However, many processes can only be fully understood when they are observed on a molecular scale. This is where *Scanning Probe Microscopy* (SPM) can show its strengths. SPM is a group of non-optical microscope techniques including the well-known *Scanning Tunneling Microscope* (STM) and *Atomic Force Microscope* (AFM) which are able to record images at sub-nanometer resolution. The technology was invented in 1982 by G. Binnig and H. Rohrer in the form of STM [1], for which they were awarded with the Nobel prize in 1986. Only few years later, Sonnenfeld and Hansma showed that the technique can also be performed in a liquid environment [2]. Their discovery soon paved the way for *Electrochemical STM* (EC-STM), where the transfer of microscope probe and sample into a small electrochemical cell allows in-situ measurements under full potential control [3]. Previously, all attempts of localized electrochemical measurements could only resolve much larger areas due to the size of the available electrodes and therefore were not able to analyze the surface in much detail. With the development of EC-STM, it became possible for the first time to directly observe the electrochemical processes, as they occur inside a battery, on a molecular or even atomic scale.

The aim of this work is to use these unique capabilities of electrochemical scanning probe microscopy, the combination of electrochemical measurements with high-resolution surface imaging, to investigate materials with promising properties for energy storage applications. After this introduction, important background information will be presented first, the fundamental knowledge necessary to understand the theoretical background and the experimental methods in chapter 2 and a description of the experimental setup and sample preparation as well as of the used materials in chapter 3. In chapter 4, different aspects of *Scanning Electrochemical Potential Microscopy* (SECPM) will be investigated, a variation of STM that records images by mapping potential differences in the sample's *Electrochemical Double Layer* (EDL, introduced in section 2.1.2) at the electrode-electrolyte interface to gain a better understanding of this powerful but not widely used experimental technique. The influence of trace amounts of water on the double layer capacitance of *Ionic Liquids* (ILs) will be analyzed in chapter 5 to analyze the

cause of contradicting reports [4], [5], using a combination of electrochemical impedance spectroscopy and electrochemical STM. Furthermore, in chapter 6 the adsorption behavior of a class of molecules called *Polyoxometalates* (POMs) will be analyzed thoroughly. The properties of POMs are highly tunable and they can undergo multiple redox reactions [6], [7], making them a promising candidate as charge carriers for energy storage applications. How the properties of POMs and of the electrolyte influence the adsorption will be analyzed with electrochemical AFM and AFM in air.



## 2 Fundamental Knowledge

Batteries store electric energy through electrochemical processes and therefore, research in this field consists largely of experiments in an electrochemical environment. This section will give a brief introduction into the fundamental electrochemical concepts and processes this work is based on. Because electrochemical SPM measurements take place inside the electrochemical double layer, located at the interface between sample and electrolyte, we will focus on the properties of that region and also introduce the experimental methods and provide the necessary theoretical knowledge to understand the results of the experiments.

### 2.1 Electrochemistry

#### 2.1.1 Definition of Fermi Level and Potentials

All electrochemical processes are the result of electric charges being transported between two electrodes through an electrolyte, driven by potential differences in the system. Electrolytes are solutions that conduct electronic charges through the movement of charged ions. In order to fully understand these processes and to *“bridge the gap between the terminology of solid state physics and electrochemistry”* [8], the concept of potentials must be introduced. The argumentation in this section will closely follow the work of H. Gerischer and W. Ekaradt [8] which helped to define the Fermi energy in electrolytes.

In an electronic conductor/metal, the Fermi energy  $E_F$  can be expressed through the work function  $W$ . It describes the minimum energy necessary to move an electron from its position in the bulk metal into a vacuum outside the conductor:

$$E_F = -W \quad (2.1)$$

It is possible to measure the work function directly with photoelectron emission experiments [9]. During its journey from bulk metal to vacuum, the electron has to pass a dipole barrier at the metal surface which is caused by a relaxation process that manifests itself in a different atomic spacing of the outermost atomic layers [10]. Therefore, the work function is generally composed of two parts [11], [12]. The first part describes the work needed to pass the dipole barrier  $\chi$  and the second part to overcome the chemical potential  $\mu_e$  of electrons in the bulk electrode material.

$$W = \mu_e + e\chi \quad (2.2)$$

Here  $e$ , is the electric charge of a single electron. The energy of the electron can be described by the electrostatic potential  $V_i$ . Using  $V_i$ , the Fermi energy can now be defined in relation to  $V_i(-\infty)$ , the energy of an electron in the conduction band of the bulk metal. After an increase from passing through the surface dipole layer, the energy becomes constant again once the electron reaches a larger distance from the surface. At this point, the energy is defined as  $V_i(+\infty)$  as is illustrated in Fig. 2.1. Because of the dipole layer, the vacuum level energy differs from  $V_i(+\infty)$  by  $e\varphi(z)$ , where  $\varphi(z)$  is called the *Galvani potential*. In absence of excess charges on the surface, the dipole layer contribution can be expressed as:

$$\chi = \varphi(-\infty) - \varphi(+\infty) \quad (2.3)$$

In conclusion, the Fermi energy can be expressed through the chemical potential and the Galvani potential, resulting in the electrochemical potential  $\bar{\mu}_e$ :

$$E_F = \mu_e - q\varphi \equiv \bar{\mu}_e \quad (2.4)$$

Here,  $\varphi$  is the actual Galvani potential and equals  $\chi$  in the absence of excess surface charges and  $q$  the electric charge, in this case  $q = e$ .

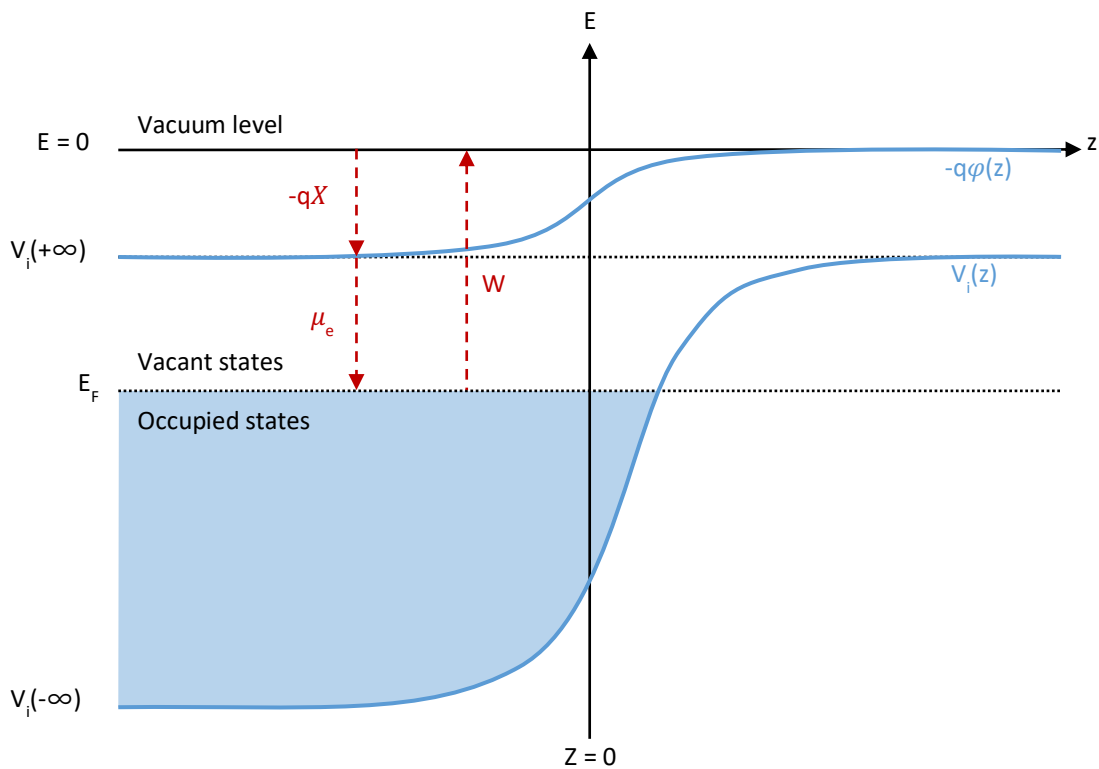


**Fig. 2.1:** Illustration of the energy levels of electrons at the interface between a conductor ( $z < 0$ ) and vacuum ( $z > 0$ ). The surface is assumed to have no excess charge. This image was adapted from [8].

In the case a redox electrolyte is used instead of a metal, the reduced and oxidized species have different chemical potentials. This also affects the expression for the Fermi energy, changing it to:

$$E_{F,redox} = \mu_{red} - \mu_{ox} - q\chi \quad (2.5)$$

Here,  $\mu_{red}$  and  $\mu_{ox}$  are the chemical potentials of the reduced and oxidized species and  $\chi$  the surface potential of the electrolyte. Alternatively, the Fermi energy can also be expressed through the ionization energy  $I$  and the free energies of solvation of the two species  $O$  and  $R$ , which incorporate all interactions with the solution.

$$E_{F,redox} = -I + O - R - q\chi \quad (2.6)$$

When the metal and the electrolyte are brought into contact with each other, a current will start to flow that causes their electrochemical potentials to shift until  $\bar{\mu}_e$  is constant across the interface. The exchange of charge between the two phases results in a difference between their electrostatic potentials. This so-called *Volta potential* difference  $\Delta U$  can be expressed as:

$$\Delta U = U_2 - U_1 = (W_2 - W_1)/q \quad (2.7)$$

If the surface dipoles are unaffected by the current flow and potential changes,  $\Delta U$  describes the relative change of the two Galvani potentials. Using the vacuum next to the surface as a reference point, the electronic states in the metal are shifted downward upon contact with the electrolyte. Therefore, it can be concluded that it is possible to measure the Fermi level in the electrolyte if the difference in Volta potentials at equilibrium and the work function of the metal are known:

$$E_{F,redox} = -W_m - q(U_m - U_e) \quad (2.8)$$

The subscripts  $m$  and  $e$  stand for metal and electrolyte respectively. Above considerations allow the definition of an experimentally determinable absolute scale of electrode potentials with a point in vacuum as reference, as suggested by B. Trasatti et al. [13]. However, from an experimental point of view it is generally not practical to employ an in-vacuum reference point for measuring potentials. Therefore, in most experiments a *reference electrode* (RE) is used instead. These are electrodes that are specifically designed to possess a well-known and stable potential which is often realized by the means of a redox system with constant concentrations of each component [14]. While there are many different types of reference electrodes, a widely used potential scale has been established, based on the hypothetical *standard hydrogen electrode* (SHE) through which potentials for all other reference electrodes can be defined. Its absolute potential (vs. the vacuum state) is estimated to be located around  $-4.43$  V [15]. The SHE consists of a platinized sheet that is immersed in an acid containing exactly  $1$  M of  $H^+$  ions with unit

activity ( $pH = 0$ ) and is continuously flushed with Hydrogen gas with a pressure of  $1 \text{ bar}$  [16]. The defining electrode reaction is:



However, it is common practice in most publications to state potentials against the *normal hydrogen electrode* (NHE) as a reference instead. The NHE is an experimentally realizable variation of the SHE. Its potential  $U_0$  is slightly shifted from the SHE due to unavoidable interactions of  $H^+$  with other ions. This changes the activity of the  $H^+$  ions to approximately  $0.8$  [16].

### 2.1.2 The Electrochemical Double Layer

As explained in section 2.1.1, when a conducting electrode is immersed into an electrolyte, a current begins to flow between them to establish a constant electrochemical potential across the interface. Because of the resulting Volta potential difference  $\Delta U$  (for simplicity from here on referred to as  $U$ ), electric charges accumulate at the electrode surface. This charge is compensated by ions of opposite polarity accumulating at the electrolyte side of the interface. In 1853, H. von Helmholtz used the analogy of a plate capacitor to describe this effect and named it the *electrochemical double layer* [17]. In his model, the charged electrode surface forms one plate of the capacitor and the layer of accumulated ions in the electrolyte the other. Treating the ions as point charges, he expressed the differential double layer capacitance  $C_{DL}$ , in this model referred to as *Helmholtz capacitance*  $C_H$ , with the total stored charge  $q$  as:

$$C_{DL} = C_H = \frac{dq}{dU} = \frac{\varepsilon A}{d} \quad (2.10)$$

$C_H$  is directly proportional the electrochemically active surface area  $A$  and the effective dielectric constant of the electrolyte  $\varepsilon = \varepsilon_0 \varepsilon_r$ , where  $\varepsilon_0$  is the dielectric permittivity of free space and  $\varepsilon_r$  the specific dielectric constant of the electrolyte. Also,  $C_H$  is inversely proportional to the distance  $d$  between surface and ionic layer which can be approximated from the radii of the ions, including their solvation shell of water molecules.

While the Helmholtz model provides a useful template for the understanding the basic concept of the electrochemical double layer, it has several critical flaws when it comes to describing real systems. For instance, thermal disorder prevents the EDL from forming a single, two-dimensional monolayer and causes it to extend in z-direction, away from the interface. Also,  $C_H$  was found to vary with changes in electrode potential and ion concentration. L. Gouy [18] and D. Chapman [19] realized that instead of the rigid ionic layer proposed by Helmholtz, the solvated ions form an extended *diffuse layer* that reaches from the surface into the bulk electrolyte with decreasing density. These

*nonspecifically adsorbed* ions are interacting with the charged surface exclusively through long-ranged electrostatic forces and are still treated as point charges.

The diffuse layer forms because of interactions between electrostatic forces, thermal motion and diffusion. The latter is caused by a lower concentration of ions in the bulk electrolyte than at the interface and distributes the counterions over a three-dimensional region within the electrolyte. Because the model of a simple plate capacitor is no longer valid here, a new formalism for  $C_{DL}$  must be established. We begin with the charge density in the electrolyte  $\sigma$  at a distance  $x$  from the interface. It follows a Boltzmann distribution [14]:

$$\sigma(x) = \sum_i c_i n_i e \exp\left(\frac{-n_i e U(x)}{k_B T}\right) \quad (2.11)$$

In this equation,  $c_i$  is the bulk concentration of ionic species  $i$ ,  $n_i$  its charge in multiples of the electronic charge  $e$ ,  $k_B$  the Boltzmann constant and  $T$  the absolute Temperature. At large distances from the interface,  $U = 0$  and  $dU/dx = 0$ . Therefore, equation ( 2.11 ) combined with the Poisson equation yields the important Poisson-Boltzmann equation which describes the behavior of the system as [14]:

$$\left(\frac{dU}{dx}\right)^2 = \frac{2k_B T}{\varepsilon} \sum_i c_i \left[ \exp\left(\frac{-n_i e U}{k_B T}\right) - 1 \right] \quad (2.12)$$

In the case of a symmetrical electrolyte where  $n_1 = -n_2 = n$  and  $c_1 = c_2 = c_0$ , the Poisson-Boltzmann equation can be simplified to:

$$\frac{dU}{dx} = -\sqrt{\frac{8k_B T c_0}{\varepsilon}} \sinh\left(\frac{neU}{2k_B T}\right) \quad (2.13)$$

Using the Gauss law and integrating over the whole electrode surface, the total charge  $q$  in the diffuse layer can be expressed as:

$$q = \varepsilon A \left(\frac{dU}{dx}\right)_{x=0} \quad (2.14)$$

Substituting from equation ( 2.13 ) and using the charge density in solution  $\sigma_s = -\sigma_M = q/A$  with  $\sigma_M$  being the charge density in the metal, it can be concluded for the Gouy-Chapman capacitance of the diffuse layer  $C_{GC}$  [14]:

$$C_{GC} = \frac{d\sigma_M}{dU} = \sqrt{\frac{2(ne)^2 \varepsilon c_0}{k_B T}} \cosh\left(\frac{neU}{2k_B T}\right) = \varepsilon \kappa \cosh\left(\frac{neU}{2k_B T}\right) \quad (2.15)$$

Here,  $\kappa$  is the inverse of the Debye length  $\lambda_D$  which describes the characteristic thickness of the diffuse layer and is defined as:

$$\lambda_D = \kappa^{-1} = \sqrt{\frac{\epsilon k_B T}{2c_0(ne)^2}} \quad (2.16)$$

Therefore, the width of the diffuse layer increases when the ion concentrations in the electrolyte are lowered. Even though the *Gouy-Chapman* (GC) model is an important improvement compared to the original Helmholtz model, it has one critical flaw. With increasing potential,  $C_{GC}$  would rise towards infinity, a direct consequence of describing the ions as point charges. The resulting capacitance vs. potential curve assumes a typical U-shape (Fig. 2.2). In this unrealistic scenario, the distance between ions and surface would decrease towards zero at high potentials.

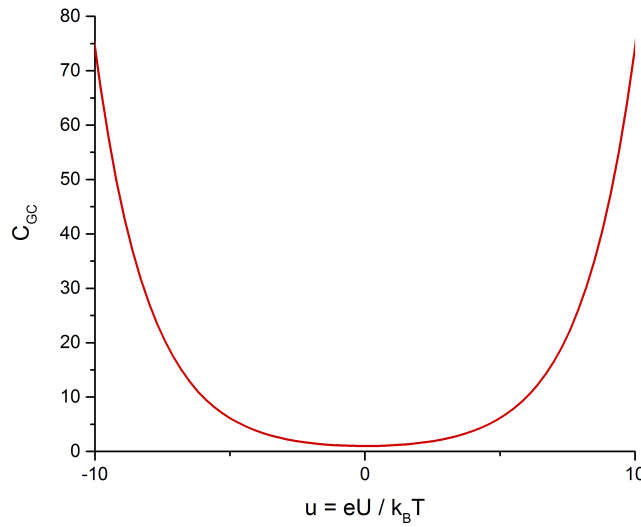


**Fig. 2.2:** Normalized  $C_{DL}$  vs. potential curve in the GC model, calculated from eq. ( 2.15 ) in arbitrary units. The graph shows that the double layer capacitance would start increasing towards infinity at higher potentials.

To address this issue, O. Stern refined the GC-model by treating the electrolyte side of the double layer as two separate regions [20]. His formalism merges the idea of a rigid ionic layer at the interface from the Helmholtz model with the diffuse layer suggested in by Gouy and Chapman. The resulting formalism is commonly referred to as the *Gouy-Chapman-Stern* (GCS) model. The two ionic layers can be treated as two capacitors in series and the total double layer capacitance  $C_{DL}$ , now called the *Gouy-Chapman-Stern capacitance*  $C_{GCS}$  can be expressed as:

$$C_{DL} = C_{GCS} = \frac{1}{C_H} + \frac{1}{C_{GC}} \quad (2.17)$$

The ions in the rigid first ionic layer are no longer treated as point charges and are assigned a finite size instead. The assumed ion size not only includes the diameter of the ion itself

but also its solvation shell of water molecules that become attached to it due to their polar nature. The smallest possible distance  $x_2$  of the centers of these solvated ions from the electrode surface defines the so called *Outer Helmholtz Plane (OHP)* [21]. David Grahame proposed that a layer of polarized solvent molecules (e.g.  $H_2O$ ) is located between the OHP and the electrode surface, in direct contact with the latter. It also contains small amounts of ions that have (partially) shed their solvation shells [22]. The plane defined by the centers of these *specifically adsorbed ions*, at a distance  $x_1$  from the surface, is known as the *Inner Helmholtz Plane (IHP)*. At distances larger than  $x_2$ , the diffuse layer of the Gouy-Chapman model is used to describe the system.

While there are many extensions and additions to the GCS model, it defines a commonly used basis for the description of the molecular structure and the according potential profile of the EDL. An illustration is shown in Fig. 2.3. While the GCS model already provides a sufficiently accurate description of the EDL in many dilute electrolyte systems, several aspects that can still be refined and improved. Factors such as the dielectric structure within the Helmholtz planes and its full polarization in the strong electric fields that exist near the surface at high potentials, different values of  $x_2$  for anions and cations as well as ion-ion interactions can influence the double layer structure and its capacitance.

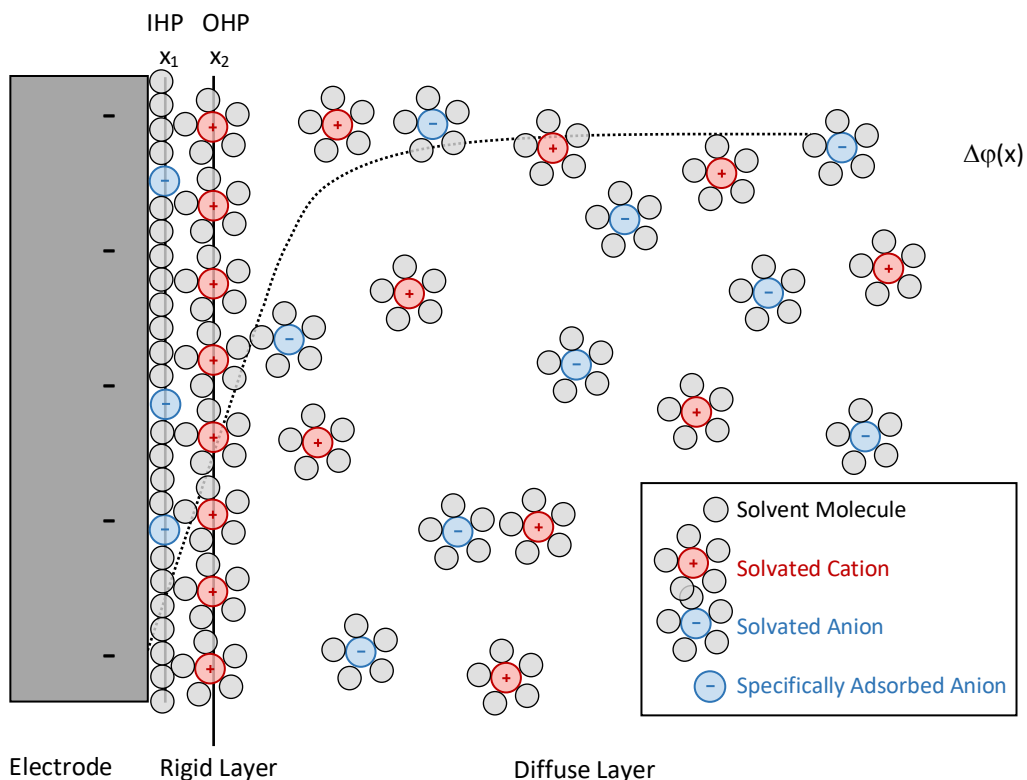


**Fig. 2.3:** Illustration of the molecular structure and potential distribution inside the EDL, according to the GCS model. The dotted curve represents the potential vs. distance from the surface. The image was adapted from [14].

An important value for the description of the EDL is the so-called *Potential of Zero Charge* (PZC), sometimes also referred to as *Point of Zero Charge*. It marks the transition between positive and negative electrode polarization. At the PZC, the electrode surface is free of excess charges and therefore does not attract or repulse the cations and anions in the electrolyte. Therefore, the double layer capacitance is at a minimum here. An example for this effect can be seen in Fig. 2.2.

### 2.1.3 Electrochemical Double Layer in Ionic Liquids

Ionic liquids, more accurately also sometimes referred to as *Room Temperature Ionic Liquids (RTILs)*, consist completely of ions. Because of the high concentration of ions, the absence of solvents and the comparatively large size of the individual ions, the GCS model fails to correctly describe the EDL structure of ionic liquids. However, since the intrinsic properties of ILs make them a promising alternative to conventional electrolytes in many electrochemical applications, it is crucial to understand the processes and structure of their EDL. The description in this section mostly follows the comprehensive review of ionic liquids at electrified interfaces by M. Fedorov and A. Kornyshev [23].

Since the early 2000s, much attention has been given to the topic and has led to a good basic understanding of their EDL. A first simple approach was made using mean field theory, describing the system with a lattice gas model at a flat, metallic interface [24]. An important finding of this model was that the distribution of anions and cations as a function of the electrostatic potential depends on the so called *compacity parameter*  $\gamma$ . The compacity is defined as the ratio of the average ion concentration in the neutral region  $c_0$ , far away from the interface to their highest possible concentration  $c_{max}$ , which is generally limited by the ion size.

$$\gamma = \frac{2c_0}{c_{max}} \quad (2.18)$$

It describes the amount of available space within the ionic liquid that could theoretically be filled with more ions. The addition of water or organic solvents decreases  $\gamma$ , which equals 1 in a hypothetical maximally dense IL. In the unrealistic limiting case of  $\gamma = 0$ , the potential distribution  $\varphi(x)$  within the EDL would follow the curve defined by the GC model. For higher values of  $\gamma$ , around  $\gamma = 1/2$  is a realistic estimate for many ILs, the potential decreases more slowly with  $x$ . This is caused by the counterions approaching maximum density near the interface. Therefore, their distribution begins to extend over a larger distance from the surface to counter the surface charge, an effect known as *crowding* or *lattice saturation*. Crowding has a strong influence on the potential dependence of the differential capacitance [25], [26]:

$$C_{DL} = C_{Debye} \cosh\left(\frac{u}{2}\right) \frac{1}{1 + 2\gamma \sinh^2\left(\frac{u}{2}\right)} \sqrt{\frac{2\gamma \sinh^2\left(\frac{u}{2}\right)}{\ln [1 + 2\gamma \sinh^2\left(\frac{u}{2}\right)]}} \quad (2.19)$$

with the Debye capacitance  $C_{Debye}$ , the Debye length  $\lambda_D$  and the potential drop expressed through the thermal voltage  $u$ :

$$C_{Debye} = \frac{\varepsilon_*}{4\pi\lambda_D}, \lambda_D = \sqrt{\frac{\varepsilon_* k_B T}{2c_0 (ne)^2}}, u = \frac{eU}{k_B T} \quad (2.20)$$

In contrast to the formalism for dilute electrolytes introduced in section 2.1.2, the high frequency dielectric constant  $\varepsilon_*$  is used here instead of the effective dielectric permittivity  $\varepsilon$ . The first two factors of eq. ( 2.19 ) are equivalent to the Gouy-Chapman capacitance  $C_{GC}$ . The remaining two factors change the voltage dependence of the capacitance drastically. Instead of the U-shaped capacitance-voltage curve of the GC model from Fig. 2.2, the capacitance now decreases at high electrode polarizations. The behavior at small and medium voltages depends on the value of  $\gamma$ . For  $\gamma > 1/3$ , the capacitance curve has a single maximum around the PZC and therefore is usually referred to as a bell shape curve. Interestingly, for  $\gamma < 1/3$ , the capacitance has a minimum at the PZC instead that is located between two maxima. Due to its appearance with two peaks, this plot is generally referred to as *camel shape* curve [24]. Fig. 2.4 shows capacitance vs. potential curves calculated with eq. ( 2.14 ) for different values of  $\gamma$ . The change from bell- to camel-shape is clearly visible.

The camel shape is the result of a combination of the effects causing the U- and bell-shaped behaviors. At small voltages, the ion density in the EDL grows when  $U$  is increased because the compacity is relatively small. Therefore, the counter-ions can occupy empty space or replace solvent molecules that are shifted away from the interface which increases the double layer capacitance [27]. The two maxima and the following decrease of capacitance occur at potentials further from the PZC, when the IL reaches the maximum density near the surface and is in the state of lattice saturation. Any counterion reaching the interface when the potential is further increased must end its approach at greater distance from the electrode. This increases the EDL's thickness and in consequence causes its capacitance to decrease. In reality, the critical value between bell and camel shape is not always exactly 1/3 and depends on intrinsic properties of IL and electrode [25], [27]. In most ILs, the cations are significantly larger than the anions and should therefore possess a lower  $c_{max}$  [24], [28]. According to eq. ( 2.18 ), this results in different values for  $\gamma$  at negative and positive electrode polarizations with a higher  $\gamma$  on the negative side.

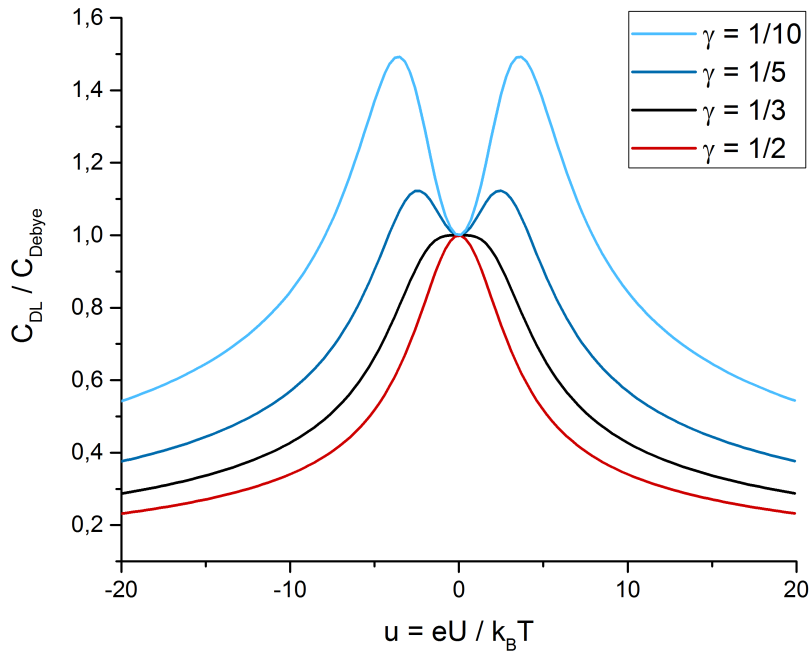


**Fig. 2.4:** Double layer capacitance vs. voltage curves of an ionic liquid, calculated with eq. ( 2.19 ) for different values of the compacity parameter  $\gamma$ . When  $\gamma > 1/3$ , the curve assumes a bell-shape (red), for  $\gamma < 1/3$  the so-called camel-shape (blue). An intermediate shape is found at  $\gamma = 1/3$  (black).

This asymmetry can be implemented into the EDL model by attributing a voltage dependence to the compacity:

$$\gamma(u) = \gamma_- + \frac{\gamma_+ - \gamma_-}{1 + e^u} \quad (2.21)$$

The adjustment of  $\gamma$  has two distinct effects on the appearance of the capacitance vs. potential curves. On the one hand, all minima and maxima are shifted to more positive potentials. On the other hand, differences between the positive and negative wing of the curve emerge. The positive side now has an overall higher capacitance than the negative side. It has to be noted that the presence of even small amounts of solvent in the IL drastically decreases its compacity and therefore also has a strong direct influence on the capacitance. Fig. 2.5 shows calculated capacitance curves from eq. ( 2.19 ), adjusted with the potential dependent  $\gamma(u)$  from eq. ( 2.21 ).

The adjusted capacitance curves show the expected asymmetry between positive and negative wing when different sizes for cation and anion are assumed. In the case of the dark blue curve, where  $\gamma_+ = \gamma_-$ , the curve again assumes the symmetric shape of the unadjusted system with a constant value of  $\gamma = 0.2$ . The red curve shows that, if both  $\gamma_+$  and  $\gamma_-$  are larger than 0.3, the camel-shape changes into an asymmetric version of the bell-

shaped curve. Both bell and camel shaped capacitance curves have been reported from experiments on the EDL structure in several ionic liquids. However, it is difficult to use these results to verify the theoretical models because, due to the varying and complicated ion shapes, the compacity parameter of the ionic liquids cannot be obtained or even reliably estimated [39]. It has also been found that changes in the atomic structure of the electrode surface and the adsorption of ions can strongly influence the measured double layer capacitance [40].

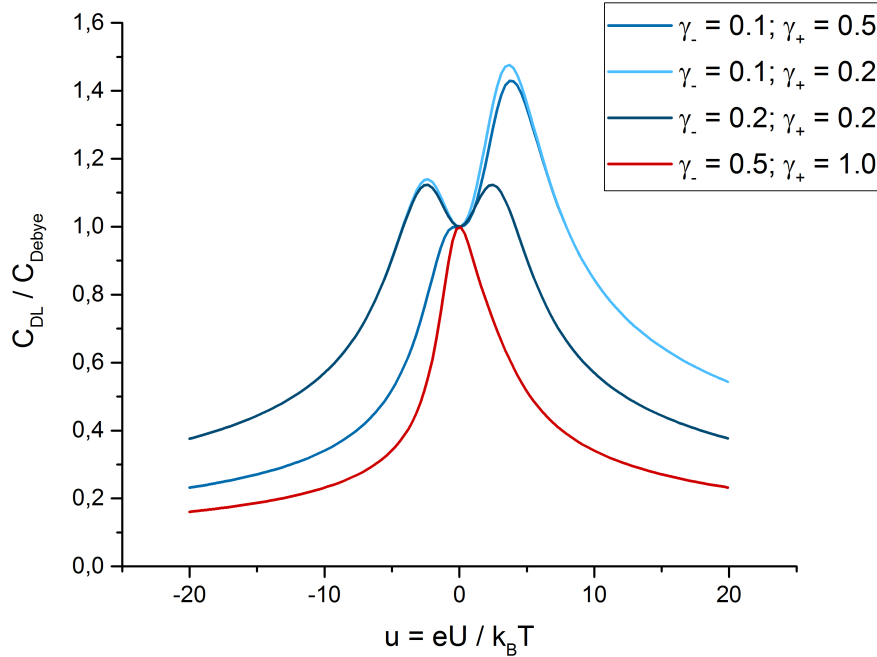


**Fig. 2.5:** Double layer capacitance vs. voltage curves of an ionic liquid, calculated with eq. ( 2.19 ). The model has been adjusted with a potential dependent  $\gamma(u)$  from eq. ( 2.21 ) and different values of  $\gamma$  for cations and anions.

This simple mean field model, while providing a good qualitative description of the double layer structure, does not take into account more complicated effects such as multibody correlations between the ions, their molecular structures as well as geometry and material composition of the electrode. Computer simulations are better suited to implement those factors and show a strong dependence of the double layer structure on the ion size and on the addition of solvents or another ionic liquid. The simulations also predict a structure of ionic layers close to the electrode surface that can extend several nanometers into the electrolyte at lower potentials [29], [30] which was not predicted by the mean-field model. It is called *overscreening* and is known from dipolar liquids such as water [31]–[33] and high temperature molten salts [34] and has also already been observed experimentally [35], [36]. The layered ion structure is created because the first layer of ions overcompensates for the charge of the electrode, resulting in a net charge that causes a second ion layer of opposite sign to assemble beyond it. This again

overcompensates for the net charge of the combination of electrode and first ionic layer, continuing for several layers of decreasing charge until the bulk electrolyte state is reached. At higher electrode polarizations, the layers disappear as the structure is reorganized once the lattice saturation effect takes over [37]. The exact structure of the ionic layers depends on the ion shape. Especially long organic tails that are often part of IL-cations were found to play an important role. While ions with shorter tails form the alternating cation-anion monolayer structure described above, it was discovered that ions with longer alkyl chain lengths rather accumulate in a bilayer structure [38].

In a publication in 2013, by Gebbie et al. [109] found “*that pure ionic liquids are expected to behave as dilute weak electrolyte solutions, with typical effective dissociated ion concentrations of less than 0.1% at room temperature*”, using direct surface force measurements and thermodynamic arguments. This has recently sparked a discussion about the dependence of the screening length on the ion concentration which also affects the understanding of the EDL structure in ionic liquids. It has for instance been suggested that the charges are transported by solvent molecules instead of ions [110] or that the formation of large ion clusters limits the number of free ions available for screening the electrode charge [111], both resulting in a much flatter potential curve than in an environment of mainly dissociated ions. This discussion is still ongoing and no final conclusions have been made yet.

#### 2.1.4 Electrode Reactions

Electrode reactions are electrochemical processes in which an electron is transferred across the interface between an electrode and a chemical species in the electrolyte. The equations and theories presented here provide the basis for many electrochemical experimental methods. In the following, we will use a simple example to describe the physical and chemical processes involved. An electrode is immersed into an electrolyte that contains a redox species  $S$  in its oxidized form  $Ox$  and its reduced form  $Red$ . The electrode reaction that converts one form to the other through a transfer of  $n$  electrons can then be expressed as:



When examined in more detail, three steps are necessary to complete the reaction. In the case of  $Ox$  being converted into  $Red$ , in the first step, the reagent  $Ox$  must be transported from its position in the electrolyte to the electrode surface where the electron transfer can take place. In the second step, an electron is transferred from the electrode to  $Ox$ , reducing it to  $Red$ . Finally, in the third step of the reaction, the product  $Red$  is transported away from the surface. In other, more complicated reactions, different reaction steps such as coupled chemical reactions and adsorption on the electrode surface can also play a role. The rate at which the reaction takes place is determined by its slowest step. In this

simple case, this can be either the electron transfer or the mass transport to/from the reaction site. Generally, mass transport is the result of a combination of three types of particle motion [14]:

- *Diffusion*: The motion of particles under the influence of a concentration gradient. This effect occurs when the electron transfer changes the concentrations of *Ox* and *Red* at the interface in relation to their bulk concentrations.
- *Migration*: The gradient of an electric field, for example of the charged electrode, exhibits a Coulomb force on charged particles in the electrolyte.
- *Convection*: The motion of the whole fluid. This can be the result of temperature or density gradients within the electrolyte or external mechanical forces such as stirring.

However, in controlled reaction environments, the influence of migration and convection can generally be controlled and therefore ignored. The only influence on the reaction that has to be taken into account is diffusion. The first quantum-mechanical descriptions of the electron transfer process were developed starting in the 1950s by R. A. Marcus, R. Dogonadze, V. G. Levich and others [41]–[45]. These models are based on the Franck-Condon principle which states that, because electron transfer can be considered instantaneous compared to nuclear motion, it takes place via vertical transitions between nuclear vibrational states [46], [47]. In terms of a redox reaction, the transition must occur between local minima of the Gibbs free energy of reduced and oxidized states. Between the two minima, a maximum must exist. In classical terms, the maximum describes the activation energy  $E_a$  that the electron must overcome [14]. From a quantum-mechanical perspective, the situation can be described as an energy barrier that the electron can pass by tunneling.

At this point, we revisit the case described in section 2.1.1, where a current starts to flow after electrode and electrolyte are brought into contact to establish a constant electrochemical potential across the interface. Given enough time, the potential difference stabilizes at  $U_0$  and the current flow diminishes. However, this is only true for the net current, the forward and backward reactions now simply have reached an equilibrium and compensate each other. The current  $I_0$  of either one of these half-reactions is known as the *exchange current*. Normalized by the concentration of the redox species (for equal concentrations of *Ox* and *Red*) and the electrode area  $A$ , it yields the electron transfer constant  $k_0$ :

$$k_0 = \frac{I_0}{nFAc} \quad (2.23)$$

Here,  $F$  is the Faraday constant and  $n$  the number of transferred electrons. For a system at equilibrium, where no net current flows, the relation between  $U_0$  and the concentrations  $c$  or activities  $a$  of the redox couple is established through the chemical potentials by the Nernst equation [48]:

$$U_0 = U^\theta + \frac{RT}{nF} \ln \left( \frac{c_O}{c_R} \right) = U^\theta + \frac{RT}{nF} \sum_j n_j \ln a_j \quad (2.24)$$

In this equation,  $U^\theta$  is the characteristic standard potential of the redox couple, a value that can be found in literature for most common redox reactions [49],  $a_j$  is the activity of species  $j$  and  $R$  the gas constant. If an external potential is applied to the system or the equilibrium is disturbed in another way, a current  $I$  flows through the interface and its potential  $U$  will shift from  $U_0$ . The resulting potential difference is called *overpotential*  $\eta$ :

$$\eta = U - U_0 \quad (2.25)$$

A positive overpotential decreases the Fermi level in the electrode, allowing electrons to transfer from occupied states of *Red* in the electrolyte into unoccupied states in the electrode and vice versa for negative potentials (illustrated in Fig. 2.6).

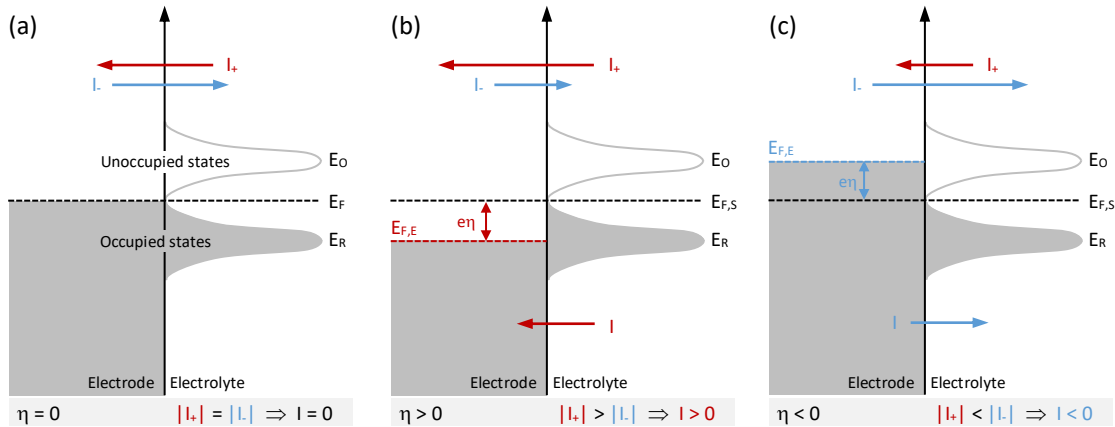


**Fig. 2.6:** Illustration of the energy levels in electrode and electrolyte when different overpotentials are applied. The exchange currents are shown at the bottom of each image. **(a)** No overpotential, **(b)** positive (anodic) overpotential and **(c)** negative (cathodic) overpotential.  $E_{F,S}$  and  $E_{F,E}$  are the Fermi energies in solution and electrode. This graph was adapted from [48].

When the overpotential is increased further, at a certain point the current will reach a limiting value. The reaction is now consuming all reactants as soon as they reach the surface and the reaction rate becomes limited by the speed of mass transport in the electrolyte. If the reaction is kept in the kinetic regime, below this region, mass transport has no impact on the reaction rate. In this case, the correlation between net current and overpotential is defined by the Butler-Volmer equation:

$$I = I_0 \left[ \exp\left(\frac{\alpha_a n F}{RT} \eta\right) - I_0 \exp\left(-\frac{\alpha_c n F}{RT} \eta\right) \right] \quad (2.26)$$

where  $\alpha_a$  and  $\alpha_c$  are the anodic and cathodic transfer coefficients with values between 0 and 1. They are a measure for the symmetry of the potential barrier between the two states of the redox couple. Under certain conditions, the Butler-Volmer equation can be simplified. For very small overpotentials an approximation can be made using the Taylor expansion, where  $e^x \approx 1 + x$ , changing eq. ( 2.26 ) into:

$$I = I_0 \frac{(\alpha_a + \alpha_c) n F}{RT} \eta \quad (2.27)$$

Here, the ratio  $\eta / I = R_{ct}$  is the so-called *charge-transfer resistance*. For high positive overpotentials, the cathodic side of the Butler-Volmer equation becomes negligible and can be omitted:

$$I = I_0 \exp\left(\frac{\alpha_a n F}{RT} \eta\right) \quad (2.28)$$

Accordingly, for high negative overpotentials only the anodic part of the Butler-Volmer equation is relevant:

$$I = -I_0 \exp\left(-\frac{\alpha_c n F}{RT} \eta\right) \quad (2.29)$$

The solutions for high overpotentials are known as the Tafel equations and can be used to determine the electron transfer coefficient  $k_0$  and the exchange current  $I_0$ .

## 2.2 Electrochemical Methods

All electrochemical measurements were performed in a three-electrode cell. Technically, in EC-STM and SECPM the microscope tip can be considered as a fourth electrode, but due to its much smaller surface area the general description of a three-electrode cells still applies. All reactions of interest take place at the sample surface which is called the *working electrode* (WE). Its potential is measured against a reference electrode that has a defined and stable potential (as described in section 2.1.1). Finally, a *counter electrode* (CE) is employed to pass the current flowing through the cell. The goal of this setup is to reduce the current flowing through the reference electrode, ideally to 0, to bring it as close as possible to the state of an ideal nonpolarized electrode. To achieve this, the counter electrode is placed close to the working electrode and possess a large surface area compared to the reference electrode.

### 2.2.1 Cyclic Voltammetry

Cyclic voltammetry is a commonly used method for a first characterization of an electrochemical system. Not only does it provide a good overview of processes occurring at the electrode, it also helps with the determination of more complicated reactions. These include coupled homogeneous reactions, adsorption on the electrode surface and multi-step processes [14], [21]. Starting from an initial potential  $U_0$ , generally located in a region where no reactions take place, the potential is linearly increased at a sweep rate  $\nu$  up to a vertex point  $U_1$  and then reversed to a second vertex point  $U_2$  and finally reversed again back to  $U_0$ . The current response of the system is recorded and plotted in an  $I$  vs.  $U$  curve known as *Cyclic Voltammogram* (CV). If reactions occur in the potential range between  $U_1$  and  $U_2$  under the applied conditions, the increased current results in peaks in the CV. By observing the changes in peak shape, size, position and number when parameters such as  $U_1$ ,  $U_2$ ,  $\nu$ , concentration of the redox couple and pH of the electrolyte are varied, information about the reaction mechanisms and kinetics as well as surface characteristics of the working electrode can be extracted.

### 2.2.2 Electrochemical Impedance Spectroscopy

The behavior of an electrochemical system in response to small perturbations from equilibrium depends on the frequency of the perturbation and thus cannot be described by an ohmic resistance. Instead, the concept of impedance must be applied. It uses a complex resistance  $Z = Re(Z) + i Im(z)$  with the imaginary number  $i = \sqrt{-1}$  to for a realistic description of the. For the limiting case of zero frequency, the impedance equals the ohmic resistance. In *Electrochemical Impedance Spectroscopy* (EIS), this concept is used to gather information about the double layer capacitance  $C_{DL}$  and the charge transfer resistance  $R_{CT}$  of an electrochemical system. In EIS, the potential of the working electrode is modulated using a sine wave or another periodical signal with varying frequency  $f$ . The signal amplitude is kept small, generally 10 mV or less, to achieve a pseudo-linear response. This allows to disregard harmonic generation and frequency mix products [50]. However, EIS only returns reliable results when the system under study fulfills two conditions. The redox species in the electrolyte must be in an equilibrium state with the ideal case of  $C_{ox} = C_{red}$  and the *Open Circuit Potential* (OCP)  $U_{OCP}$  must be equal to  $U_0$ . Also, the dispersion of the double layer capacitance should be small, which can be achieved by using flat and non-porous working electrodes [51].

An equivalent circuit in the form of electrical elements such as resistors and capacitors is used to create a model of the examined electrochemical system. From this circuit, the double layer capacitance and other values can be calculated. A simple example for an equivalent circuit, describing the system of a single electrochemical reaction at a flat electrode surface, contains a parallel combination of the double layer capacitance  $C_{DL}$  and

the charge transfer resistance  $R_{CT}$ , in series with an ohmic part  $R_{Ohm}$ . Another commonly used component in EIS equivalent circuits is the so called *Constant Phase Element* (CPE), a special case of a complex impedance that has a phase angle independent of frequency. It is the result of a current density distribution on inhomogeneous electrode surfaces [52]. More realistic circuits can quickly become much more complex, depending on the reactions and effects contributing to the measured current. For the proposed simple equivalent circuit, the total impedance can be expressed as:

$$Z = R_{Ohm} + \frac{R_{CT}}{1 + i 2\pi f R_{CT} C_{DL}} \quad (2.30)$$

By fitting experimental curves to suitable equivalent circuits, values for  $R_{CT}$ ,  $R_{Ohm}$  and  $C_{DL}$  can be calculated. For the analysis of experimental data, a commonly used representation of the results is the *Nyquist diagram* [50], where  $-Im(Z)$  is plotted against  $Re(Z)$ . Several Nyquist plots, calculated from eq. (2.30) for different values of the three circuit elements  $R_{Ohm}$ ,  $R_{CT}$  and  $C_{DL}$ , are shown in Fig. 2.7.

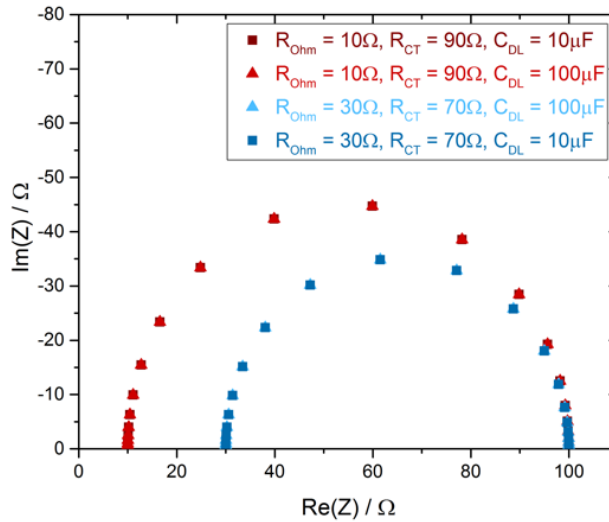


**Fig. 2.7:** Nyquist diagram of calculated curves with different values of  $R_{CT}$ ,  $R_{Ohm}$  and  $C_{DL}$ , using eq. (2.30). The two curves of the same color (red/blue) differ from each other in double layer capacitance but show no difference in the Nyquist plot.  $R_{CT}$  can be extracted from the width of the semicircle and  $R_{Ohm}$  from its the distance of from the origin.

Each point in the semicircular graph represents the measured impedance at one frequency. The second term of  $Z$  approaches  $R_{CT}$  for very low frequencies and 0 for very high ones, the latter because the double layer does not become fully charged before the current direction is reversed. Therefore, the width of the semi-circle directly shows the charge transfer resistance  $R_{CT}$  while the distance of the first data point from the origin equals  $R_{Ohm}$ . At frequencies between these two limiting cases, the imaginary part  $Im(Z)$  becomes relevant. However, the curve gives no information about the exact frequency,

at which each data point was recorded. Another shortcoming of the Nyquist diagram is the missing information about the double layer capacitance. The shape of the semi-circle does not change when only  $C_{DL}$  is altered in the equation. Therefore, for measurements of the double layer capacitance, the *Bode diagram* is a more suitable method to visualize the data. It plots both the logarithm of the absolute value of the impedance  $|Z|$  and the phase angle  $\varphi$  against the frequency on a logarithmic scale to the base of 10. This representation also has the advantage that the frequency is directly shown in the diagram. Fig. 2.8 shows a Bode representation of the same data sets used in Fig. 2.7.

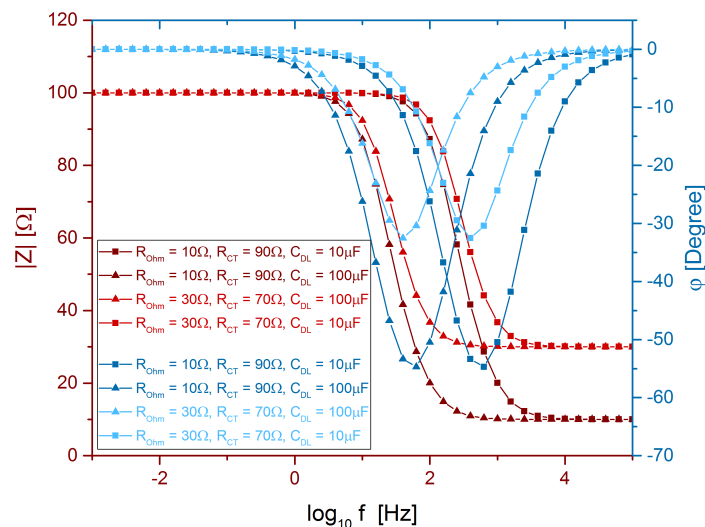


**Fig. 2.8:** Bode diagram of the same data sets as in Fig. 2.7. The red curves show the absolute impedance  $|Z|$ , the blue curves the phase angle  $\varphi$ . Curves of the exact same color only differ in  $C_{DL}$ .

Although in the Bode diagram  $C_{DL}$  still cannot be extracted from the curves directly, a difference between curves that only differ in  $C_{DL}$  is visible now, as can be seen when comparing two curves of the exact same color. The upper limit of the absolute impedance curves (red color) represents  $R_{CT} + R_{Ohm}$  and the lower limit equals  $R_{Ohm}$ .

## 2.3 Scanning Probe Microscopy

The underlying principle of all SPM is to create a map of the examined surface by raster scanning a sharp probe across the surface in parallel lines that ultimately form a two-dimensional grid. During this scanning process, the movement is interrupted regularly to measure a physical or electrochemical parameter. The measured data points are then converted into a two-dimensional map of the surface by the measurement software. Because many data points are needed for an accurate representation of the surface,

measuring an SPM image often takes several minutes. In this work, most images were recorded at a 512 x 512 pixel resolution and a scan rate of 2 Hz, deviations will always be stated in the description. This accumulates to over 4 minutes for a single image. The slow scanning process often causes the images to appear stretched. The expansion or contraction of tip, sample or scanner materials slowly shift the center of the imaged area, caused by temperature changes, material relaxation or external influences is known as drift.

### 2.3.1 Scanning Tunneling Microscopy

The technique of STM makes use of the quantum mechanical effect of electron tunneling. If two materials in vacuum are brought in close enough proximity, electrons can tunnel through the vacuum gap via overlapping wave functions of atoms on each side. Statistically, this process takes place continuously at equal rates in each direction. The situation changes when a bias voltage  $U_{bias}$  is applied between the two materials. Now one direction of electron tunneling becomes favored over the other and a net tunneling current  $I_T$  starts to flow which depends exponentially on the distance and linearly on  $U_{bias}$ . In STM, the tunneling current is measured between a sharp metal tip and the sample surface. The tip is moved across the surface in small steps by a three-axis piezo-scanner that is able to move the tip in x-, y- and z-direction. At each measuring position, the tunneling current is determined and the tip height adjusted by a feedback loop which reduces or increases the tunneling current until a setpoint value is reached. The z-distance travelled by the tip at each data point is then converted into the height information of the microscope image. Because this method is based on the measurements of currents, the operation of STM is limited to conductive samples. A detailed formalism of the tunneling effect can be found in many quantum mechanics textbooks such as [53].

Two major modes of operation exist for STM, generally known as the *constant current* and the *constant height* modes. In both modes, the tip is first slowly brought closer to the surface with  $U_{Bias}$  applied until it senses a pre-set tunneling current  $I_{sp}$ . Once the tunneling current is established, in constant height mode the tip is only moved in xy-direction (parallel to the surface). The current measured at each data point is converted into distance information and therefore the height of the sample at that position. This method can cause problems when it is used on uneven samples. There, the tip might collide with larger surface features that stand out farther than the initial tip-surface distance. This can result in damage to both sample and tip. For this reason, the slightly slower constant current mode is used in most experiments. The tip-surface distance is adjusted through a feedback loop at each measuring position until the original setpoint current is reached again. The sensitivity of the feedback adjustments can be set in the measurement software with two feedback gain parameters - the integral (i) and the proportional (p) gain. If the gain values are set too high, the tip will become too sensitive to height changes,



commonly used. The potentials of tip  $U_{tip}$  and sample/working electrode  $U_{sample}$  are controlled separately by a bipotentiostat.

Tunneling currents in STM experiments can range from below 50 pA up to several nA. Measuring these small currents in an electrochemical environment can be challenging because they cannot be experimentally distinguished from the Faradaic currents  $I_F$  at the tip that are caused by electrochemical reactions. Therefore, these unwanted currents must be reduced to a value significantly below the expected tunneling current. Since  $I_F$  is proportional to the surface area at which the reaction takes place, a simple method to reduce the  $I_F$  is to reduce the area of the tip that is in contact with the electrolyte.  $I_T$  decreases exponentially with the distance between sample and tip. Thus, only its apex contributes significantly to the tunneling current. By coating the tip in an insulating layer that only leaves its apex exposed,  $I_F$  can be greatly reduced without any impact on  $I_T$ .

### 2.3.3 Scanning Electrochemical Potential Microscopy

SECPM is a variation of EC-STM and generally uses the same experimental setup. Instead of a tunneling current, SECPM measures the potential difference between tip and sample within the EDL. SECPM was first introduced in 2004 by Veeco Instruments, based on the concept of EC-STM [54]. In the same year, Woo et al. used a similar setup for direct measurements of the potential distribution in the EDL in z-direction on an Au(111) surface in a  $\text{NaBF}_4$  solution [55]. Hurth et al. used the same technique in 2007 to investigate the influence of changes in surface potential and electrolyte concentration on the EDL structure at different surfaces [56]. To increase the accuracy of those approach curves, Yoon et al. developed a technique that modulates the tip-sample distance during the measurement to filter out time-dependent noise [57]. Their method yields more detailed information about the potential distribution in the EDL than conventional approach curves. The first two-dimensional SECPM images were published by Corbella et al. in 2005 in an analysis of the deposition of tungsten on a diamond-like carbon surface [58]. In 2009, Baier et al. showed in a comparison of SECPM and EC-STM images of enzymes on HOPG that SECPM can have superior resolution and showed first experimental proof that even non-conductive adsorbates can be detected which remain hidden in EC-STM measurements [59]. Furthermore, various metal single crystal surfaces were analyzed by Wolfschmidt et al. in a comparison of AFM, EC-STM and SECPM [60] and by Traunsteiner et al. in a study of the oxidation of Cu(111) surfaces in an alkaline solution [61].

The measured potentials at the tip are determined by complicated interactions between the electrochemical double layers of SECPM tip and sample and are also subject to other influences. Hamou et al. used finite element method simulations to analyze the influence of tip shape, Debye screening effects and overlapping EDLs on the SECPM measurements [40-43]. They discovered that the tip geometry and the dielectric permittivity of the tip's

coating layer influence the tip potential and also discovered that the observed size of adsorbed particles in SECPM depends on the concentration of the electrolyte [65]. Dickinson showed in numerical simulations that for sharp tips with radii smaller than 50 nm, the basic model describing the electrochemical double layer by Gouy, Chapman and Stern (GCS model, introduced in section 2.1.2) no longer accurately describes the diffuse layer of the EDL [66].

For the measurements, the potential of the sample is controlled while the tip is at open circuit potential and therefore changes with the potential in the surrounding electrolyte. At a large distance from the surface, the tip has the same potential as the bulk electrolyte. When it is brought closer to the electrode surface, it enters the sample's EDL and its potential gradually shifts towards that of the working electrode, following the EDL's potential distribution. The measured potentials therefore depend on the distance between tip and sample and can be used as a feedback signal, just like the tunneling current in STM but in contrast to this method, the independence from currents gives SECPM a major advantage over STM. Even non-conductive samples or adsorbates can be examined, as long as an EDL is formed at their interface with the electrolyte. However, what makes SECPM truly remarkable and unique is the ability to locally probe the structure of the EDL which is still one of the least understood areas in the field. Measuring the potential during the approach towards the sample directly yields the potential distribution within the EDL. Potential maps of the surface can show how adsorbed molecules disturb the EDL structure and even changes in their oxidation state could be detected.

#### **2.3.4 Atomic Force Microscopy**

Atomic force microscopy is one of the most commonly used SPM methods because of its versatility. Several different modes of operation and many possible variations of tip properties allow measurements on almost any type of surface and topographic measurements can even be combined with the investigation of other properties of the sample such as conductivity, magnetic properties or rigidity. In all variations of AFM, a small tip attached to the bottom of a cantilever is scanned over the surface in the same manner as in STM. Different forces, such as van-der-Waals or direct contact, attract or repulse the tip, bending the cantilever in the process. This movement can be measured by reflecting a laser beam from the cantilever surface and using a laser detector to record changes in its position.

The most basic AFM technique is the so-called *contact mode* in which the tip is physically dragged across the surface. Therefore, the motion of the cantilever is a direct translation of the surface topography. However, this method only gives good results when a stable sample is used, any adsorbates or soft and unstable areas are easily damaged. Therefore,

the less intruding *tapping mode* (TM) is often used. Here, the cantilever is oscillated near its resonance frequency during the measurement. The forces between tip and sample influence the oscillations. By monitoring the changes in the oscillation frequency, the surface structure can be deduced. Another mode of contactless AFM is the so-called *ScanAsyst* technique. In this case, a force vs. distance curve is recorded at each measurement point. From these curves, the software can precisely determine the tip-sample distance. ScanAsyst mode has the additional advantage that most microscope parameters such as feedback gains and oscillation frequency do not need to be optimized manually because it already delivers the best possible image. It is also possible to operate AFM in liquids and perform in-situ electrochemical measurements (EC-AFM) by transferring the setup into an electrochemical cell.



## 3 Materials and Experimental Setup

In this chapter, an overview of the experimental setup of all experiments and the necessary sample preparation methods will be provided. Also, the materials used in this work will be introduced. While the majority of the experiments were performed in the local laboratory at *TUM-CREATE*, some of the SECPM measurements discussed in chapter 4 were conducted by or in cooperation with affiliated groups at the *Technische Universität München* (TUM) and at the *Newcastle University* (NU), which will be marked in the captions of the presented data.

### 3.1 Microscope Setup

The microscope used in this work was a Bruker MultiMode 8 that is able to perform STM, EC-STM, SECPM and AFM measurements. For AFM, the microscope head must be exchanged. The following descriptions of the experimental setup are all based on this model. The microscopes used at *TUM* and *NU* were a Bruker MultiMode 6 and another Bruker MultiMode 8 respectively. The design of the electrochemical cells and microscope head is the identical for all three machines. Any differences between these microscopes in setup and performance do not significantly influence the outcome of the experiments.

#### 3.1.1 Experimental Setup for EC-STM and SECPM

The microscope is positioned inside a specially equipped glove-box by MBraun where it stands on an active vibration-cancelling device to shield the measurements from any external mechanical disturbances. Besides being modified to provide connections for all necessary cables, the glove-box also features a large metal plate that is built underneath the main chamber. It guarantees a firm stand on the floor to establish a more stable measurement environment that is less likely to pick up external vibrations. The glove-box itself is positioned on a slab of floor that is mechanically decoupled from the building through compressed air cushioning that are built directly onto the foundation of the building. The glove-box was only in operation when an inert atmosphere was needed for the experiment because the gas-flow inside the box can disturb the scanning process and distort the images. The MultiMode microscope consists of an arrangement of three major components (Fig. 3.1 (a)).

- The *microscope body* holds the circuits that control the scanning process. It is equipped with a switch that changes between three different microscopy modes (STM, Tapping-mode AFM and all other AFM modes) and a second switch that is

used to move the sample up and down, bringing it closer to the tip. It is used before a measurement until they are close enough to initiate the software controlled engagement procedure.

- The *scanner* is placed on top of the body. It holds the piezo-electronics that move the sample underneath the tip in sub-nanometer precision during the imaging process. A small step-motor is used for the final approach of sample and tip. The scanner used in this work is the E-model which is able to scan areas of up to 13.4  $\mu\text{m}$  edge length.
- The *microscope head*, either for STM/SECPM or for AFM, is placed on top of the scanner (Fig. 3.1 (b)). The STM head contains the current and potential amplifiers for STM and SECPM respectively, a holding tube for the microscope tip and the contacts and positioning screws for the RE and CE wires. The AFM head is equipped with a laser, the tip holder and the laser detector, as well as a window on its upper side. The window is used for illuminating the sample and to monitor the sample with an optical microscope that allows precise positioning of the tip on the surface and alignment of the laser on the cantilever.

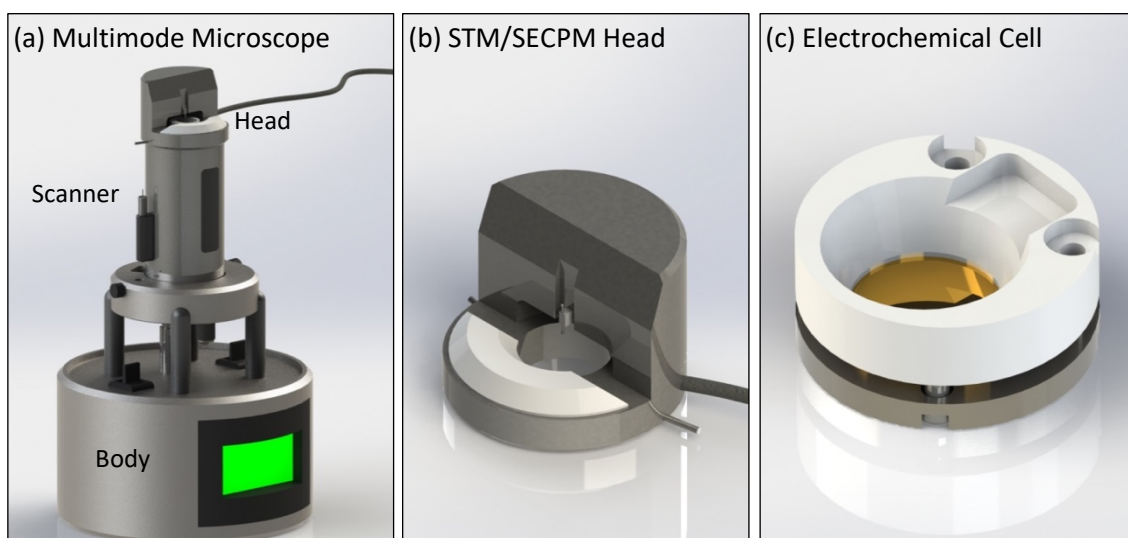


**Fig. 3.1:** Illustration of the microscope components. **(a)** The whole MultiMode 8 microscope with the body at the bottom, the scanner in the middle and the STM/SECPM head on top. **(b)** STM/SECPM head. The cell is positioned in the round hole in the center. **(c)** The electrochemical STM/SECPM cell with a gold sample positioned between Teflon cell (white) and baseplate (grey).

The electrochemical cell for EC-STM and SECPM is made of a Teflon ring with an inner diameter of 7 mm which slightly increases from bottom to top (Fig. 3.1(c)). To assemble the cell, the sample is positioned on a metal base plate that also serves as the electrical connection between scanner and sample. The Teflon cell is carefully placed on top of the sample to prevent gaps through which the electrolyte could leak out of the cell. The

assembly is then fixed in place with four screws that enter through the base plate. A cross section of the setup of the cell is shown in Fig. 3.2.

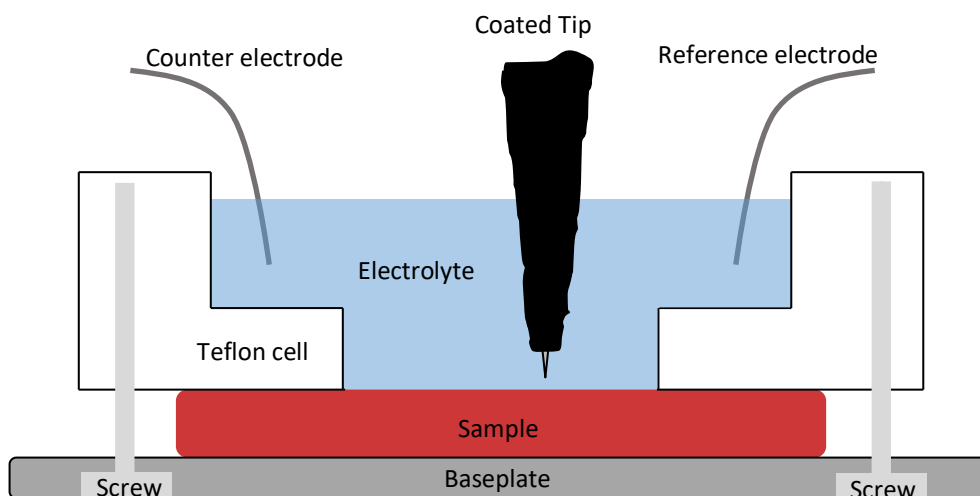


**Fig. 3.2:** Schematic cross-section of the electrochemical cell for EC-STM and SECPM. After the cell is fully assembled, the tip is brought close to the surface manually. Next, the electrolyte is filled in and finally CE and RE are put into position.

After placing the cell on the scanner where it is held in position magnetically, the STM/SECPM head is positioned on top of cell and scanner and secured by two metal springs. The scanner must be retracted beforehand to make sure that the tip does not contact the surface during the positioning. Even the smallest contact would destroy the tip and could even damage the sample. Next, the electrolyte is filled in with a pipette and the RE and CE wires are bent into the measurement position, in which they enter the electrolyte but do not contact the sample, the tip or each other. The tip can now be manually brought close to the surface using the switch on the microscope body. The final few  $\mu\text{m}$  of the tip approach and all measurement parameters are controlled using the Nanoscope control-software. For the experiments in the different laboratories, different metal wires were used as reference and counter electrodes:

Lab	CE	RE	Experiment
TUM-CREATE	Pt (0.5 mm)	Pt (0.5 mm)	All
TUM	Pt (0.25 mm)	Pt (0.25 mm)	Experiment in Fig. 4.2
TUM	Au (0.5 mm)	Au (0.5 mm, oxidized)	All other experiments
NU	Pt (0.5 mm)	Pt (0.5 mm)	All

The gold wire reference electrode used at TUM was oxidized in a 1 M  $\text{H}_2\text{SO}_4$  solution at a potential of 12 V for several seconds. The procedure was terminated once the wire was visibly fully coated with an oxide layer. The material of the counter electrode does not

influence the experiment, as long as the potentials are kept within its stable window. Since the wires are only quasi-reference electrodes, their potential is not stable when the pH value of the solution changes. However, in the SECPM studies of this work it is not necessary to know the exact reference potential for the interpretation of the results. Within each image series, the reference electrode remained the same and the images are comparable. Therefore, the potentials were not converted to a common reference, with the possibility of error due to not exactly known pH values, but rather stated against the reference electrode they were measured with. For comparison, the reference potentials in a 0.1 M H<sub>2</sub>SO<sub>4</sub> solution in contact with air are 0.92 V vs. NHE for the Pt wire and 1.25 V vs. NHE for the Au/Au-oxide wire.

Since the electrochemical cell, microscope tip and all electrodes can be used in both EC-STM and SECPM, it is possible to switch between both modes without the physical modifications to the microscope setup. A command in the control software switches between the current amplifier for EC-STM and a high input-impedance potential amplifier for SECPM. This enables the user to subsequently record images of the same surface area in both modes. A comparison of these images can increase the amount of information about the surface.

### 3.1.2 Tip Preparation

The STM/SECPM tips were prepared from a Pt/Ir wire with a ratio of 80/20 and 0.25 mm diameter. An advantage of using this material is that sharp tips do not have to be etched electrochemically but can be cut manually, which reduces the time needed to produce one tip from several minutes to only a few seconds. For the cutting procedure, the end of the wire is held strongly with flat-nose pliers. Then, a set of clean and sharp pliers is used to cut and simultaneously pull the wire apart at an acute angle at a typical length of between 1 cm and 1.5 cm. If the cutting pressure is too high, the wire will only be cut, not pulled, which yields a lower ratio of good quality tips.

For all electrochemical measurements, the tips must be coated with an insulating layer to reduce the influence of faradaic currents. At *NU*, a commercial clear nail polish was used for the tip coating. It is carefully applied by brushing it onto the wire towards the tip-end using the brush supplied with the nail polish. This is a cheap and simple method for tip insulation. However, the tips cannot be used immediately after coating because the nail polish must first dry completely to prevent any solvents from contaminating the cell. This process can take up to 30 minutes. Therefore, in all other experiments the tips were coated in a layer of insulating Apiezon wax instead, which is inert under the conditions used in the experiments for this study. For the coating procedure, a flat-tip soldering iron with a 1 mm wide slit cut into its tip was installed horizontally in a holding mechanism. A stick of Apiezon wax is brought into contact with the soldering iron. Set to a temperature

of 170 °C to create the right viscosity, a small portion of the wax melts and sticks to the iron, covering the slit. Now, the sharp microscope tip can slowly be inserted into the slit from the side with its top is always visible above the wax. Once fully surrounded by the wax, it is pulled down until the apex is covered and then pushed upwards again until the desired length of the tip wire is coated (between 2 mm and 4 mm). Finally, the tip is pulled out sideways through the slit. An illustration of the coating procedure is shown in Fig. 3.3. This coating procedure can normally be performed in less than 30 seconds.

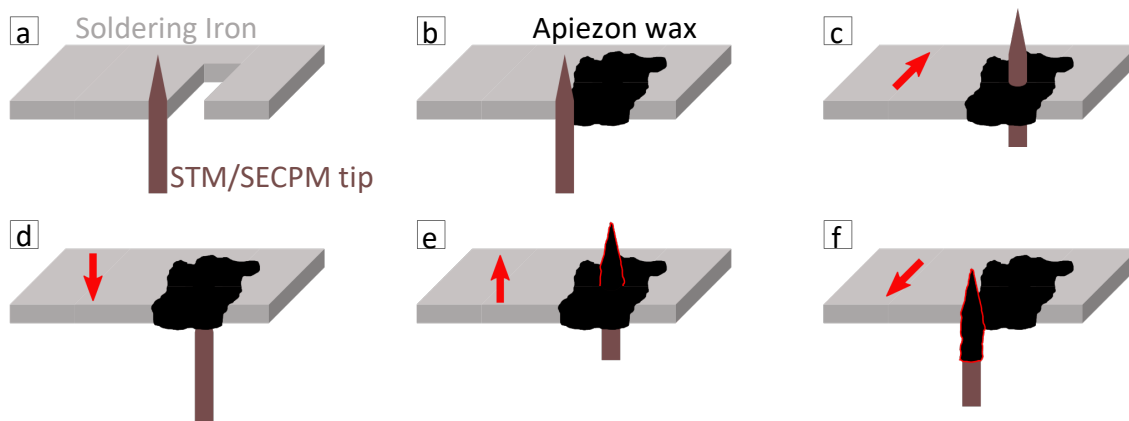


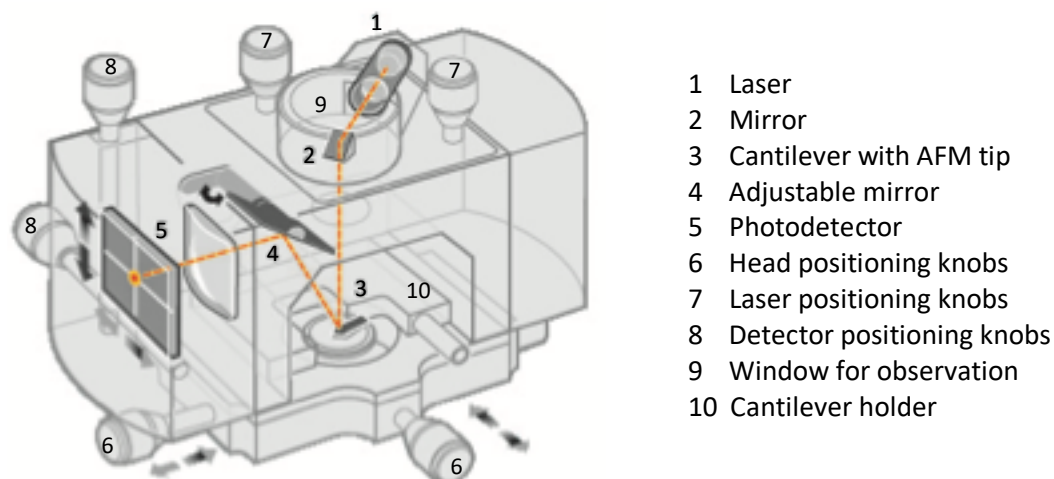
**Fig. 3.3:** Illustration of the tip coating procedure. After the soldering iron is heated to 170 °C, a small amount of Apiezon wax is melted over the slit. Once the wax has fully melted the tip is inserted from the side. The red arrows indicate the direction of tip-movement for each step. The whole procedure can be performed in less than 60 seconds.

Due to its viscosity, the wax flows away from the tip's apex when it is pushed upwards through the wax surface, exposing it in the process. Most tips fabricated with this process show leakage currents that are frequently below 50 pA and therefore well below the often used setpoint current of 1 nA. The wax hardens quickly enough that the tips can be used few minutes after they were coated.

### 3.1.3 Experimental Setup for AFM and EC-AFM

For the AFM techniques, a different head has to be mounted on the microscope after the sample is positioned on the scanner. This AFM head contains the laser and photodetector as well as the electronics to oscillate the tip for tapping mode measurements Fig. 3.4. The laser follows the orange path from its source<sup>1</sup> through a mirror<sup>2</sup>, reflecting from the cantilever<sup>3</sup> and a second, adjustable mirror<sup>4</sup> until it reaches the photodetector<sup>5</sup>. The round knobs extending out from the head are to adjust the position of the tip over the sample<sup>6</sup>, the position of the laser on the cantilever<sup>7</sup> and the position of the detector<sup>8</sup>. The laser positioning is necessary to align the beam with the front of the cantilever to obtain the strongest possible laser signal at the detector. A small window<sup>9</sup> is built into the top of the head to allow the user to monitor the tip and laser during alignment and approach

through an optical microscope that is connected to the computer. After the head has been connected to the microscope, the tip holder<sup>10</sup> with the installed cantilever is mounted inside the head.



- 1 Laser
- 2 Mirror
- 3 Cantilever with AFM tip
- 4 Adjustable mirror
- 5 Photodetector
- 6 Head positioning knobs
- 7 Laser positioning knobs
- 8 Detector positioning knobs
- 9 Window for observation
- 10 Cantilever holder

**Fig. 3.4:** Sketch of the AFM head. The orange line shows the path of the laser beam from its source to the photodetector. Image adapted from [67].

Due to its shape and because an unobstructed path for the laser beam must be guaranteed at all times, the design of the electrochemical cell for EC-AFM is more complicated than the EC-STM/SECPM cell. An illustration is shown in Fig. 3.5. The shape of an air-electrolyte interface would be subject to fluctuations caused by air flow and tip movement which would disturb the laser beam. Therefore, the electrolyte is encased in a chamber that is closed to all sides. The cell itself is made of glass<sup>5</sup> to let the laser beam pass through undisturbed. An O-ring<sup>1</sup>, positioned in a ring-shaped groove on the bottom side of the cell, is used to seal the cell-chamber in order to keep the electrolyte inside. Three channels connect the chamber to the front of the cell, two of which are used to fill it with the electrolyte and as overflow for excess electrolyte<sup>10</sup>. The third channel gives access to the reference electrode<sup>2</sup>, made of the same 0.5 mm Pt-wire as for the EC-STM and SECPM experiments. The counter electrode<sup>3</sup> is positioned inside the chamber through a small hole from the top surface of the cell and is held in place by tying it around a holding pole on top of the cell<sup>4</sup>. The cantilever<sup>9</sup> itself is positioned in a small indentation in the center of the cell, secured in position by a metal hook<sup>9</sup> that also functions as a connection to the microscope electronics. After tip, O-ring and electrode wires are firmly attached to the cell, it is positioned inside the AFM head, fixed by a clamping mechanism that also completes the connection from the tip to the microscope. The sample<sup>7</sup>, attached to the base plate<sup>6</sup>, is then positioned on the microscope scanner before the head is mounted on top of it and secured by the same metal springs that are used to hold the STM/SECPM head.

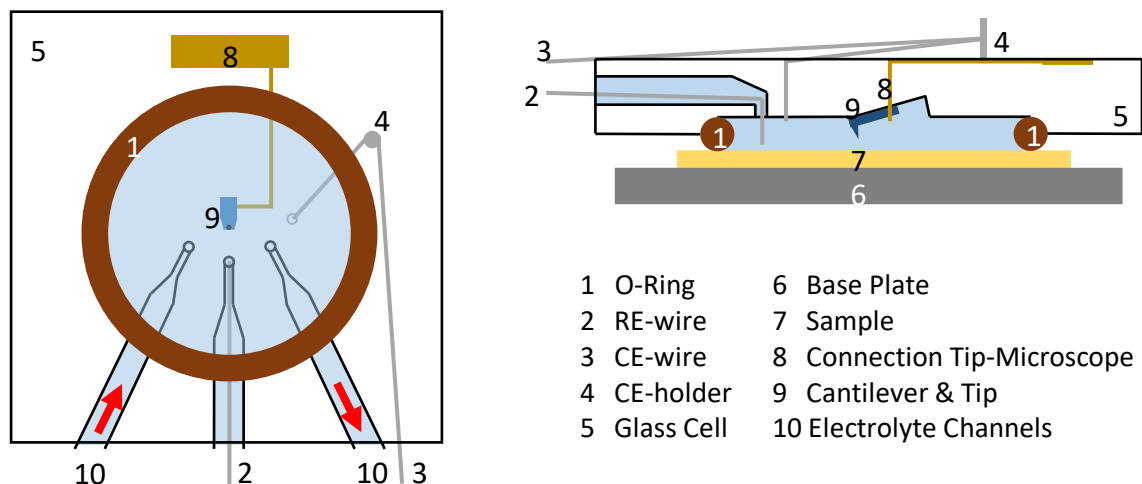


**Fig. 3.5:** Illustration of the electrochemical glass cell for EC-AFM. Shown from below on the left and as a cross-section on the right.

Now, the electrolyte can be carefully filled in through the channels, using a syringe. Any air bubbles inside the cell must be removed by inserting more electrolyte because they would obstruct the laser's path. After setting up the cell and head, the laser has to be aligned on the cantilever and the detector and the cantilever tuned to the operation-frequency. In a liquid environment, the laser alignment tends to drift and must be re-aligned regularly during the measurements.

### 3.2 Electrochemical Impedance Spectroscopy

The EIS measurements as well as the CVs for the double layer capacitance study were performed in a highly symmetric Kel-F cell (Fig. 3.6). After filling the cell with the ionic liquid, it was immediately closed with the gold single crystal to prevent it from absorbing more water from the ambient air. To keep the liquid inside the cell, the sample is pressed onto the opening using a cell holder which consists of two plates held together by four screws. A folded piece of aluminum foil is positioned between the sample and the cell holder to establish the electrical contact between sample and potentiostat. The counter electrode, a 0.5 mm gold wire, was positioned at the opposite side of the cell. A 0.5 mm platinum wire quasi-reference electrode was used to keep the input impedance low. The gold surface was exposed to the ionic liquid through a circular opening in the cell with a 3 mm radius. After the cell was set up, the aluminum foil and the reference electrode and counter electrode wires were connected to an SP-300 Bio-Logic potentiostat for the electrochemical measurements. After each experiment, the cell and electrode wires were thoroughly rinsed with acetone and left to dry completely before the next use.

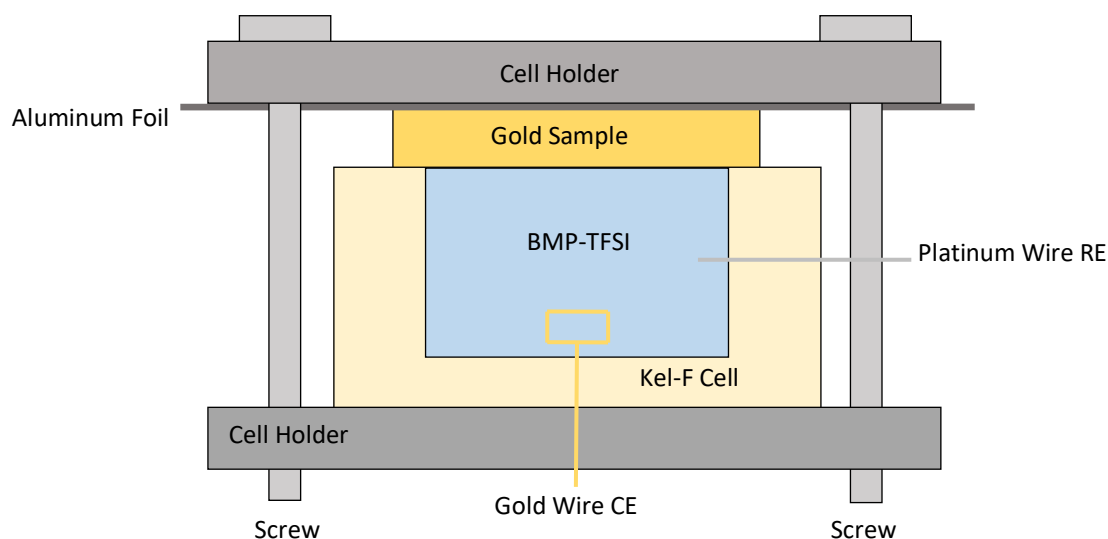


**Fig. 3.6:** Cross-section of the electrochemical cell used in the EIS measurements. The RE and CE were inserted into the IL through small holes in the Kel-F cell and then sealed with Teflon tape.

### 3.3 Materials

#### 3.3.1 Ionic Liquids

Ionic liquids can provide an interesting alternative to organic solvents in battery electrolytes. This is mainly due to their large stable potential window which would allow higher battery voltages. Their low flammability could also lead to much safer batteries, an important property for applications in electromobility. ILs are a group of mostly organic salts with low melting points around room temperature or in some cases up to 150 °C [68]–[70]. In contrast to dilute conventional electrolytes, where ions are surrounded by large amounts of solvent and thus mainly interact with each other through long range Coulomb forces, direct ion-ion interactions become an important factor in ILs. To obtain the properties necessary for a low melting point, the combination of cations and anions is chosen specifically to inhibit crystallization. In most cases, large organic cations are combined with smaller organic or inorganic anions that often have an asymmetric shape. Delocalized charges in the anions reduce the ion-ion Coulomb forces [71]. All these characteristics make the formation of a stable crystal lattice more difficult.

A first ionic liquid with intrinsic conductivity – ethylammonium nitrate  $[\text{EtNH}_3][\text{NO}_3]$  - was already described in 1914 by Paul Walden [72], and in the following decades, several new ILs were discovered [73]. However, it took until the 1970s until they became subject of more extensive research, in this case on a class of chloroaluminate ionic liquids [74], [75]. The applicability of this class of ILs was limited due to their complicated and expensive synthesis and purification processes, as well as their high moisture sensitivity [74]. These

problems were only solved when a new generation of ILs was described in the 1990s, mostly based on ammonium salts or cyclic amines [69]. Since then, they have become a rapidly growing research field due to their versatility and easy adjustment of their properties. Their unique structure gives ILs a number of properties that, in their combination, cannot be found in any other material [23], [24], [26], [76]–[78]:

- Due to the strong electrostatic forces between cations and anions in direct contact with each other, the volatility of ILs is so low that it can be ignored in most situations.
- In general, ILs have a high thermal and electrochemical stability because they consist of rather inert ions. This gives them a large operable potential window that can reach up to 5 - 6 V and a high liquid temperature range of up to 200 °C.
- Already, a large and still increasing number of easily modifiable ions is known and different ILs can be mixed with each other and with many polar solvents. Therefore, the properties of ILs can be tuned as desired in an almost infinite number of possible combinations.
- Many ILs function as a nearly universal solvent.
- Because of the absence of organic solvents, ILs exhibit a very low flammability.
- Even though ILs basically consist completely of charge carriers, their conductivity is rather low. While conventional water-based electrolytes have conductivities between 200 and 800 mS cm<sup>-1</sup>, the conductivity of ILs at room temperature is mostly in a much lower range between 0.1 and 18 mS cm<sup>-1</sup>. This rather unintuitive property is caused by their comparatively high viscosity and therefore low ion mobility.

In this work, the IL *1-Butyl-1-Methylpyrrolidinium Bis(Trifluoromethylsulfonyl)imide* (BMP-TFSI) was used for the double layer capacitance measurements in chapter 5 and in the SECPM experiment comparing the imaging capabilities in different electrolytes in chapter 4.1.1. The molecular structures of the *Pyrrolidinium* cation and the TFSI anion are illustrated in Fig. 3.7. The high purity BMP-TFSI used for the impedance spectroscopy experiments was bought dried to a water content of 60 ppm. It was continuously stored in a sealed container inside a glove box under Argon atmosphere with a water content constantly below 1 ppm. For transport to the measurement, small amounts were transferred into a glass container and only exposed to ambient air directly before being used. For measurements with increased H<sub>2</sub>O content, drops of MilliQ water were added to the IL with a pipette. The resulting amount of water in the IL was determined by Karl-

Fischer titration, using a Metrohm 831 KF Coulometer. It returns the water content in ppm, comparing the detected amount of water to the total weight of the inserted liquid. For a more meaningful expression of the water content, the results were converted into the ratio of BMP or TFSI ions to water molecules. It is then expressed as values in the form of 1000 : 100. In this example, the ionic liquid contains an average of 100 H<sub>2</sub>O molecules per 1000 BMP or TFSI ions.

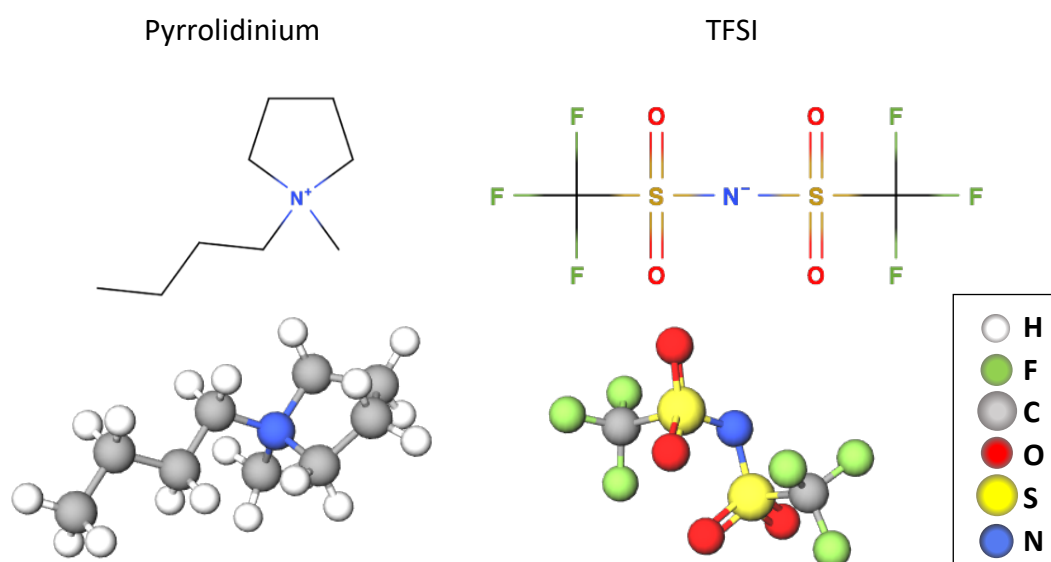


**Fig. 3.7:** Illustration of the molecular structures of the BMP-TFSI ionic liquid. On the left the 1-Butyl-1-Methylpyrrolidinium cation and on the right the Bis(Trifluoromethylsulfonyl)imide anion.

### 3.3.2 Polyoxometalates

POMs are most commonly based on early transition metals like vanadium, molybdenum or tungsten [79] and often combined with a central heteroatom such as phosphorus, silicon, aluminum, arsenic or germanium [80]. POMs can reach astonishingly large sizes with molecules containing several hundred metal atoms, resulting in diameters up to 6 nm [81], [82]. Consequently, they can be viewed as an intermediate construct between oxoanions of non-metals in aqueous solution and insoluble metal-oxides and possesses some unique properties [79]. The heteroatoms are predominantly surrounded by discrete MO<sub>6</sub> octahedra, where M is the respective metal atom, with short M=O (dπ-pπ) *terminal* bonds that are directed outwards. Due to low surface charge densities and therefore weak anion-cation attraction compared to the cation solvation energies, POMs have a wide-ranging solution chemistry in aqueous as well as non-aqueous solvents [79]. Interesting for the use in energy storage is their ability to undergo multiple redox reactions and therefore transport many electrons.

The first POM, the phosphomolybdate  $[\text{PMo}_{12}\text{O}_{40}]^{3-}$ , was already synthesized nearly 200 years ago by J. Berzelius [83]. However, more intensive research on them was only started around the beginning of the 20<sup>th</sup> century [84]. Important work on their molecular structure was done by J. Keggin in 1933. He analyzed the phosphotungstic acid  $\text{H}_3[\text{PO}_4\text{W}_{12}\text{O}_{18}(\text{OH})_{36}]n\text{H}_2\text{O}$  using X-ray diffraction. He found that the central  $\text{PO}_4$  group is surrounded by a shell of twelve  $\text{WO}_6$  octahedra which are linked by shared oxygen atoms. These octahedra are also arranged in four trimetallic  $\text{W}_3\text{O}_{13}$  groups that consist of three  $\text{WO}_6$  clusters with trigonal symmetry. Therefore, the complex anion can be expressed as  $[\text{PW}_{12}\text{O}_{40}]^{3-}$  [85]. The general POM type of  $[\text{XM}_{12}\text{O}_{40}]^{n-}$  is now commonly known as the *Keggin structure* with a typical ion size of around 1 nm, which is illustrated in Fig. 3.8.

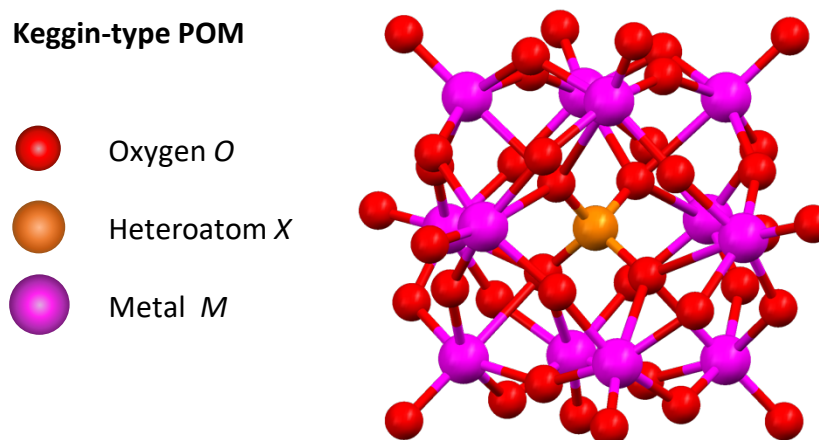


**Fig. 3.8:** Illustration of the molecular structure of the Keggin-type polyoxometalate with an orange heteroatom in the center, surrounded by the octahedral metal (pink) and oxygen (red) clusters. The image was adapted from [86].

The three axes of symmetry results in the existence of several rotational isomers of the Keggin ion. Out of the five possible structures, only three have to this point been realized experimentally. The most stable form, which is also the one originally analyzed by Keggin, is the  $\alpha$  isomer [87]. By rotation of one of the  $\text{M}_3\text{O}_{13}$  groups by  $\pi/3$ , the  $\beta$  isomer is formed. Further rotation each of the other trimetallic groups leads to the remaining isomers. Single or multiple metal centers of Keggin POMs can be removed experimentally in alkaline solutions under certain conditions [88]. Some of these lacunary Keggin species are still stable and especially the  $\text{XM}_9$  and  $\text{XM}_{11}$  types are commonly realized. Reacting with transition metals or similar elements, these vacant sites can be filled to form substituted Keggin POMs [80], [88]. Several other types of POM exist besides the Keggin structure. However, since only Keggin type POMs were used in this work, the other variations will not be discussed here.

The large variety in usable elements, composition, shape and size of POMs results in a wide range of tunable properties and possible applications [89]. Soluble in aqueous

media, many POMs act as strong acids and can be used in homogeneous and heterogeneous catalysis [79], [87]. As a consequence of the atomic structure, a single POM molecule can undergo many redox reactions [6], [7] which makes them a promising candidate as charge carriers for energy storage applications. Because of their relatively large molecule size, POMs are also expected to have a high electron transfer constant  $k_0$  [90].

### 3.3.3 HOPG

Highly oriented pyrolytic graphite is a pure form of graphite that exhibits a much smaller density of defects and material impurities than any other form of graphite. It possesses an oriented crystal structure of monoatomic graphene layers that are greatly larger than in common graphite. Atomically flat terraces with sizes over 1  $\mu\text{m}$  can be found frequently on *Highly Oriented Pyrolytic Graphite* (HOPG) surfaces. It is produced by high temperature decomposition of hydrocarbon gas (acetylene is commonly used) or chemical vapor deposition at temperatures around 2100  $^\circ\text{C}$ , followed by a high pressure annealing step above 3000  $^\circ\text{C}$  [91], [92]. The inter-layer distance in an HOPG crystal is 0.335 nm and the in-plane distance between two carbon atoms is 0.141 nm. Taking a closer look at a graphene monolayer *A* within the HOPG, it exhibits a honeycomb structure where every atom has three nearest neighbors. The layer *B*, positioned underneath *A*, is shifted in a way that an atom of *B* is always positioned below the center of each hexagon in layer *A*, as illustrated in Fig. 3.9 (b). The overall HOPG structure is a series of *ABABAB...* layers. Each layer consists of two equivalent interpenetrating triangular sublattices [93] that differ slightly in their atomic density of states [94]. In most STM images, only one of those sublattices can be resolved, the other appears as dark areas. Each sublattice exhibits an apparent spacing between atoms of 0.246 nm in the STM images.

HOPG is a widely-used sample in SPM experiments due to its unique properties. The large flat terraces are a highly useful background for deposition experiments, giving high contrasts between the graphite surface and any adsorbed materials. The surface is also mechanically stable and conductive enough for STM. The samples are comparatively inexpensive and can be re-used many times by simply removing damaged or contaminated surface layers which reveals a clean new surface. Finally, it is chemically inert under many circumstances which makes it a useful substrate for electrochemical measurements. The samples used in this work were of ZYB quality with a surface mosaic spread of  $1.2^\circ \pm 0.2^\circ$  and a grain size of up to 1  $\mu\text{m}$ . A fresh HOPG surface was prepared before each measurement with the cleaving method, where adhesive tape is pressed on the HOPG and then slowly pulled off. The topmost layers stick to the tape because of the weak inter-layer binding forces and are therefore removed from the sample. The new surface revealed this way is automatically clean and can be used immediately. An AFM

image of a typical, freshly cleaved HOPG surface is shown in Fig. 3.9 (a), including an illustration of the lattice structure (b) and an atomic resolution image (c).

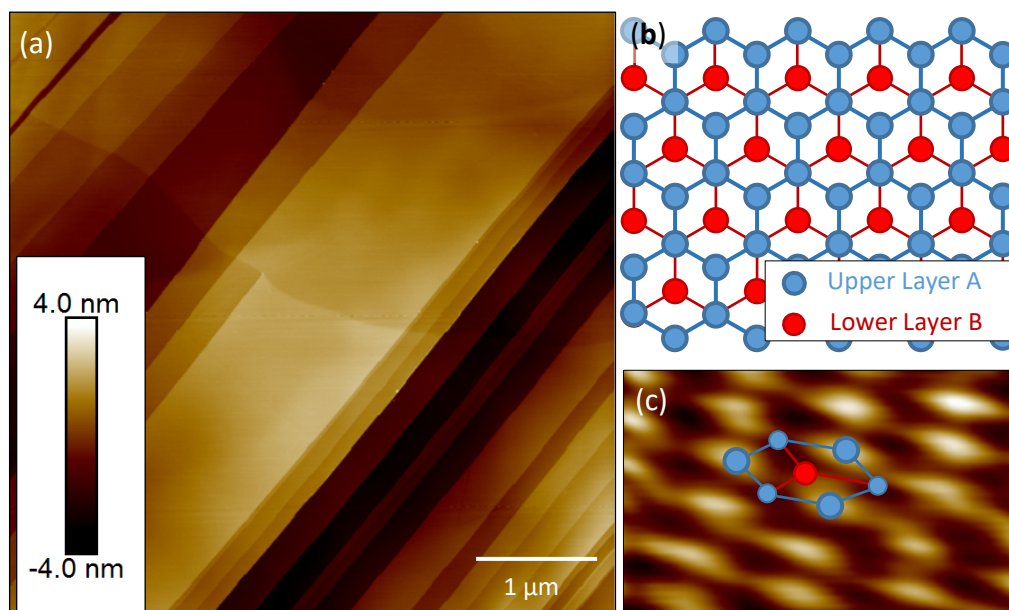


**Fig. 3.9:** (a) AFM image ( $5\ \mu\text{m} \times 5\ \mu\text{m}$ ) of a freshly cleaved HOPG surface with large terraces. (b) Structural model of two atomic HOPG layers. The blue layer A is located on top of the red layer B. (c) Atomic resolution STM image of HOPG.

In the large-area microscope image in in Fig. 3.9 (a), the typical combination of HOPG step edges and atomically flat terraces, also known as basal plane, can be observed. The structural drawing in Fig. 3.9 (b) shows the positions of the atoms in the two topmost graphene layers. An atom in the bottom (red) layer always occupies the position underneath the center of each hexagon of the top layer (blue). In Fig. 3.9 (c), an STM image of a HOPG surface with atomic resolution is shown. The drawn structural pattern marks the positions of the atoms in the two topmost layers for comparison with Fig. 3.9 (b). The different sizes of the blue circles represent the two sublattices of the graphene layer. Only the atoms of one sublattice are seen in the microscope image. The whole surface appears stretched due to a drifting effect that can be caused by a not perfectly horizontal sample surface or material expansion/contraction from mechanical relaxation or temperature shifts.

### 3.3.4 Au(111) Single Crystal

The Au(111) single crystal surface can be prepared to contain large flat terraces suitable for SPM experiments and is often used in electrochemical experiments because of its large stable potential window. Gold crystallizes in a *face centered cubic* (fcc) lattice structure of individual hexagonally close packed layers, following an *ABC* stacking sequence [95], [96]. The (111)-surface plane used in this work has a hexagonal atomic structure. A typical

surface consists of atomically flat terraces that can reach sizes up to several 100 nm. The steps separating the terraces are mostly monoatomic and 0.24 nm high [97]. They exist in two different orientational varieties, the (111) or the (100) type, depending on their alignment with the underlying crystal structure. The (111) type step is structurally more stable than the (100) type [98].

The Au(111) surface layer undergoes a surface reconstruction that is caused by the low coordination number of the surface atoms compared to the bulk crystal atoms. The structure of the surface layer is compressed by 4.34 %, fitting 23 surface atoms into 22 lattice sites [99]. A typical effect of this reconstruction is the so-called *Herringbone* structure, which appears as pairs of parallel lines and can sometimes be resolved in STM images. The distance between the two lines of each pair is 4.4 nm and the pairs have a distance of 6.3 nm from each other, the elevated structures appear ca. 0.02 nm higher than the surrounding atoms. If the terraces on the surface are large enough, the lines follow a zigzag pattern [100]. However, when immersed into electrolyte, the surface does not always form the Herringbone reconstruction, its structure depends on the applied potential. It was found that once the potential is increased over a certain value, the reconstruction is lifted. For example, observations of a Au(111) surface in a H<sub>2</sub>SO<sub>4</sub> solution showed that the Herringbone pattern is visible at potentials below 0.5 V vs. NHE. However, it is lifted when the potential is increased over 0.5 V, where an adlayer of hydrogen sulfate anions forms instead. At 1.0 V, the anion adlayer undergoes a phase transition into a disordered phase. Each transition caused a sharp peak in the cyclic voltammogram of the system [101], [102].

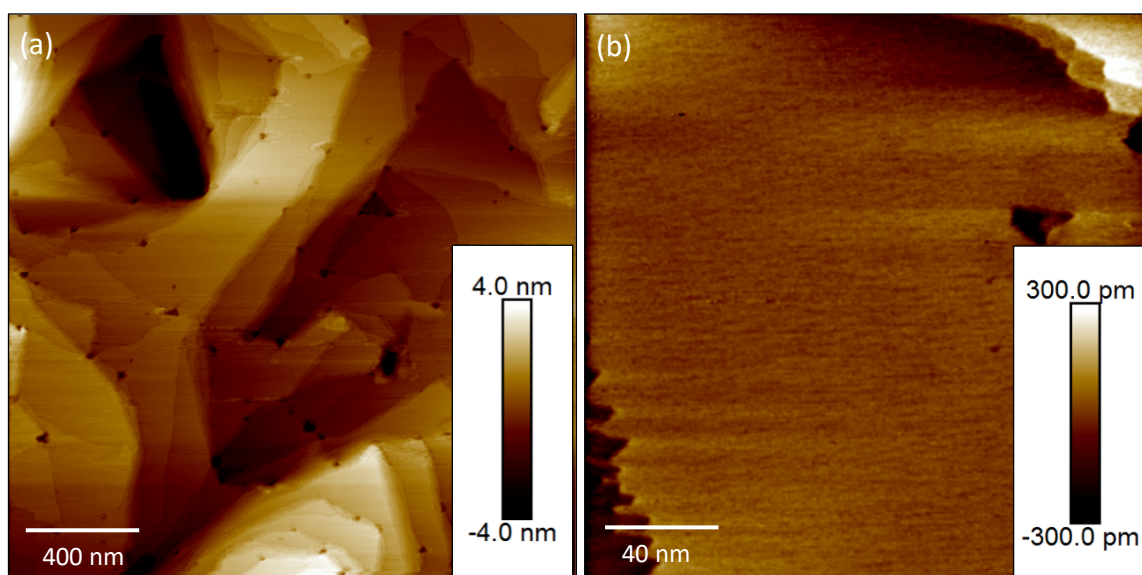


**Fig. 3.10:** Scanning Tunneling Microscope images of the atomically flat terraces of the Au(111) surface after annealing. **(a)** 2  $\mu\text{m}$   $\times$  2  $\mu\text{m}$  image, tunneling current  $I_T = 1$  nA, tunneling voltage  $U_{\text{Bias}} = 100$  mV. **(b)** 200 nm  $\times$  200 nm image,  $I_T = 1$  nA,  $U_{\text{Bias}} = 100$  mV. (This image has been adapted from our publication [103].)

The surface of the Au(111) single crystal was freshly prepared before each experiment. After finishing the measurement, it was immediately rinsed, first with Acetone and followed by de-ionized water. The cleaned crystal was stored and freshly annealed shortly before the next measurement. The annealing process creates larger Au(111) terraces. Using a butane torch-burner, the gold was heated in a darkened room until it exhibited a dark-orange glow and kept at that temperature for 10-20 seconds. Next, it was allowed to cool down for 30 seconds under a stream of Argon gas. This procedure was then repeated two more times before completely cooling the crystal down to room temperature under the Argon stream, which usually took 10 - 15 minutes. The atomically flat terraces achieved with this preparation method reached sizes up to several 100 nm (Fig. 3.10).

### 3.3.5 List of Materials

The following list includes all chemicals and other materials used for this work. Because in some cases different vendors or material purities were used in the different laboratories, separate lists are shown for each university.

#### TUM CREATE

Material	Vendor	Purity/Quality
Sulfuric Acid ( $H_2SO_4$ )	Sigma Aldrich	$\geq 99.99\%$
Lithium Sulfate ( $Li_2SO_4$ )	Sigma Aldrich	$\geq 99.99\%$
Hydrochloric Acid ( $HCl$ )	Sigma Aldrich	$\geq 99.99\%$
Lithium Perchlorate ( $LiClO_4$ )	Sigma Aldrich	99.99%
Phosphoric Acid ( $H_3PO_4$ )	Sigma Aldrich	99.99%
MilliQ water ( $H_2O$ )	Elga	R > 18.2 M $\Omega$ , TOC < 10 ppb
Ferrocene ( $Fe(C_5H_5)_2$ )	Sigma Aldrich	98%
BMP-TFSI ( $C_{11}H_{20}F_6N_2O_4S_2$ )	IoLiTec	99%
Gold wire	Goodfellow	99.99%
Platinum/Iridium wire	Goodfellow	Ratio Pt/Ir = 80/20
Platinum wire	Goodfellow	99.9%
Au(111) single crystal	MaTeck	99.999%
HOPG	Bruker	ZYB
Argon	National Oxygen	99.99%
Acetone ( $C_3H_6O$ )	Sigma Aldrich	p.a.
Apiezon Wax	Bruker	

## TUM

<b>Material</b>	<b>Vendor</b>	<b>Purity/Quality</b>
Sulfuric Acid ( $H_2SO_4$ )	Merck	supra pure
MilliQ water ( $H_2O$ )	Millipore	R > 18.2 M $\Omega$ , TOC = 3 ppb
Ethylene glycol	Sigma Aldrich	99.8%, anhydrous
BMP-TFSI	IoLiTec	99.5%
Gold wire	MaTeck	99.995%
Platinum wire	MaTeck	99.99%
Platinum/Iridium wire	MaTeck	Ratio Pt/Ir = 80/20
HOPG	MicroMasch	ZYB
Apiezon Wax	Plano	

## NU

<b>Material</b>	<b>Vendor</b>	<b>Purity/Quality</b>
Sulfuric Acid ( $H_2SO_4$ )	Sigma Aldrich	$\geq 99.99\%$
MilliQ water ( $H_2O$ )	Elga	R > 18.2 M $\Omega$ , TOC < 10 ppb
Platinum/Iridium wire	Goodfellow	Ratio Pt/Ir = 80/20
Platinum wire	Goodfellow	99.9%
HOPG	Bruker	ZYB

All POMs used in this study were synthesized and supplied by the group of Prof. Ulrich Kortz at the Jacob's University Bremen in Germany.

## 4 Image Generation in SECPM

The possibility of directly mapping the potential distribution within the EDL, either in z-direction with approach curves or in x-y-direction with two-dimensional microscope images, should be interesting enough to be used in many studies. Therefore, it is quite surprising that since SECPM was developed, it has only been used in a very small number of publications. One reason might be that it is more difficult to obtain images of sufficient quality than in EC-STM and EC-AFM measurements because on the one hand, tips that produce sharp images in EC-STM often do not even engage in SECPM. On the other hand, the image quality greatly depends on the working electrode potential. The level of noise in the images increases rapidly when the potential approaches the PZC, up to a point where the surface is not recognizable anymore. Therefore, in a certain potential range around the PZC, SECPM cannot be performed at all. The size of this window depends on the quality of tip and tip-coating and can often extend over several 100 mV, preventing the use of SECPM if the potential of interest lies within that region. From many SECPM measurements, the center of the potential range can be estimated between 0 mV and 100 mV vs. Pt for HOPG in a 0.1 M H<sub>2</sub>SO<sub>4</sub> solution. Another possible reason for the small number of publications utilizing SECPM can be found in the complicated interactions between the double layers of tip and sample which overlap at during the measurements, preventing an easy deconvolution of the contributions of sample and tip to the measured images. Furthermore, a full description of the double layer structure of the sharp, irregularly shaped tips and the influence of the tip coating requires more complex models than the ones that are currently available. Several attempts have been made to gain a deeper insight into the topic. Hamou et al. analyzed the influence of the tip shape and the consequences of overlapping double layers with finite element method simulations to explain the behavior of previously measured potential-distance curves [62]–[65]. Traunsteiner et al. investigated the influence of leakage currents from electrochemical processes and electron tunneling on the measured tip potential and came to the conclusion that mainly a tunneling current, similar to the one measured in STM, determines the tip potential [61].

Despite these efforts, not much is known about the influence of thickness and composition of the EDL on the measured SECPM images. Therefore, the effects of changing electrolyte concentration and of different types of liquids on the SECPM images will be analyzed, including the first atomic resolution images reported with this technique. In the second part of this chapter, the nature of an artifact that is often found in SECPM images of HOPG step edges in the form of an oscillation will be investigated. To understand its origin, changes in the oscillation pattern were monitored during the variation of different measurement parameters. For an easier distinction between SECPM

images and the images from other SPM methods, a different color scheme was selected for SECPM (blue/white instead of the traditional brown/yellow). This study was conducted in cooperation with our colleagues at TUM (Lukas Seidl, Yunchang Liang and Oliver Schneider) and NU (Jingying Gu). Measurements contributed by their laboratories are marked in the image captions.

## 4.1 Influence of Parameter Variations

SECPM relies on the potential gradient within the electrochemical double layer to guide its feedback mechanism. Therefore, it is important for the interpretation of all results of to understand how the resulting images are affected by the double layer structure itself.

### 4.1.1 Electrolyte Composition

The GCS model describes the reason for the formation of an EDL with the influence of the electric field of a polarized electrode on the ions within the electrolyte [14]. A positively charged electrode increases the concentration of anions near the interface while reducing the cation concentration in the same region, and vice versa for a negatively charged electrode. However, the resulting ion distribution and thus the potential profile also depends on the concentration of ions in the bulk electrolyte. To analyze how this affects the SECPM images, an image series in varying concentrations of sulfuric acid (Fig. 4.1) was recorded, with all other parameters and settings held at constant values.

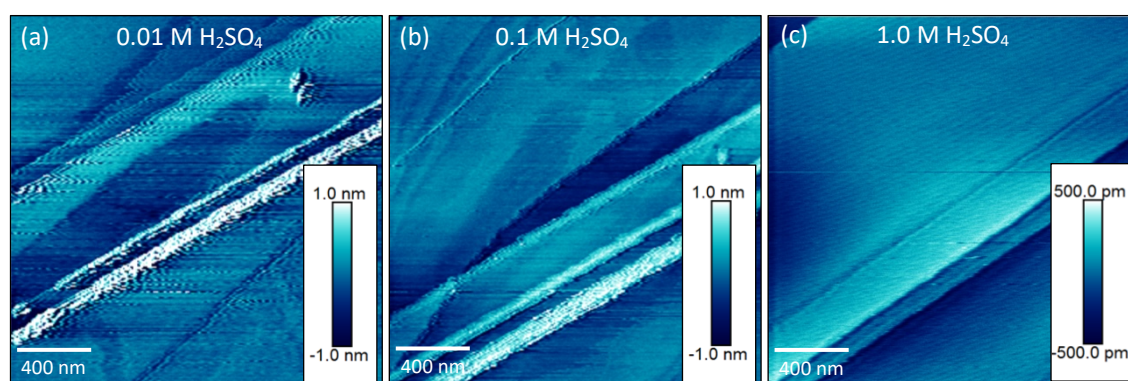


**Fig. 4.1:** SECPM images (500 nm x 500 nm, measured at NU) of a HOPG surface in different concentrations of H<sub>2</sub>SO<sub>4</sub> (a) 0.01 M, (b) 0.1 M, (c) 1.0 M. For comparability, the same tip and measurement parameters were used to record each image. However, different areas were scanned because the tip position shifts when electrolyte is exchanged. Microscope settings:  $U_{SP} = 50$  mV, Scan Rate = 1 Hz, Gains ( $i/p$ ) = 1/5,  $U_{WE} = -400$  mV vs. Pt.

The measurement was based on a 0.1 M H<sub>2</sub>SO<sub>4</sub> solution, because it was also used in most other SECPM experiments in this work. For the other images, the concentration was either

increased or lowered by one order of magnitude. In 1.0 M concentration (Fig. 4.1 (c)), all step edges appear clear and sharp and the terraces flat. When decreased to a 0.1 M concentration (Fig. 4.1 (b)), the step edges become rougher and image is generally noisier. After a further decrease to 0.01 M  $\text{H}_2\text{SO}_4$  (Fig. 4.1 (a)), the noise at the edges becomes much stronger and extends further onto the terraces. Because of the small forces exerted on the tip when the electrolyte was removed and refilled, the position of the tip shifted, preventing imaging of the same area in each concentration.

The conditions in each measurement vary slightly because of the Pt-wire reference electrode. Its potential changes with the pH value of the solution [104]. However, the total change in reference electrode potential between the lowest and highest concentration is only around 100 mV which does not affect the image quality much. Also, the effect of the RE potential would cause changes in the opposite direction to the observations made in the image series. A lower  $\text{H}_2\text{SO}_4$  concentration shifts the potential further away from the PZC, which would increase the image quality but in the measured images the quality is clearly better at higher concentrations. Therefore, the effect can be ignored in the discussion of the images.

While the EDL structure of ions in aqueous solution such as  $\text{H}_2\text{SO}_4$  is sufficiently described by the GCS model, the circumstances can be more complicated in other types of electrolytes such as ionic liquids. To analyze how the EDL structure in other liquids affects the SECPM images, a series of measurements in three different types of liquids (Fig. 4.2) was performed:

- De-ionized MilliQ water
- The organic solvent ethylene glycol and
- The ionic liquid BMP-TFSI

MilliQ water and ethylene glycol contain only very small amounts of ions, mainly in the form of impurities or from autopyrolysis, where two water molecules react with each other to form an  $\text{OH}^-$  and a  $\text{H}_3\text{O}^+$  ion. The ionic liquid on the other hand consists purely of ions and contains only trace amounts of water. The parallel lines that appear in all three scans over the whole image, less pronounced in Fig. 4.2 (c), are 50 Hz oscillations that can be picked up from the local power grid under certain conditions and are not relevant for the interpretation of the images. In MilliQ water in Fig. 4.2 (a), the image quality is good with sharp step edges and no noise besides the 50 Hz oscillations. MilliQ water can be viewed as an extreme case of a sulfuric acid solution with a 0 M concentration. Considering this, the SECPM image is of unexpectedly good quality compared to the images in sulfuric acid in Fig. 4.1. However, a direct comparison between these images should not be made because they were obtained under very different conditions. The working electrode potentials differ by several 100 mV, the setpoint potential was much

lower in MilliQ water and most importantly, different tips were used. The image in ethylene glycol (Fig. 4.2 (b)) is slightly noisier but the step edges still appear sharp. Here, the tip was not coated but the resulting faradaic currents are low enough not to disturb the imaging process because of the nature of the solvent. The final image in BMP-TFSI (Fig. 4.2 (c)) appears much sharper, partly because the 50 Hz oscillations are less pronounced and partly because of the lower working electrode potential which places the measurement further from the potential region with reduced image quality. However, some step edges appear covered with brighter spots that might be adsorbed material or an effect of the feedback gains. These images show that SECPM measurements can be performed in a wide range of different liquids when the right combination of settings is found.

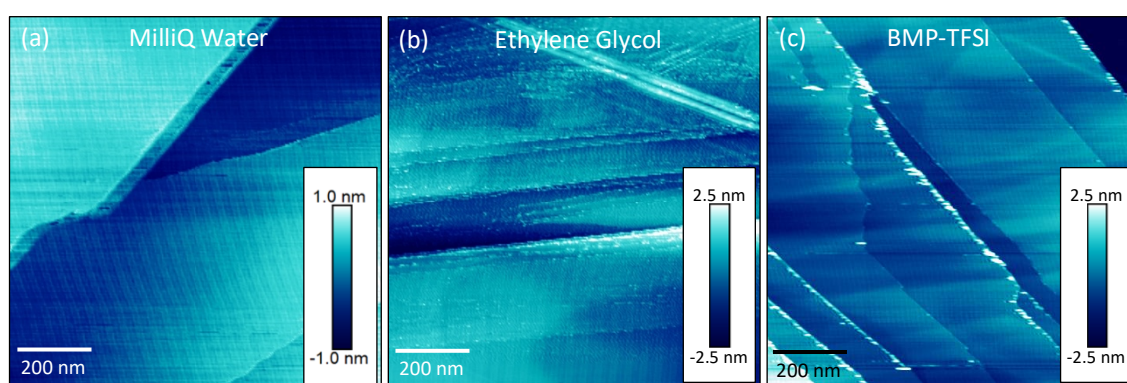


**Fig. 4.2:** SECPM images ( $1\ \mu\text{m} \times 1\ \mu\text{m}$ , measured at TUM) recorded in different electrolytes: **(a)** De-ionized MilliQ water, microscope settings:  $U_{SP} = 20\ \text{mV}$ , Scan Rate = 1 Hz, Gains = 1/2,  $U_{WE} = 0\ \text{mV}$  vs. Au/Au-oxide. **(b)** Ethylene glycol measured with an uncoated tip, microscope settings:  $U_{SP} = 100\ \text{mV}$ , Scan Rate = 1 Hz, Gains (i/p) = 1/2,  $U_{WE} = 100\ \text{mV}$  vs. Au/Au-oxide. **(c)** The ionic liquid BMP-TFSI, microscope settings:  $U_{SP} = 50\ \text{mV}$ , Scan Rate = 1 Hz, Gains (i/p) = 0.2/0.3,  $U_{WE} = -1200\ \text{mV}$  vs. Au/Au-oxide.

The decreasing image quality in the less concentrated  $\text{H}_2\text{SO}_4$  solutions in Fig. 4.1 can be explained by the differing extent of the EDLs in different concentrations. As described in section 2.1.2, the Debye length provides a measure for the thickness of the EDL and was used to estimate it for all three concentrations, using eq. ( 2.16 ):

- $\kappa^{-1}_{1M} = 0.30\ \text{nm}$
- $\kappa^{-1}_{0.1M} = 0.96\ \text{nm}$
- $\kappa^{-1}_{0.01M} = 3.04\ \text{nm}$

The larger double layer thickness in lower concentrations (at constant electrode potential) results in a flatter potential vs. distance curve. In this case, when the SECPM tip travels a certain distance normal to the HOPG surface, it experiences a smaller potential change in lower electrolyte concentrations which directly decreases the z-resolution. The tip also

reaches the setpoint potential at a larger distance from the surface which effectively reduces the lateral resolution. Within certain limits, the effects can be prevented by optimizing the SECPM settings. The setpoint potential can be decreased to bring the tip closer to the surface. Shifting the working electrode potential further away from the PZC generates a steeper potential curve.

The images series in (Fig. 4.2) shows that an EDL with a sufficient potential gradient is present in each of the analyzed liquids. Because their structures cannot be described by the GCS model, different mechanisms must be responsible for the EDL formation. As explained in section 2.1.3, the ions in the double layer in ionic liquids are ordered in a layered structure of alternating anion and cation layers. As a result of the lattice saturation effect, where the ions reach maximum density near the surface (see section 2.1.3), the potential curve often progresses flatter than in liquids with an EDL that follows the GCS model. Similar to the EDL structure in ionic liquids, in polar or polarizable liquids such as water the polar molecules align in layers of alternating orientation in the electric field around the electrode surface to form an EDL [105]–[107]. In this case, another factor contributing to the double layer structure are water molecules that become ionized in the strong electric field near the electrode surface [108]. Ethylene glycol on the other hand is not a polar liquid and does not contain any ions. It is possible here that enough impurities are present to still form a sufficient EDL for SECPM operation but further studies would be necessary to confirm this, using SECPM approach curves in different purity levels of ethylene glycol or similar liquids.

A possible explanation for the unexpectedly high resolution and the images in ethylene glycol can be found in the work of Traunsteiner et al. [61]. They report that the potentials measured by the SECPM tip are in fact the result of various leakage currents in the system and do not represent the potential profile of the electrochemical double layer. The currents cause a potential drop across the gap between tip and electrode that determines the measured potential. At larger distances, the main contribution to the current is a result of faradaic processes. However, when tip and sample are brought sufficiently close together, an STM-like tunneling current becomes the major influence. Because this current depends exponentially on the distance, the achievement of atomic resolution might be a realistic consequence. This model could also explain the good image quality in water, where the potential gradient in the double layer is expected to be much flatter than in any concentration of  $\text{H}_2\text{SO}_4$ . However, if this model is accurate it would mean that SECPM is effectively a variant of EC-STM without control of bias voltage and tunneling current. On the other hand, several factors speak against the tunneling model. Firstly, the high input impedance amplifier in the SECPM setup is specifically designed to specifically prevent the flow of such currents. Another reason can be found in the SECPM study of enzyme adsorption by Baier et al. [59]. In Figure 3, they present a comparison between an EC-STM and a SECPM image of several enzymes adsorbed on an HOPG surface. One of

the enzymes is only visible in the SECPM image but could not be detected by EC-STM and the resolution of details in the molecular structure is better in SECPM.

#### 4.1.2 Atomic Resolution

The highest previously reported resolution with SECPM was achieved in the detailed images of single molecules of the enzyme horseradish peroxidase on HOPG surfaces by Baier et al. [59]. It has been shown many times that the large, atomically flat terraces of an HOPG surface are ideal locations to achieve atomic resolution with STM [94]. Therefore, these surfaces were chosen to attempt the first atomic resolution with SECPM. Each tip was first tested in EC-STM. When a tip was found that repeatedly delivered atomic resolution images at several different positions on the HOPG surface, the microscope was switched to SECPM mode. Without changes to setup, an image was recorded at the same position under similar conditions. The working electrode potential was kept far from the potential window around the PZC to guarantee the best possible image quality. The scan rate was set very high and the gains were decreased close to zero for a quasi-constant height mode measurement. Only a small value was assigned to the integral gain to protect the tip from crashing into the surface. A low setpoint was chosen to position the tip close to the surface for optimal resolution (Fig. 4.3 (a)). Instead of the typically portrayed height information, the SECPM images in Fig. 4.3 (a) and (b) were measured in constant height mode and display the measured potentials directly. For atomic resolution, this mode of presentation often provides better contrast and makes the surface structure detectable more easily. Image (a) is relatively noisy and the influence of a fluctuating drift is evident. However, the periodic pattern of the atomic structure of the HOPG surface is clearly visible.

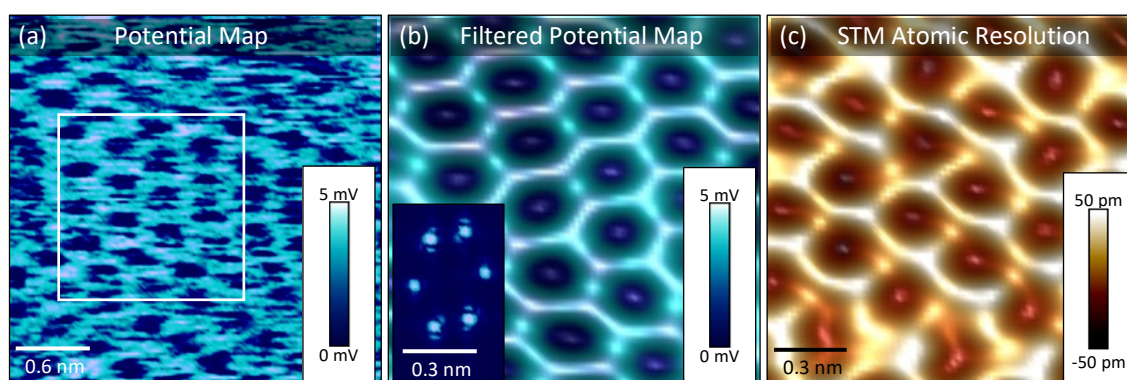


**Fig. 4.3:** (a) Atomic resolution SECPM potential map of a HOPG surface in 0.1 M  $H_2SO_4$ , measured in quasi-constant height mode (3 nm x 3 nm, measured at TUM). Microscope settings: Scan rate = 40 Hz, gains (i/p) = 0.1/0.0,  $U_{SP} = 15$  mV,  $U_{WE} = -1.0$  V vs Au/Au-oxide. (b) Fourier noise-filtered image of the area marked by a white square in (a), showing the hexagonal structure of the graphene layer (1.5 nm x 1.5 nm). The inset shows the Fourier-transformed image. (c) STM image in air of a HOPG surface in atomic resolution for comparison (1.5 nm x 1.5 nm, measured at TUM CREATE). Microscope settings: Scan rate = 20 Hz, gains (i/p) = 0.1/0.0,  $I_{SP} = 1$  nA,  $U_{Bias} = 100$  mV.

For (b), the area marked by the white square has been Fourier-transformed (FFT), noise filtered (inset) and finally transformed back with inverse FFT. For comparison, an atomic resolution STM image of a HOPG surface is shown in (c). It has been noise-filtered with the same method as (b). The striking similarities between SECPM and STM image confirm that SECPM is indeed capable of atomic resolution. The SECPM image appears sharper than the one recorded with EC-STM but because different tips were used for the measurements, this should not be interpreted as superior SECPM image quality over EC-STM.

## 4.2 Step Edge Oscillations

During SECPM measurements on HOPG surfaces an oscillation effect can frequently be observed at step edges. Its amplitude slowly decreases with a larger distance from the edge until it disappears after several oscillations. The number of visible maxima and the distance between them appears to be influenced by various measurement parameters and microscope settings. To find the cause of the oscillations and to determine if they are a measurement artifact or an actual potential effect, several SECPM image series were recorded with a systematic variation of different parameters.

### 4.2.1 Size and Shape

The oscillations were mainly observed on HOPG surfaces but have also been found in SECPM measurements at step edges on Au(111) surfaces. Therefore, it can be excluded that the effect is material-specific to HOPG. Fig. 4.4 (a) shows an example SECPM scan of an HOPG step edge with large oscillations towards the left side of the step edge. For comparison, an EC-STM scan of the same area, recorded immediately before the SECPM image, is shown in Fig. 4.4 (b). The example images show that the oscillations can only be observed in SECPM which already indicates that the oscillations are an artifact. However, the possibility cannot be ruled out that a to this point unknown oscillation in the potential structure of the EDL, caused by the presence of the step edge and picked up by the SECPM tip, is the reason for the observed structures. To quantify the influence of each microscope parameter on the oscillations, a line profile perpendicular to the step edge was taken from each image. The amplitude and distance of the peaks were measured from these profiles and compared to each other. Fig. 4.5 shows a typical SECPM image of an HOPG step edge (a) and the line profile extracted from the marked area (b). Because the step edges often appear uneven and the oscillations can differ in intensity along a step edge, the line profiles were averaged over the width of around 100 nm along a straight step edge for a better comparability of the results.

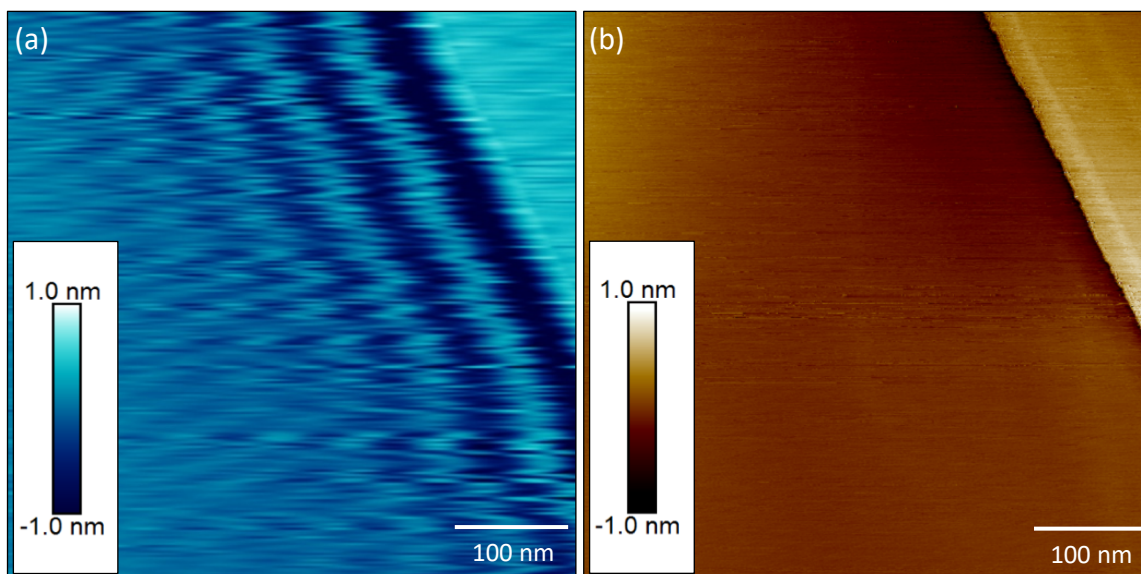


**Fig. 4.4:** Comparison of an SECPM **(a)** and an EC-STM **(b)** image of the same HOPG step edge in a 0.1 M  $H_2SO_4$  solution (500 nm x 500 nm). The SECPM image was recorded immediately after the EC-STM image, using the same tip. Microscope parameters: **(a)** Scan rate = 1 Hz, Gains (i/p) = 5/8,  $U_{WE} = -400$  mV vs. Pt,  $U_{SP} = 5$  mV **(b)** Scan rate = 2 Hz, Gains (i/p) = 0.5/1,  $U_{WE} = -400$  mV vs. Pt,  $I_{SP} = 1$  nA,  $U_{Bias} = 100$  mV (measured at TUM-CREATE).

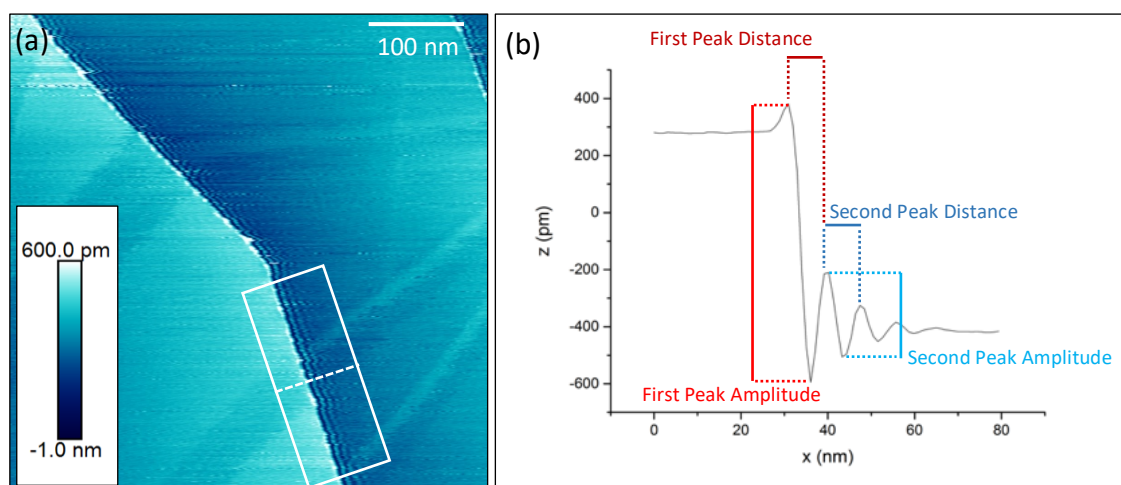


**Fig. 4.5:** **(a)** SECPM image (trace) with step edge oscillations of a HOPG surface in 0.1 M  $H_2SO_4$  (500 nm x 500 nm). The white rectangle shows the area that was used to generate the averaged line profile which is shown in **(b)**, the dashed line indicates its direction. Microscope settings: Scan rate = 2 Hz,  $U_{SP} = 5$  mV,  $U_{WE} = -400$  mV vs. Pt, Gains (i/p) = 5/8 (measured at TUM-CREATE).

It becomes evident from the line profile shown in Fig. 4.5 (b) that the amplitude of the oscillation peaks decreases with distance from the step edge until the profile flattens and turns into the HOPG basal plane. To obtain comparable values from the recorded images and line profiles, the peak amplitude and distance were measured as shown in the image. The amplitude of the first peak was measured between the small maximum directly at the step edge and the first minimum. The peak distance was recorded between the same

maximum and the following peak. The same values were also measured for the second maximum, on the one hand to obtain more data and on the other hand to locate possible differences between the result for the first and second peak. To analyze the oscillations, several image series were recorded, each with variation of a different microscope parameter. For comparable results, all experiments were performed in a 0.1 M H<sub>2</sub>SO<sub>4</sub> solution.

#### 4.2.2 Influence of Measurement Parameters

As mentioned above, the oscillations always appear after the tip scans over a step edge. To determine if and how their appearance differs when the step edge is scanned from upper to lower terrace or vice versa, two images were recorded with opposite scan directions (Fig. 4.6), the so-called *trace* (scan direction from left to right) and *retrace* (scan direction from right to left) images.

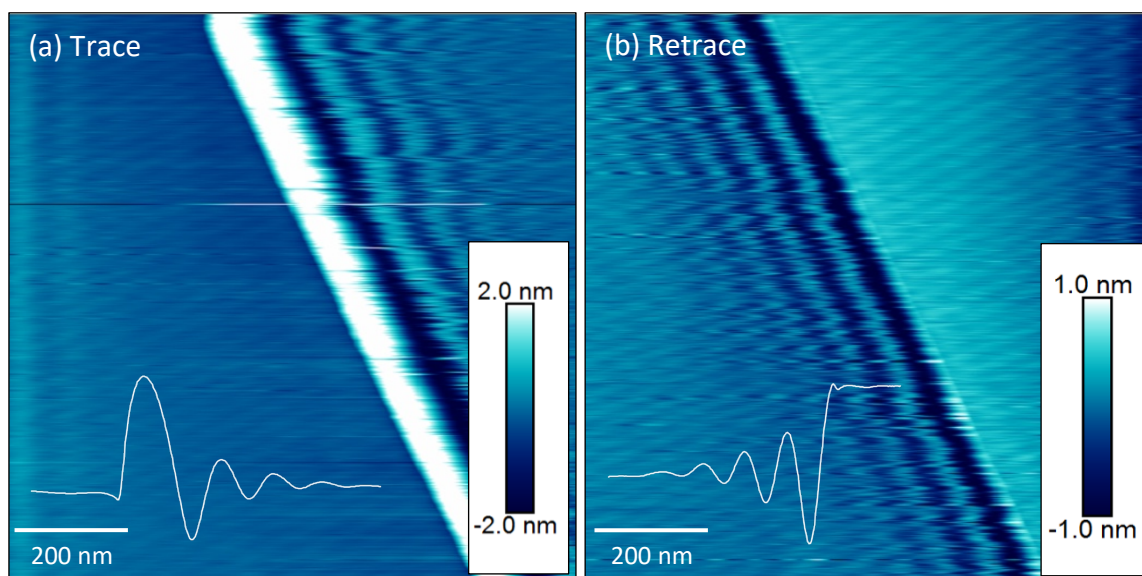


**Fig. 4.6:** SECPM images of an HOPG step in a 0.1 M H<sub>2</sub>SO<sub>4</sub> solution (1 μm x 1 μm) showing the typical oscillation behavior ((a) Trace, (b) Retrace). The upper terrace is located to the right of the step edge, the lower terrace to the left. The line profiles perpendicular to the edge are shown as white curves over the images (not to scale). Microscope settings:  $U_{WE} = -400$  mV vs. Pt, Scan rate = 2 Hz, Gains ( $i/p$ ) = 5/8,  $U_{SP} = 5$  mV (recorded at TUM-CREATE).

The most evident finding here is that the direction of the oscillations depends on the scan direction. They always proceed in the direction of the scan. This observation already confirms that the effect cannot be caused by a potential structure within the EDL and is also not a surface feature as was already shown by the comparison with EC-STM. Another interesting observation is that amplitude of the first maximum is much higher when scanning from the lower to the upper terrace (4 nm) than in the opposite direction (1.5 nm). The following peaks show a similar amplitude ratio. The distance between the

maxima is not affected and remains the same throughout both images. The parallel diagonal lines found in both images are the known 50 Hz oscillations of the power grid that can in some situations be picked up by the imaging mechanism and are not relevant for this analysis. When a good tip is used and the microscope settings are optimized, their intensity can be reduced. However, this also reduces the probability of the step edge oscillations to appear.

In the second image series, the scan rate was varied, i.e. the number of line scans performed per second. The resulting images with increasing scan rate are shown in Fig. 4.7. The according line profile of each image is overlaid as a white curve in each image. Since the microscope automatically records a trace and a retrace scan each time, a rate of 1 Hz corresponds to one line scan in trace direction and one in retrace direction within one second. In general, lower scan rates are expected to provide a better image quality with the drawback of longer imaging times. In this work, each image consists of 512 x 512 data points. Therefore, it takes almost 9 minutes to record an image at 1 Hz where even a slow drift can cause large distortions in the images. Because the differences between trace and retrace images have already been examined in the previous section, only the trace images will be shown in the following image series.

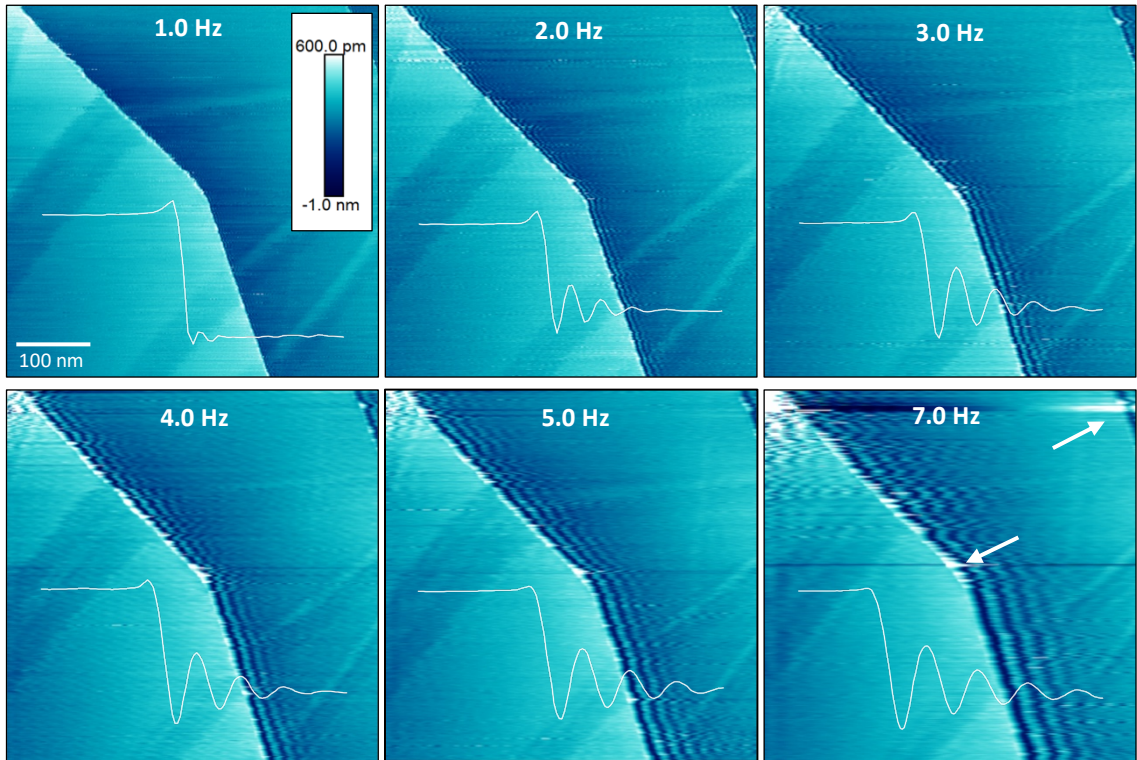


**Fig. 4.7:** SECPM image series (trace direction, 500 nm x 500 nm) of an HOPG surface in a 0.1 M  $H_2SO_4$  solution with varied scan rates. The white curves show the averaged line profile extracted from each scan (not to scale). Microscope settings: Gains (i/p) = 3/4,  $U_{SP} = 50$  mV,  $U_{WE} = -400$  mV vs. Pt, (recorded at TUM-CREATE).

At low scan rates, the oscillations are small, almost vanishing completely at 1 Hz. With increasing scan rates, they extend further away from the step edge until they cover a several 100 nm wide area. At the same time, the sharpness of the images decreases and fringe-like artifacts appear at the step edge. They point in scan direction and become more numerous and larger at faster scan rates as shown by the white arrows in Fig. 4.7 (7 Hz). This effect is most likely a direct cause of the high scan rate when the feedback loop is not able to adjust the tip height quickly enough to accurately resolve the sharp edge. Similar features have also been found in EC-STM measurements and therefore they are not considered relevant for this study.

The next image series was recorded with varied feedback gains (Fig. 4.8). The gains control the height adjustments of the tip in response to changes in the distance to the surface during the scan. For this measurement, the proportional gain was kept two units higher than the integral gain.

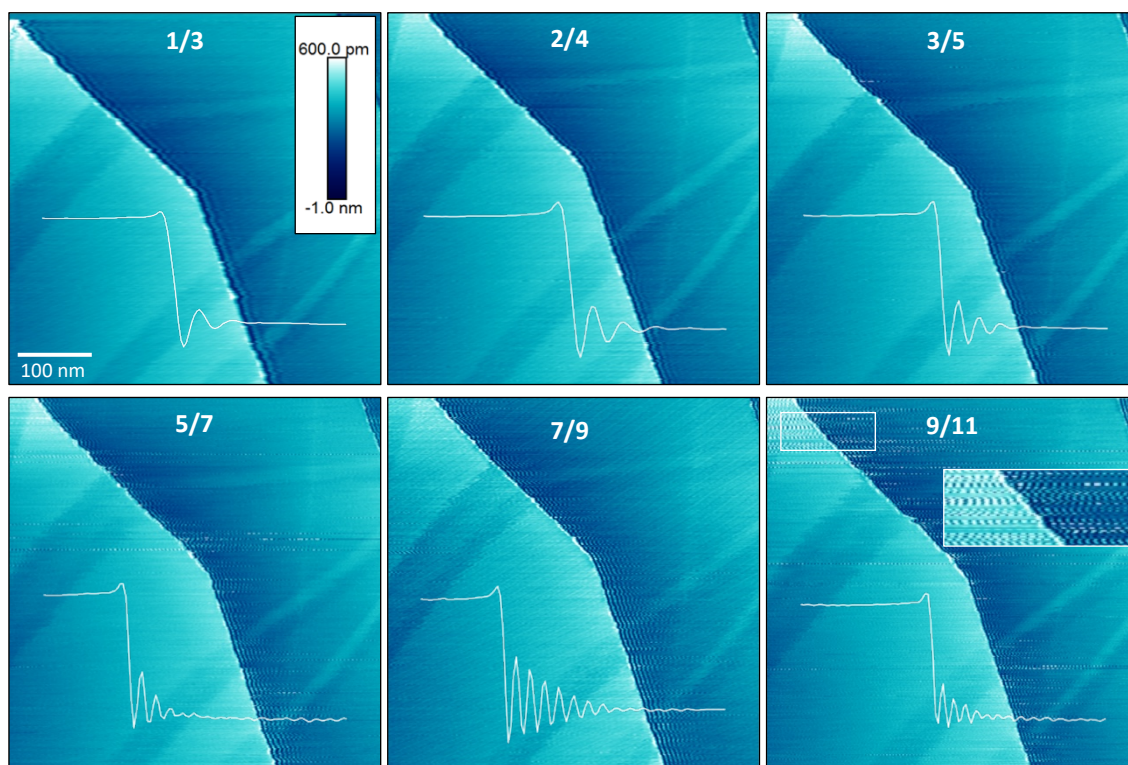


**Fig. 4.8:** SECPM image series (trace direction, 500 nm x 500 nm) of an HOPG step edge in a 0.1 M  $H_2SO_4$  solution with increasing feedback gains ( $i/p$ ), shown in the top left corner of each image. The line profiles for each scan are again shown as white curves (not to scale). Microscope settings: Scan rate = 2 Hz,  $U_{WE} = 50$  mV vs. Pt,  $U_{SP} = 5$  mV (recorded at TUM-CREATE).

These images were recorded under the same conditions as the previous scan rate series at the same position on the HOPG surface. In this case, while the size of the oscillations appears to remain constant, the number of visible maxima increases with the gains. The step edge appears sharper at higher gains due to the faster response by the feedback

loop. At very high gain values, the extent of the oscillations begins to vary with the number of visible maxima ranging from three to over ten. In extreme cases, they can even be found on both sides of the step edge (Magnified area in Fig. 4.8 (9/11)). This is a known effect that emerges when the gains are set too high, making the tip oscillate over large areas of the whole image with a similar appearance as the step edge oscillations.

In Fig. 4.9, the setpoint potential of the measurement was varied. It describes the constant potential difference between tip and sample at which the image is recorded. Therefore, a higher  $U_{SP}$  stands for a larger distance. The dotted white line in the 10 mV image shows the step edge from which the line profiles were extracted.

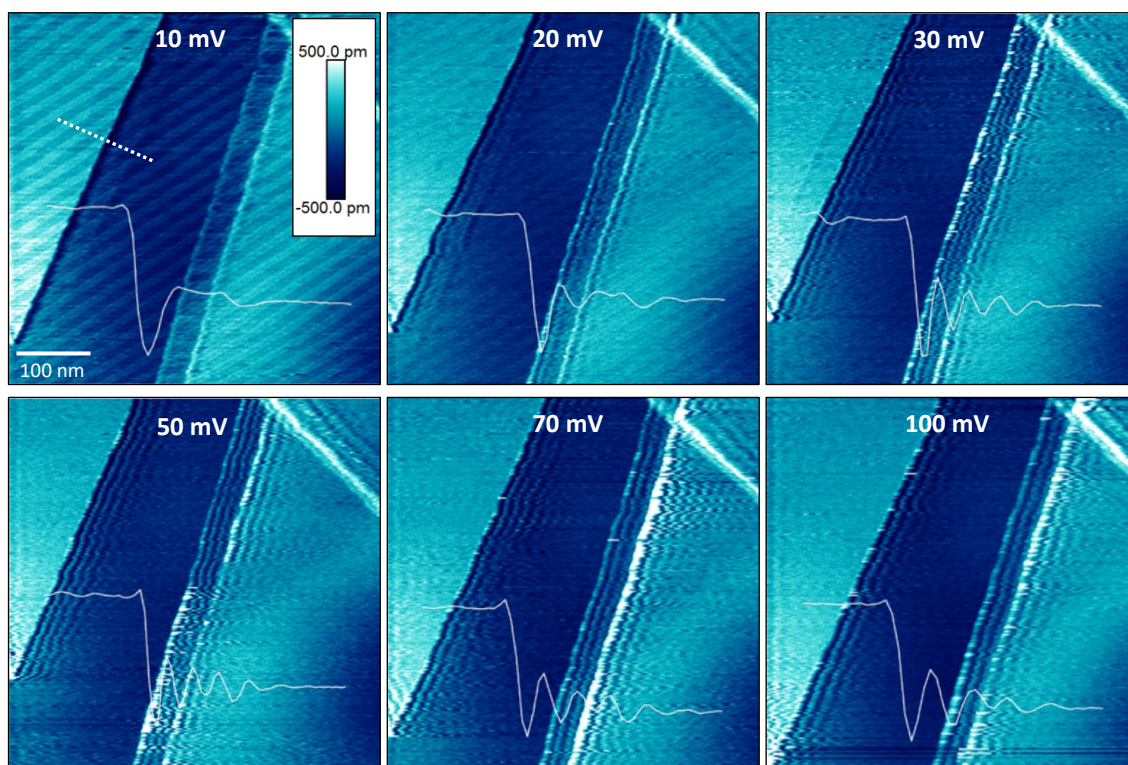


**Fig. 4.9:** SECPM image series (trace direction, 500 nm x 500 nm) of an HOPG step edge in a 0.1 M  $H_2SO_4$  solution with varied setpoint potential. The dotted line in the 10 mV image marks the step edge at which the line profiles, embedded in each image as a white curve, were extracted (not to scale). Microscope settings: Scan rate = 2 Hz, Gains (i/p) = 1/3,  $U_{WE} = -400$  mV vs. Pt (recorded at NU).

The 50 Hz oscillations can be observed again in this series. They are strongest at the lowest setpoint and their intensity decreases at higher  $U_{SP}$  at which also the white features at the step edge are observed again that were previously shown in Fig. 4.7 (7 Hz). The best image quality is achieved at  $U_{SP}$  between 30 mV and 50 mV. The size of the step edge oscillations does not appear to be affected much by the changes in setpoint potential.

In the final image series, the working electrode potential was varied in steps of 200 mV (Fig. 4.10). The bottom of the imaged area consists of several broken and folded graphene sheets and is therefore not ideal for an analysis of the oscillations. However, in the top half, a single step edge extending several 100 nm provides a good location (indicated by the dotted, white line in the -200 mV image).

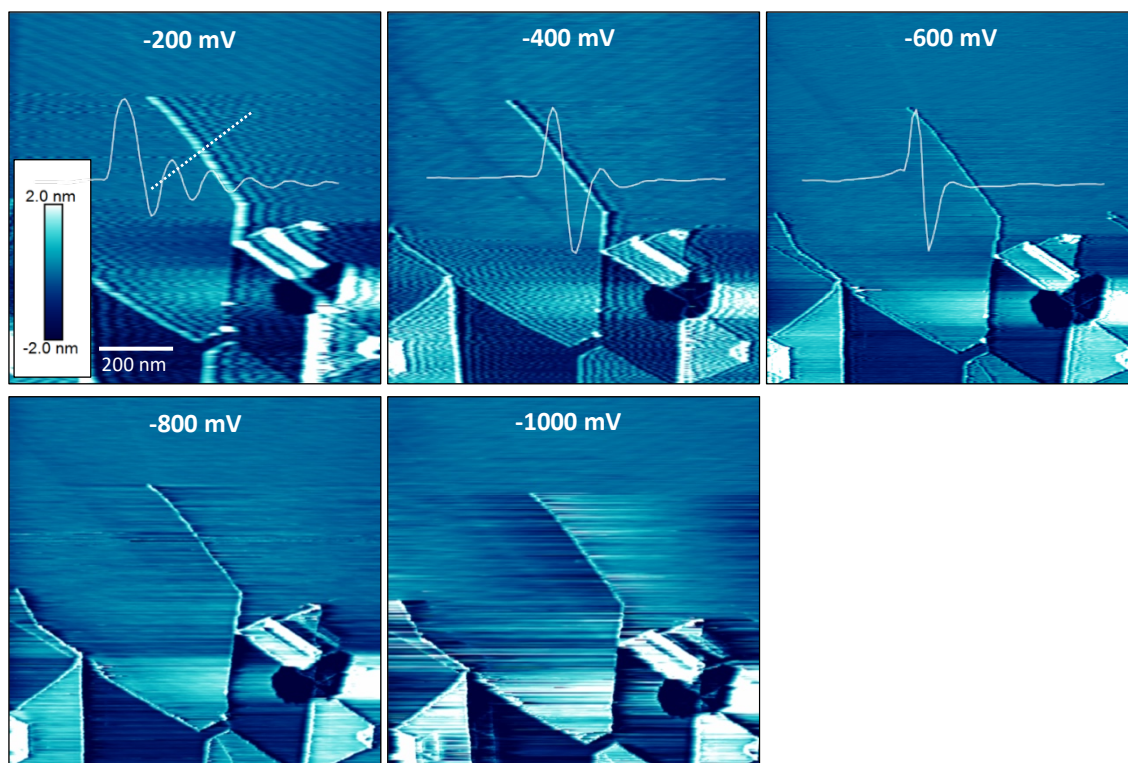


**Fig. 4.10:** SECPM image series (trace direction,  $1 \mu\text{m} \times 1 \mu\text{m}$ ) of an HOPG step edge in a  $0.1 \text{ M H}_2\text{SO}_4$  solution with varied working electrode potential. The white dotted line in the  $-200 \text{ mV}$  image indicates the position the line profiles, embedded in each image as a white curve, were extracted from (not to scale). Microscope settings: Scan rate = 2 Hz, Gains (i/p) = 5/10,  $U_{\text{SP}} = 5 \text{ mV}$  (recorded at TUM-CREATE).

An attempt was also made to obtain another image at 0 mV, but at this potential the tip cannot engage. Most likely, the PZC is too close to the working electrode potential for SECPM measurements in that case. Interestingly, the oscillations are only clearly visible in the first two images with the highest setpoint potentials and the number of visible maxima decreases rapidly with  $U_{\text{WE}}$ . At the lower potentials, horizontal lines start appearing around all edges instead.

### 4.2.3 Line Profile Analysis

To allow a direct comparison of the line profiles obtained from the microscope images, a quantifiable analysis of the oscillations is necessary. Using the method introduced in Fig. 4.5, amplitude and distance of the first and second maximum were measured and plotted

against the according varied parameter. In Fig. 4.11, the peak analysis results of the scan rate image series for both trace and retrace images are presented.

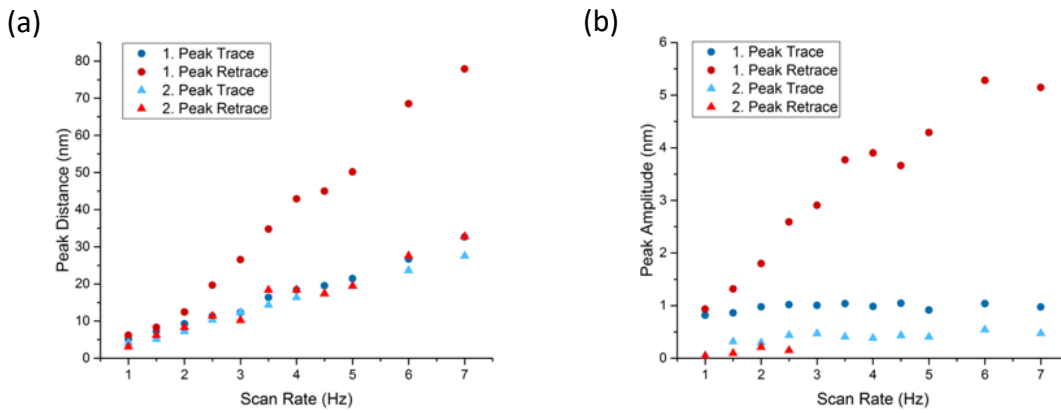


**Fig. 4.11:** Measured oscillation peak distance (a) and amplitude (b) of the scan rate image series (Fig. 4.7) using the method presented in Fig. 4.5. Analyzed were the first (circles) and second (triangles) maxima of both trace (blue) and retrace (red) images.

The analysis of the peak distance (a) shows a linear increase with the scan rate in all cases. However, the increase is much stronger for the first peak in retrace direction, while the values for the other three measured peaks are very close to each other. A similar behavior can also be observed in the amplitude data (b). In this case, the difference is even stronger because only the first peak retrace curve shows any increase at all while the other three peaks remain at a constant value. This diverting behavior is caused by the disproportionately large first peak in retrace direction that was shown in Fig. 4.6. The effect is found in all line profiles of scans in which the step edge is passed in upward direction and becomes stronger when the scan rate is increased. At higher scan rates, the peak's size increases enough that it also distorts the second maximum so much that reliable amplitude measurements are no more possible. Thus, at scan rates of 3 Hz and above, amplitude values for the second peak in retrace direction could not be extracted. Because the feedback gains were kept constant throughout the experiment, at higher scan rates the feedback loop is not able to adjust the tip height fast enough to clearly resolve the surface. After an initial overcompensation of the height change, the mechanism returns only slowly to the setpoint distance, making any surface structure appear both higher and wider than it actually is. This also causes the appearance of the typical lines and fringe-features after step edges or particles (e.g. Fig. 4.7 (7 Hz)). It can be concluded that the effect is not connected to the step edge oscillations and that it is better to omit the deviating first peak retrace data in the evaluation of the data. The same line profile analysis method was used for an analysis of the oscillation peaks of the feedback gain image series (Fig. 4.12).

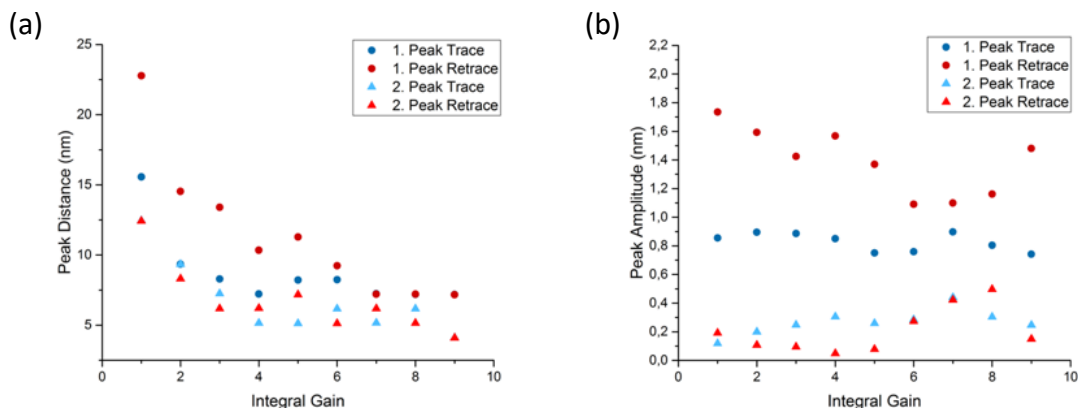


**Fig. 4.12:** Measured oscillation peak distance **(a)** and amplitude **(b)** of the feedback gain image series (Fig. 4.8) using the method presented in Fig. 4.5. Analyzed were the first (circles) and second (triangles) maxima of both trace (blue) and retrace (red) images.

The peak distance decreases strongly with increasing feedback gains at lower gain values. At higher gains the curve exhibits an only slowly decreasing nearly constant behavior. Again, the first peak retrace curve deviates from the other three curves. However, the difference is much smaller than in the scan rate series. The effect causing the large first peak when the step edge is passed in upward direction is countered to a certain extent by increasing the feedback gains which causes a faster adjustment of the tip height. This explains the stronger deviation at lower gains, while at higher gains the values of all four curves are similar. As in the scan rate series, the peak amplitude is not affected by the feedback gain changes. The peak amplitude curves of the scan rate series only appear flatter in Fig. 4.11 than here because of the different height scales used in the graphs.

Both scan rate and feedback gain are purely internal parameters of the microscope system, the setpoint and working electrode potentials on the other hand directly affect the conditions inside the electrochemical cell. This difference might provide further indications on the origin of the step edge oscillations. The line profile analysis for the setpoint potential image series is shown in Fig. 4.13. In the microscope images of the setpoint potential series in Fig. 4.9, an increasing number of oscillation peaks is observed at higher  $U_{SP}$ . However, the analysis of the maxima in the line profiles shows that both peak distance and amplitude are stable throughout the varied  $U_{SP}$  range. In this case, only images in trace direction were recorded. The small fluctuations in the measured values can be explained by the limited lateral resolution of the microscope images. The line profile analysis from each image series shows that the oscillation amplitude does not change from parameter variations in any experiment, only the distance between the maxima is affected. A measurement of the peak distance in nanometer is not suitable for a comparison when different scan rates are used. An oscillating tip would let the maxima appear closer to each other at lower scan rates, simply because it moves a shorter distance while it performs a single oscillation. Therefore, an effective oscillation frequency

$v_{eff}$  (oscillation peaks per second) was calculated from the peak distance data for better comparison:

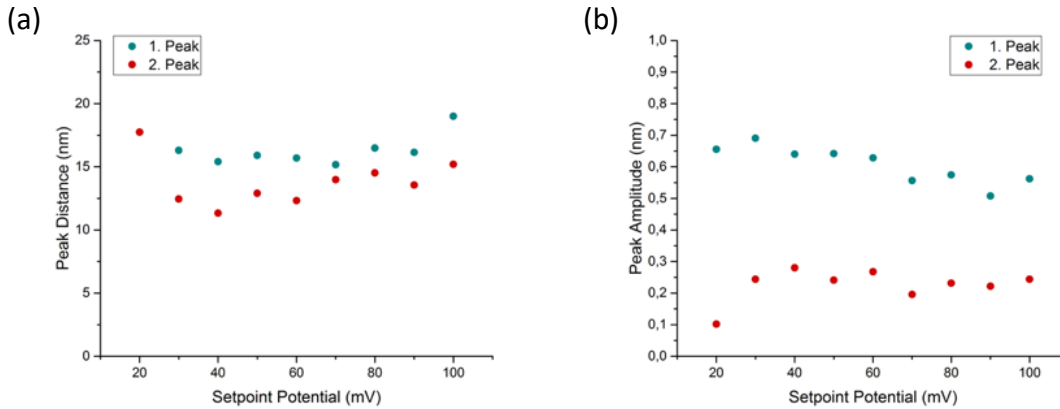


**Fig. 4.13:** Measured oscillation peak distance **(a)** and amplitude **(b)** of the setpoint potential image series (Fig. 4.9) using the method presented in Fig. 4.5. Analyzed were the first (circles) and second (triangles) maxima in trace direction.

$$v_{eff} = \frac{2ar}{d} \quad (4.1)$$

using the image size  $a$ , the scan rate  $r$  and the peak distance  $d$ . The converted effective oscillation frequency curves from all three image series are plotted together in Fig. 4.14. Since the behavior of the data does not differ much for the individual analyzed maxima within each image series, an average curve was calculated for each series. The effective oscillation frequencies of scan rate (blue) and setpoint potential (green) does not show any dependence on the varied parameter. The variation of the feedback gains (red) on the other hand clearly influences the step edge oscillations with higher gain values resulting in a higher  $v_{eff}$ . With the feedback gain being the only parameter that affects the appearance of the step edge oscillations, it can be confirmed that the effect is indeed an artifact. The feedback loop, a component of the microscope that has no influence on the electrochemical conditions inside the cell, keeps the tip-sample distance constant during the measurement. The most probable explanation for their appearance is therefore that the scanning of a sharp step edge in SECPM can cause the feedback loop to overcompensate for the height change under certain conditions. The tip height is adjusted too much, causing the feedback-loop to initialize a counter-adjustment with lower amplitude that is too strong as well. This continues for several repetitions until the effect becomes too small to be observable. An examination of the final image series (Fig. 4.10) with varied working electrode potential gives some insight into the conditions under which the oscillations occur. The images indicate that the oscillations are only found in a certain range of  $U_{WE}$  and that the number of visible maxima increases when the potential approaches the region around the PZC in which SECPM measurements are not possible.

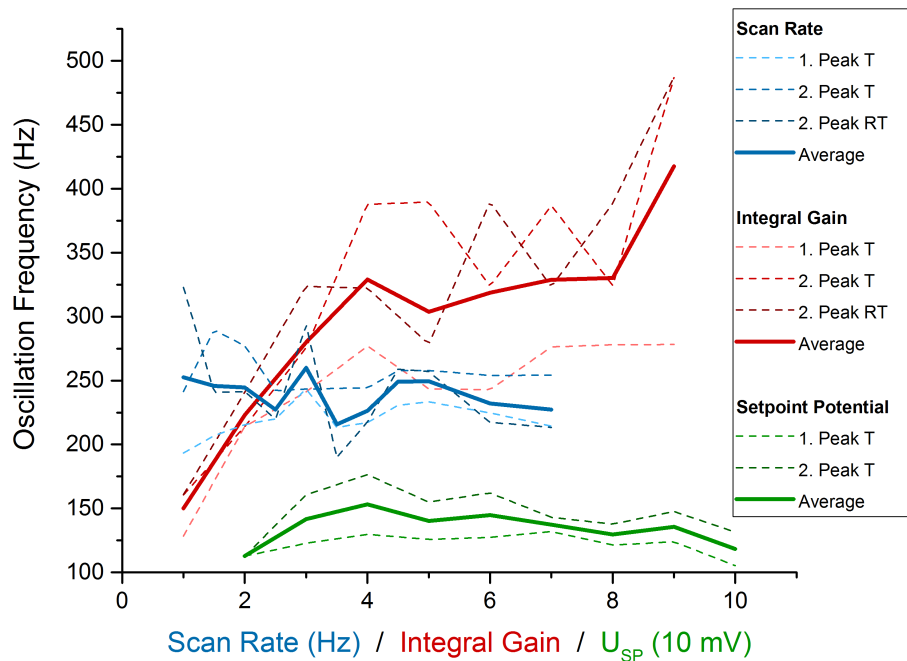


**Fig. 4.14:** Effective oscillation frequency curves calculated from the measured peak distances of the scan rate, integral gain and setpoint potential series, each plotted over the according parameter. The thick, solid curves are calculated average values from the individual trace and retrace data ( $T = \text{trace}$ ,  $RT = \text{retrace}$ ) of the first and second peak, plotted as dashed lines.

On a smaller scale, a similar behavior can also be found in the setpoint potential image series, where the number of visible maxima increases with  $U_{SP}$ . It appears that the step edge oscillations are more likely to appear and increase the number of visible maxima when the potential gradient in the EDL is smaller. This is the case for higher  $U_{SP}$  as well as for  $U_{WE}$  close to the PZC. These findings suggest that the feedback loop system only functions properly when the z-resolution is high enough and that under certain conditions in SECPM, the potential gradient falls below this threshold. It has been observed that the occurrence of the oscillations is also linked to the tip quality. With some tips, the parameters have to be adjusted to extremely high or low values in order to initiate the oscillations, while other tips would still oscillate at potentials far from the PZC at low setpoint values. This indicates that the shape of the tip, its exposed surface area and the length of the exposed part of the tip all affect the measured potentials and thus the z-resolution.



## 5 Influence of Water on the Double Layer Capacitance of an Ionic Liquid

The shapes of measured *Double Layer Capacitance* ( $C_{DL}$ ) vs. potential curves of several ILs by different groups showed unexpected deviations and, in some cases, were not even consistent throughout a single experiment [4], [5]. Suspected causes of the problem were varying levels of contamination, mainly with water, but also possible unwanted reactions occurring at certain potentials [112], [134]. To clarify the situation and confirm the actual cause of the deviations, the influence of the presence of water in an IL on its double layer capacitance will be investigated. The measurements are performed in a potential region in which no faradaic reactions occur. Small amounts of water were added to a dried ionic liquid and its double layer capacitance at an Au(111) single crystal electrode was measured with *Electrochemical Impedance Spectroscopy* (EIS). The resulting  $C_{DL}$  vs. potential curves were then compared to curves derived from a simple mean field model. A peak found in the measured capacitance curves was suspected to be caused by a surface reconstruction of the Au(111) surface. The high resolution of EC-STM allows to detect the occurrence of a surface reconstruction. Therefore, the method was used to study potential dependent changes in the Au(111) surface. The results presented in this chapter were published in [113] and the supporting information [103].

### 5.1 Water in Ionic Liquids

Although many ionic liquids are hydrophobic and therefore immiscible with water, they are often hygroscopic in reality and absorb water from the ambient air [114]. The presence of even small traces of water can have a strong influence on the properties of the IL such as its polarity, conductivity and viscosity. However, when it comes to the field of energy storage research, the most important effect is a drastic decrease of the width of the electrochemical window. Generally, the large window is considered one of the great advantages of ILs over conventional electrolytes [115]. Water as an impurity in different ILs and its effect on the physical properties of the bulk ionic liquid have been thoroughly studied [116]–[119]. Also, the structure and interactions of water molecules in ILs were analyzed [120]–[124]. The solubility of water depends mainly on the type of anion in the ionic liquid and the water molecules often form hydrogen-bonds with two anions simultaneously [121]. It was found that at low concentrations of water, the ionic liquid can be induced to form organized nanostructures until, with increasing water content, a turnover point is reached and the structural organization decreases again. At this point, when the water concentration is sufficiently low the water molecules disturb

the short range order of the IL by positioning themselves in the form of molecule clusters at the preferential ion-ion interaction sites, the hydrophilic moieties, where they form a hydrogen bonded network [120], [125].

The conditions at the electrode-ionic liquid interface can differ significantly from the bulk IL. Since it is practically impossible to completely remove water from an ionic liquid, it is of particular importance for electrochemical applications to understand how its presence affects structure and properties of the electrochemical double layer. Simulations of the water distribution near the electrode showed an enrichment of water at the surface that increases with the surface charge density and an asymmetry in the amount of adsorbed water between positively and negatively charged electrodes was discovered [126]–[128]. Molecular dynamics simulations by Feng et al. [126] of imidazolium-based ionic liquids on multi-layered graphene electrodes showed that the distribution of water molecules depends on their interaction with the electric field in the double layer, driving them towards the absolute maxima of the field. The water also accumulates at positions where it has access to highly charged moieties of the ions and at any available free space in the liquid near the surface. These factors also depend on the size, shape, structure and charge distribution of the ions which again are affected by the electrode polarization [126]. The theoretical models were confirmed experimentally by Motobayashi et al. [129] and Zhong et al. [130]. Motobayashi et al. used surface-enhanced infrared absorption spectroscopy in combination with electrochemical methods. They found that the water molecules accumulate at the interface and form a strong hydrogen-bond network, even at low concentrations. As predicted by the simulations, the water accumulation depends on the sign and strength of the electrode polarization. It is linked to the exchange between cations and anions in the first layer of ions which is also driven by the electrode potential. The stronger bonds between water and anion lead to an increased water content when the first ionic layer consists mainly of anions. They also found that the presence of water facilitates the anion-cation exchange in the EDL by reducing coulomb forces between them and between ions and electrode. Zhong et al. analyzed the layered structure of *1-Butyl-1-Methyl Pyrrolidinium Bis(trifluoromethylsulfonyl)amide* (BMP-TFSA) near an Au(111) electrode surface with AFM force curves. They discovered ordered structures between three and five ionic layers wide. The two layers closest to the surface are charged while the remaining ones are neutral. The force required to penetrate the two charged layers closest to the surface varied with the potential because of the accumulation of water, with the first layer showing a stronger dependence than the second. The stiffness of these layers also decreased when the water content was increased which indicates that it causes a reduction of the coulomb forces between cations, anions and electrode. The thickness of the two charged layers increases with a higher water content while the thickness of the one to three remaining neutral layers is unaffected.

Electrochemical impedance spectroscopy is an important method for obtaining information about the EDL by determining the double layer capacitance and its dependence on the electrode potential. Much effort has been put into EDL capacitance measurements in ionic liquids with EIS [4], [5], [112], [131]–[133] and other methods. However, the results often contradict each other or in some cases were not even reproducible within a single study [4], [5]. The resulting capacitance-potential curve shapes range from camel shape to bell shape and others (introduced in section 2.1.3). While this might be caused partially by the different ILs, other influences such as experimental methods, electrode interfaces and equivalent circuits used in the experiments, contaminations of the ILs with water or other substances and reactions taking place within the large potential window must also be considered as possible reasons [112], [133]. To avoid most of these problems, the potential range of the measurement was reduced to a region where no other reactions are taking place in the IL-electrode system and controlled the water content to analyze its influence on the double layer capacitance.

## 5.2 Electrochemical Measurements

### 5.2.1 Reference Electrode Stability

Especially in longer experiments, it is important to use a stable reference electrode to obtain reliable results. Therefore, the stability of the Pt-wire's potential that was used in the EIS measurements as quasi-RE was analyzed by measuring the equilibrium potential of the ferrocene/ferrocenium couple in the same cell setup used for impedance spectroscopy. A 0.5 mM ferrocene solution was made from the dry BMP-TFSI inside the glove box. As in the double layer capacitance measurements, different amounts of water were added to the IL before it was filled into the cell. To determine the electrode's stability over longer time, five subsequent cyclic voltammograms were recorded. The positions of the ferrocene/ferrocenium peaks were then compared between each of them (Fig. 5.1 (a)). The influence of the water content was analyzed by comparing the peak positions in measurements with different water contents in the IL (Fig. 5.1 (b)). The stability measurements show that the Pt-wire potential remains stable during a single measurement (Fig. 5.1 (a)). The location of the ferrocene redox peaks does not change throughout several potential cycles. However, a comparison of the results from measurements with different water content in the IL (Fig. 5.1 (b)) revealed that the ferrocene redox peak potential varies from measurement to measurement. The position of the peaks seems to fluctuate randomly without any recognizable influence by the water content. Therefore, it has to be concluded that the Pt-wire's potential, while being stable during a single measurement, changes between to separate measurements. In order to

compare the results from different samples, the capacitance-potential curves will therefore be normalized to a common feature (the method will be described in section 5.2.3).

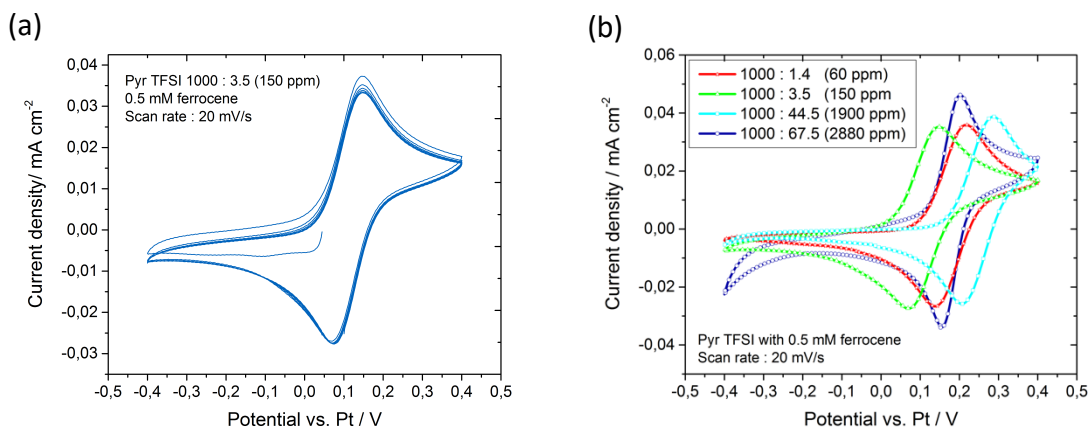


**Fig. 5.1:** (a) CV (5 cycles) of BMP-TFSI with a water content of 1000 : 3.5 and 0.5 mM ferrocene. The ferrocene reaction redox peaks remain stable throughout the measurement. (b) CVs of BMP-TFSI with 0.5 mM ferrocene and different amounts of water added. The potential of the ferrocene redox peaks changes from measurement to measurement. This graph has been published in [103].

## 5.2.2 Cyclic Voltammetry

To determine a suitable potential region for the double layer capacitance measurements in the BMP-TFSI - Au(111) system, CVs in a fairly large potential window of -1.2 V to 1.2 V vs. Pt were recorded with different amounts of water added to the IL (Fig. 5.2). The thick blue curve shows the CV of the dry ionic liquid (1.4 water molecules for each 1000 BMP-TFSI anions and cations) on a smaller current scale. The CVs are located completely within the stable potential window of BMP-TFSI and are therefore expected not to contain any major features. However, the curves show several peaks in the observed potential range. The simple explanation for this counterintuitive observation is that the flat non-faradaic region presented in many CVs of ILs has been shown to only appear flat due to the large scale generally used in their presentation [112]. Both anodic and cathodic currents increase when more water is added to the system and even the dry IL shows the presence of several redox waves. The anodic peak around -0.4 V vs. Pt is only observed after reduction at -1.0 V vs. Pt. In consequence, the relatively flat potential region between -0.4 V and +0.1 V was chosen for the EIS measurements. Immediately before and after each EIS measurement, a CV in the same potential range was recorded at 20 mV/s to find out if the EIS experiments had caused any permanent changes in the system. Starting at OCP, the electrode potential was first decreased to -0.4 V vs. Pt and then reversed to 0.1 V vs. Pt. As an example, a comparison of the CVs recorded before and after EIS at two different water contents is shown in Fig. 5.3.

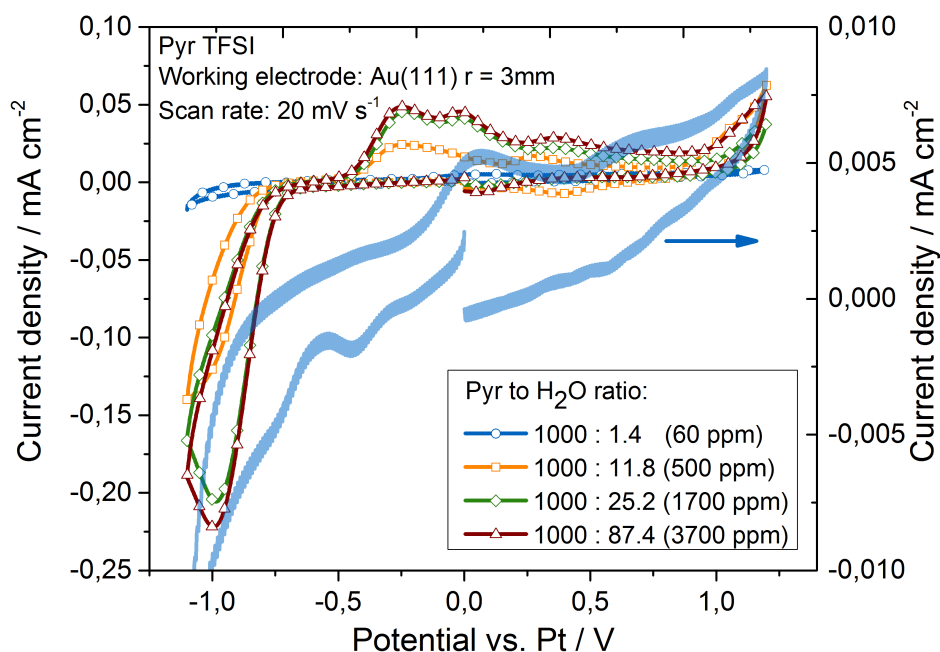


**Fig. 5.2:** CVs of BMP-TFSI with different amounts of water added. The thick blue curve was measured in dry BMP-TFSI and is plotted with a smaller current scale (Current density axis on the right side of the graph). This graph has been published in [113].

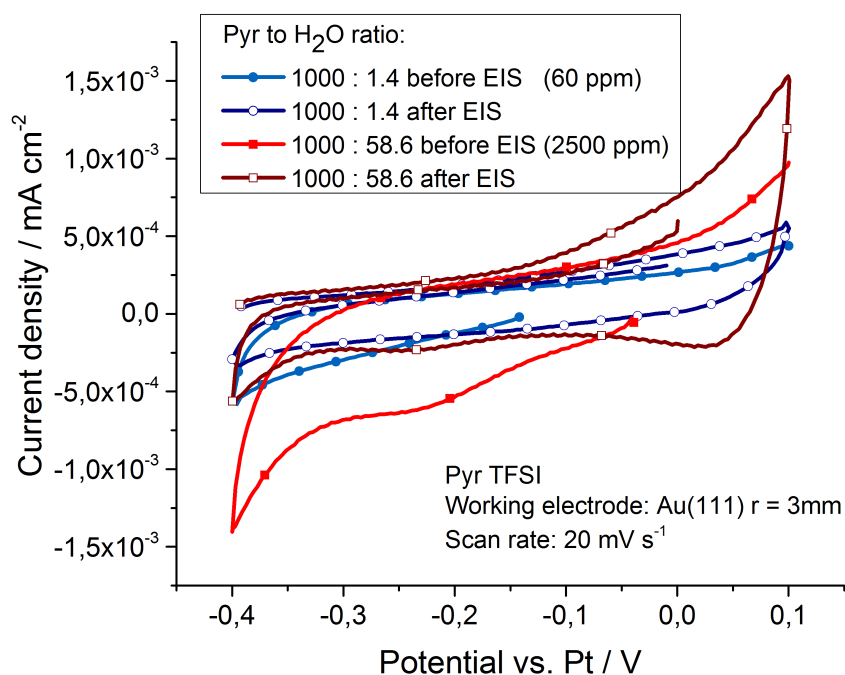


**Fig. 5.3:** CVs (20 mV/s) of BMP-TFSI recorded immediately before and after the EIS measurements and in the same potential region. The blue curves were measured in dry BMP-TFSI (1000 : 1.4), the red curves with added water (1000 : 58.6). This graph has been published in [113].

Since the CVs in dry BMP-TFSI (1000 : 1.4) before (light blue) and after (dark blue) the EIS measurement are very similar, it can be concluded the system does not undergo any significant changes during the impedance spectroscopy. Neither are any faradaic processes observed in any CV. In the more humid IL (1000 : 58.6) on the other hand, differences between the CVs recorded before (light red) and after (dark red) EIS are much more pronounced. It can be assumed that the higher currents in the CV after EIS are caused by products that were formed during the EIS measurement [134]. The current density is still rather low, as can be seen when compared to the 0.5 mM ferrocene peak in Fig. 5.1. Therefore, the effect is not expected to influence the results significantly.

### 5.2.3 Electrochemical Impedance Spectroscopy

Immediately after the initial CV was recorded, the EIS measurement was started in the same potential range. Each EIS data set consists of 51 data points, the first one recorded at +0.1 V vs. Pt. The potential was then subsequently decreased in steps of 20 mV until the final potential of -0.4 V vs. Pt was reached. For each data point, an EIS spectrum was measured in a frequency range between 200 kHz and 0.5 mHz with a 10 mV amplitude. After each potential step and before the next data point was measured, a two-minute waiting period was applied to allow the system to revert to an equilibrium state. After the last EIS measurement, the second CV was recorded with the same potential limits, but starting at the present cell potential of -0.4 V.

The double layer capacitance can be calculated from the measured impedance data by fitting it to an equivalent circuit that correctly describes all processes in the electrochemical cell. Because finding the best equivalent circuit is not a straightforward task, three possible candidates were chosen and the resulting fits compared for their quality (Fig. 5.4).

- **Orange:** An ohmic resistor  $R_{Ohm}$  and a capacitor  $C_{HF}$  in series, using a limited frequency range between 200 kHz and 100 Hz (Fig. 5.4(a));
- **Green:** An ohmic resistor  $R_{Ohm}$  and a CPE  $Q$ , using the whole recorded frequency range (Fig. 5.4 (b));
- **Blue:** An ohmic resistor  $R_{Ohm}$  in series with a parallel combination of a capacitor  $C_{HF}$  and a CPE  $Q$ , using the whole frequency range [112] (Fig. 5.4 (c)).

To determine the double layer capacitance from an equivalent circuit that contains a constant phase element, an effective capacitance  $C_{Surface}$  must be calculated with a method developed by Hirschorn et al. [135], using an infinite charge transfer resistance.

Fig. 5.5 (a) shows a typical Bode plot of the Au(111) surface in BMP-TFSI with a water content of 1000 : 58.6 with fits from all three equivalent circuits in the respective colors. Fig. 5.5 (b) shows the resulting potential dependence of the calculated double layer capacitances. For equivalent circuit (c) the sum of  $C_{HF}$  and  $C_{Surface}$  is plotted.

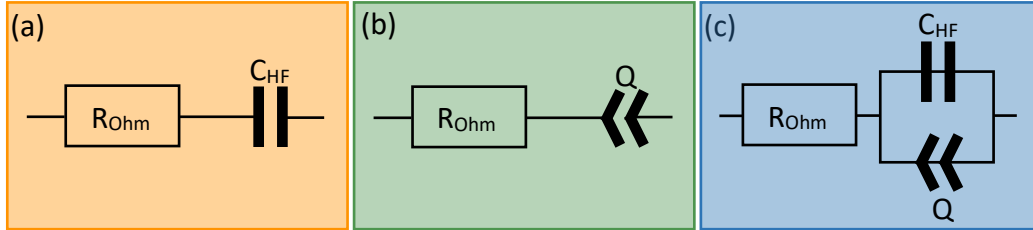


**Fig. 5.4:** Illustration of the three equivalent circuits that were tested for the fit of the EIS spectra. This graph has been adapted from [113].

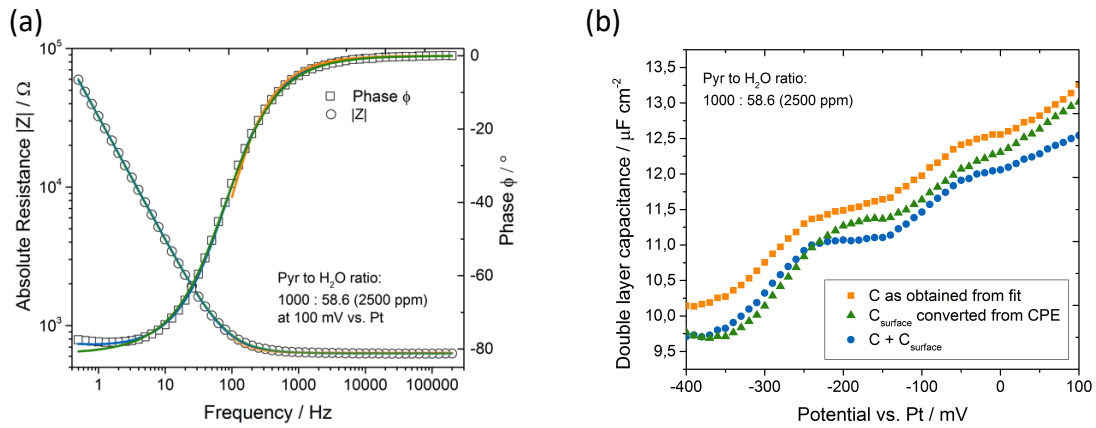


**Fig. 5.5:** (a) Typical Bode plot of BMP-TFSI (1000 : 58.6) at 0.1 V vs. Pt fitted with the three options for the equivalent circuit. (b) Resulting fitted double layer capacitance vs. potential curves from all three equivalent circuits. This graph has been published in [113].

In general, the double layer capacitance vs. potential curves show a very similar behavior of an increasing capacitance with higher potential and two small ‘humps’ around -250 mV and -50 mV. To determine the most suitable equivalent circuit, the quality of each fit was estimated using the  $\chi^2$  test:

$$\chi^2 = \sum_{i=1}^n \frac{|Z_{meas}(i) - Z_{model}(f, param)|^2}{\sigma_i^2} \quad (5.1)$$

Here,  $\sigma_i$  is the standard deviation,  $Z_{meas}(i)$  the measured impedance at frequency  $f_i$  and  $Z_{model}(f, param)$  the impedance calculated from the respective model used, a function of the model that depends on the models parameters  $param$  ( $R_{Ohm}$ ,  $C$ ,  $CPE$ ). The calculated  $\chi^2$  values for all 51 spectra using each equivalent circuit are:  $\chi^2_a = 0.011$ ,  $\chi^2_b = 0.040$  and

$\chi^2_c = 0.012$ . Therefore, equivalent circuit (a) was selected for the evaluation of the EIS data. However, the treatment of the data and thus the results would be almost the same if the sum of  $C_{HF}$  and  $C_{surface}$  from circuit (c) were used instead. Fig. 5.6 shows the capacitance vs. potential curves fitted from measured data for five different IL : water ratios. In Fig. 5.6 (a), the fitted  $C_{HF}$  vs. potential curves are plotted as obtained from the experimental data. Each sample exhibits the same general behavior of a capacitance that increases with potential and a single peak in the lower half of the examined potential range. The second peak, which was clearly visible in Fig. 5.5, only appears in some of the data sets. As mentioned above, the potential of the reference electrode, while stable throughout a single measurement, shifted between measurements, causing the maxima to be located at different potentials in each curve.

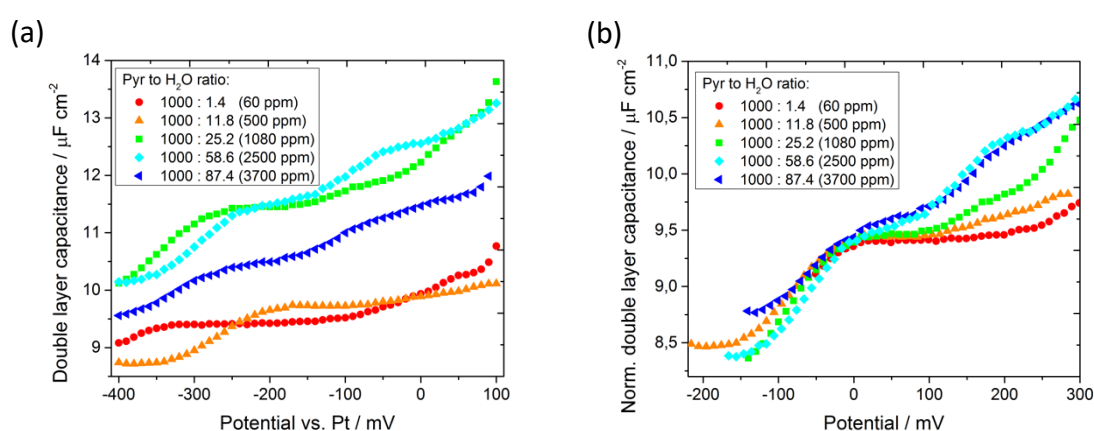


**Fig. 5.6:** (a) Double layer capacitance vs. potential curves of Au(111) in BMP-TFSI measured at different water contents. (b) The same data, shifted and normalized. This graph has been published in [113].

Another issue are the capacitance differences in capacitance between the various water contents. This inconsistency can be possibly attributed to changes in surface roughness of the Au(111) single crystal, a result of annealing the Au(111) single crystal after each measurement. To allow a comparison between the data, each curve's potential was therefore shifted to bring the maximum of the first peak to 0 mV. Also, the capacitance of each sample was normalized to the value of the first peak of the driest curve at  $C_{HF} = 9.42 \mu F$  to compensate for the shifting reference electrode potential. While the potential region below the first peak is not affected much by the addition of water, the curves show significant differences at higher potentials. The double layer capacitance of the dry sample (red curve) stays constant after the first maximum for a potential range of ca. 250 mV before it starts rising again. With increasing water content, this onset appears at lower potentials and with a larger gradient, resulting in higher overall capacitance values throughout the curve.

The PZC of Au(111) in BMP-TFSI can be estimated by comparing the literature values for the PZC of similar systems. The position of the PZC in *1-Butyl-1-Methyl-Pyrrolidinium Bis(Trifluoromethylsulfonyl)amide* has been reported in a range between -0.5 V and -0.1 V vs. Pt. at an Au(111) electrode [130] and for *1-Butyl-3-Methyl-Imidazolium Hexafluorophosphate* between -0.4 V and -0.2 V vs. Pt [112], [136]. It can therefore be assumed that the first peak, which was shifted to 0 mV, lies within  $\pm 100$  mV of the PZC.

### 5.3 Scanning Tunneling Microscopy

It has previously been reported for both Au(100) [40] and Au(111) [133], [137] surfaces that features in the double layer capacitance vs. potential curves are sometimes caused by a potential induced surface reconstruction taking place on the single crystal surface. To verify that the peak in the measured capacitance curves is not merely caused by this effect but represents the behavior of  $C_{DL}$ , the Au(111) surface in BMP-TFSI was also examined with EC-STM, which would detect changes in the surface structure. The potential range for the experiment was chosen larger than in the EIS measurements to ascertain that a shift in reference electrode potential would not cause the relevant potential region to be outside of the observed window.

The series of EC-STM images was recorded in dry BMP-TFSI (1000 : 1.4) immediately after the IL was removed from the glove box (Fig. 5.7). After a suitable area on the gold surface was located that showed both a large atomically flat terrace and a region of monoatomic steps, images of the gold surface were recorded at different potentials. After each image, the potential was shifted by 200 mV, starting at 0 mV, decreasing down to -800 mV, increasing to +400 mV and a finally returning back to 0 mV (all vs. Pt). Before an image was recorded, one full scan of the sample was performed under the same conditions without recording the result. This allows the system to reach an equilibrium state after the potential change and the tip position can be adjusted manually to compensate for drift. Adjusting the center of the image manually after several scans is necessary in most longer measurements to keep a sufficiently large portion of the starting image visible in each micrograph. Because of this process, all displayed images were scanned from top to bottom and around 10 minutes passed between the start of consecutive measurements.

The only major changes in the image series take place around the first step that separates the large terrace from the stepped region. The edge is rather curvy in the first images but becomes straighter at lower potentials. When the potential is increased again, the shape of the edge remains stable until the large hole on the terrace extends towards the edge until it opens up, forming a new curve in the edge. On the other hand, several small holes are visible on the terrace that slowly disappear when the potential is decreased and reappear when the potential is increased again.

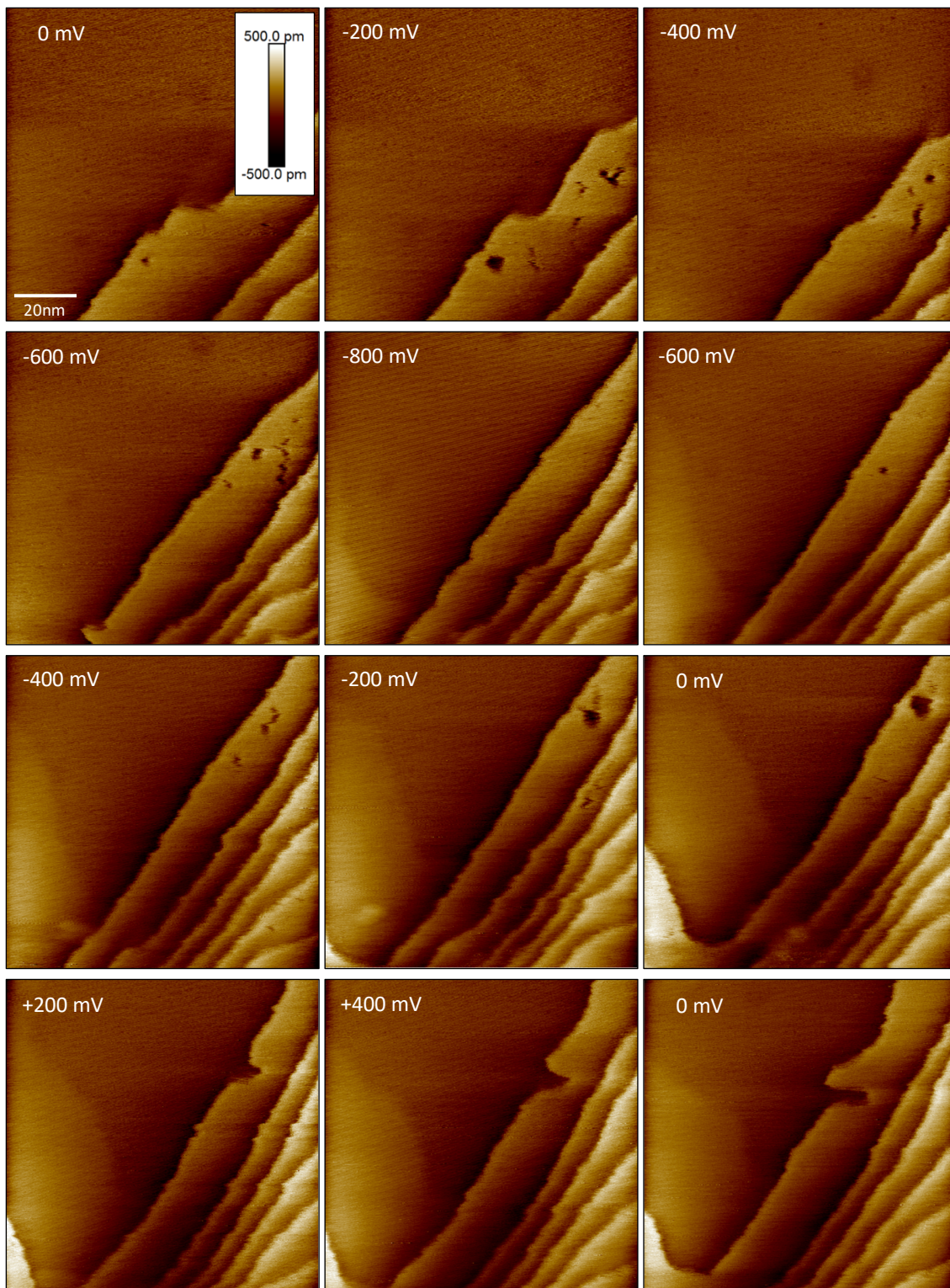


**Fig. 5.7:** EC-STM image series (100 nm x 100 nm) of an Au(111) surface in dry BMP-TFSI (water content 1000 : 1.4) at different potentials. All potentials were measured against a Pt wire reference electrode. (Microscope parameters:  $I_T = 1$  nA,  $U_{Bias} = 100$  mV). Parts of this graph have been published in [103].

At -200 mV, these holes merge into the single large hole that drifts into the step edge. The restructuring processes of Au (111) surfaces are a known effect caused by the high

mobility of the gold atoms on the surface which is enhanced by the influence of the STM tip's electric field [138], [139]. A closer look at the large flat area reveals the previously described faint pattern of diagonal, parallel lines from picking up the 50 Hz frequency of the local power network. Besides these, no other significant changes were observed, especially no dependence on the potential of surface structures in the most interesting potential range between -400 mV and +100 mV that could have had an effect on the double layer capacitance curves from the EIS measurements [140]. In a similar experiment with a slightly different ionic liquid, a surface reconstruction into the herringbone structure was observed at -1.2 V vs. Pt [141], far outside of the potential range relevant for this study. Therefore, it can be concluded that the peaks in the double layer capacitance vs. potential curves are not the result of a surface reconstruction.

## 5.4 Mean Field Theory

Detailed studies about the effects of small amounts of water on the double layer of ionic liquids in general and the double layer capacitance in particular have not been published before. Because of these unknown influences, an accurate interpretation of measurements in the EDL of ionic liquids is still difficult. However, the general trends observed here can be well explained under the assumption that the adsorption of water into the double layer is stronger when positive potentials are applied to the electrode than at negative potentials. To test the plausibility of the interpretation of the experimental results, they were compared to calculated values using a simple mean-field theory [24], [142]. This section is a contribution by A. Kornyshev. The full details and calculations can be found in our publication [113] and supporting information [103].

The mean-field theory that describes the capacitance curves in ionic liquids [24] needs to be modified to incorporate the influences of the adsorption of water into the EDL because of potential differences, a process known as electrosorption, using several physical approximations:

- At potentials near the PZC ( $-k_B T/e < u < 0.5 k_B T/e$ ), a region of water depletion is assumed in which no electrosorption takes place.
- At potentials outside the depletion range, water molecules are adsorbed into the EDL until their density is more than twice as high as in the bulk liquid. The electrosorption becomes stronger at potentials further away from the PZC and this increase is much steeper on the positive side than on the negative.

- The distribution of water in the EDL is assumed to be homogeneous, the discretely layered structures that have been reported elsewhere are not considered here. This affects the effective permittivity for the dielectric screening of ion-ion interactions and thereby the double layer capacitance which increases when more water is adsorbed in the double layer.
- The asymmetry of the positive and negative sides of the capacitance curves was implemented into the model by assigning a four times higher maximum density to the anions than to the cations. For the positive potential range the compacity parameter, which indicates how much the ionic liquid can be compressed, was estimated as  $\gamma = 0.4$ . The value originates from the ratio of the average ion concentration in the bulk IL to the highest possible cation concentration.
- The possible effect of dielectric saturation of the water molecules, where all molecules are fully aligned and their orientation frozen in the strong electric field near the surface, has been ignored here because the effect is not understood well enough to make reliable predictions. If implemented, it would reduce the influence of water on the double layer capacitance and the impact would grow with increasing electrode polarizations.

Using the potential dependent ratio of water molecules to the number of ions in the double layer  $X(u)$ , the model was used to calculate the capacitance vs. potential curves in Fig. 5.8. In order to establish this simple mean-field model, several compromises had to be made. The resulting curves with different water contents all show the expected behavior. However, the effect of the humidity of the ionic liquid on  $X_0$ ,  $X^-$  and  $X^+$  needs to be approximated since the absorption isotherm, which specifies the influence of the water concentration in the bulk IL on the average water content in the EDL, is unknown. The results indicate that these approximations are sufficiently accurate. On the other hand, the mean-field does not incorporate overscreening, which becomes particularly important at small electrode polarizations and has been taken into account in the more advanced model shown in [26]. Another shortcoming of the model is the exclusion of short ranged correlations. They were considered in the system's free energy in the original model in all terms except the first ([24], Eq. 1) but were set to zero for simplicity in the deduction of the analytical solution. If these terms were considered as well, the decoupling of cation-anion pairs and the accumulation of ions of only one type would be hindered. In consequence,  $C_0$  and  $U$  would have to be re-normalized under the new conditions, resulting in a stretched potential axis. With around  $50 \mu\text{F}/\text{cm}^2$ , the calculated values of  $C_0$  are generally too high and would be reduced if the correlation terms were considered. The curves shown in Fig. 5.8 have been corrected with a reduction of  $C_0$ .

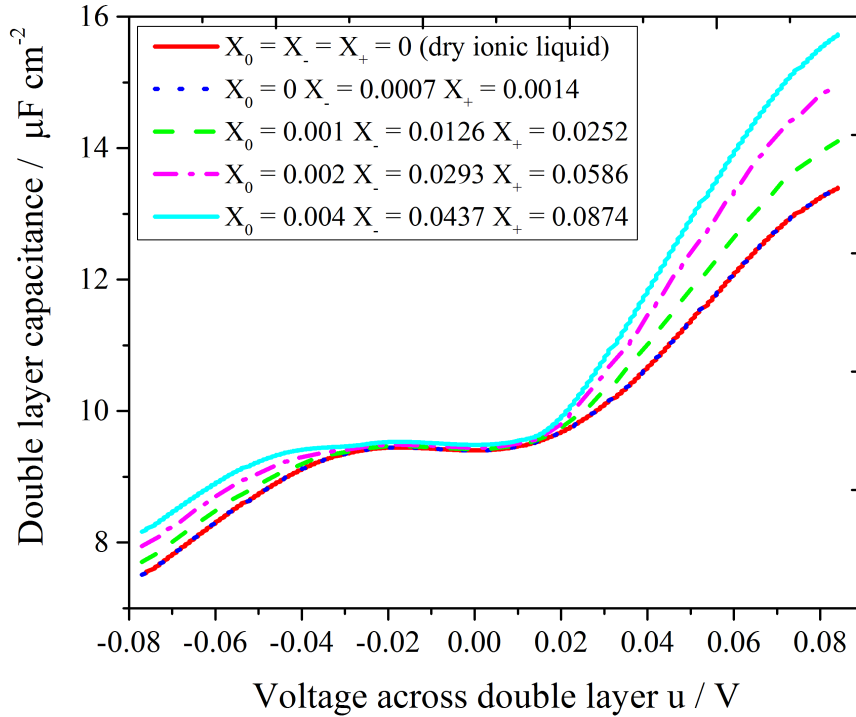


**Fig. 5.8:** Calculated capacitance curves from the mean-field model.  $X_0$  describes the water content in the depletion,  $X_-$  and  $X_+$  are the portions of water content in the positive and negative potential regions where saturation takes place. The red solid curve represents a completely dry ionic liquid. This graph is a contribution from A. Kornyshev and has been published in [113].

## 5.5 Interpretation

A comparison of the results from the EIS measurements (Fig. 5.6 (b)) and the calculated curves from the mean-field model (Fig. 5.8) helps to improve the understanding of the data. The theoretical and experimental capacitance curves are in general very similar to each other, the capacitance increases when the potential becomes more positive and the shape and size of the peak is consistent throughout the data sets. Both studies show that the double layer capacitance increases with the amount of water added to the ionic liquid and therefore the amount of water adsorbed in the EDL. Also, water adsorption at the surface becomes stronger with increasing electrode polarization, an effect that is notably stronger in the positive potential wing of the curves. In the mean-field theory this behavior was achieved by attributing a lower compacity value to the anions than to the cations, which also confirms the prediction made in ref. [126]. On the other hand, there are also certain differences between the experimental and theoretical capacitance curves:

- The second maximum in the theoretical curves assumes a bell shape and the curve approaching it therefore follows a concave course near the peak. The

experimental curves on the other hand appear convex instead and bend upwards towards the peak.

- The value of the absolute double layer capacitance changes much faster in the calculated than in the experimental curves and the potential range is smaller in the curves from the mean-field model. As mentioned above, this is caused by neglecting the short-range correlations between the ions. The resulting stretched potential axis if the correlations were incorporated into the model would cause a smaller variation of the capacitance in return. A rescaled representation of the calculated curves that takes the short-range correlations into account is presented in Fig. 5.9.

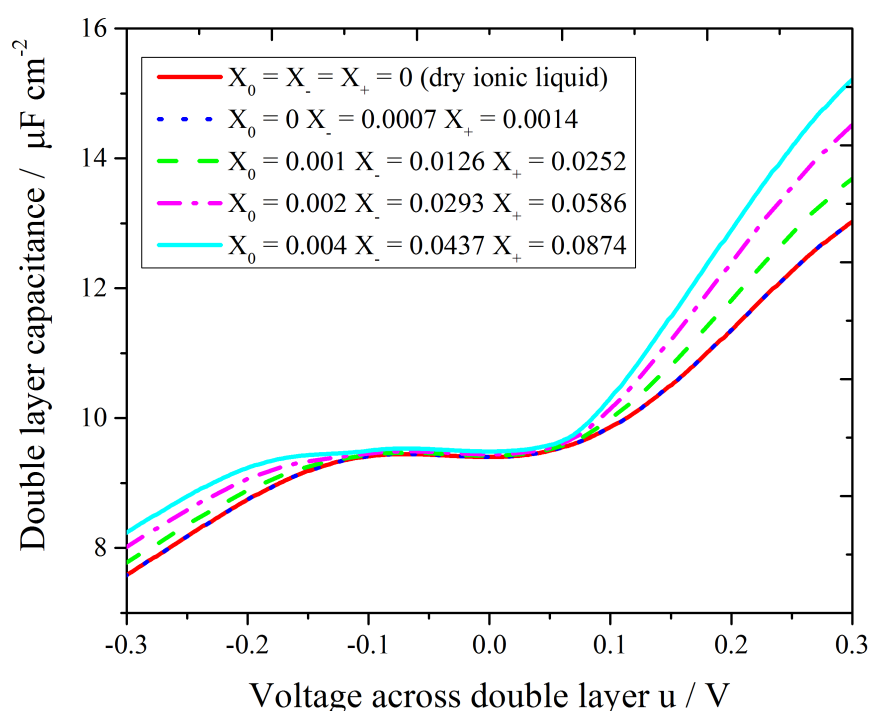


**Fig. 5.9:** Calculated capacitance curves with rescaled voltage dependence.  $U$  has been replaced by  $4 U_{\tau}$  and the following parameters have been used to calculate the curves:  $\bar{c}/c_{max}^+ = 0.4$ ,  $\bar{c}/c_{max}^- = 0.1$ . This graph is a contribution from A. Kornyshev and has been published in [103].

The mean-field model is only a simple starting point for the description of the influence of water on the double layer capacitance. Many parameters had to be approximated and simplifications had to be made. A realistic model could be created by computer simulations or *Density Functional Theory* (DFT) calculations, using a calculated isotherm for the potential dependent absorption and adsorption of water. However, the model achieves the goal to reproduce and explain the experimental results to a certain point.

In the ongoing theoretical research for a conclusive description of the EDL, Budkov, Kolesnikov and Kiselev recently developed an improved model [127] (BKK model) that incorporates a polarizable co-solvent, electrostatic interactions between ions and solvent, and, extending on the model used for the calculations shown here [24], the co-solvent molecules and their excluded volume. In a self-consistent density functional formalism, a modified Poisson-Boltzmann equation was developed and used to predict the distribution of co-solvent molecules and its influence on the double layer capacitance. According to the BKK model, a depletion of the co-solvent occurs near the electrode surface if its polarizability is lower than the IL's. Instead, the opposite is the case - an adsorption layer forms if the co-solvents polarizability is higher. The adsorption increases with the surface potential until a saturation of water is reached. However, a depletion of the co-solvent concentration relative to the bulk concentration does not occur. Regardless of this difference, the general shape of the capacitance vs. potential curves from the BKK model ([127], Fig. 4 (b)) is quite similar to the experimental curves presented here. That their model still agrees so remarkably with the experimental curves can be attributed to its sensitivity to the strong effect of dielectric screening, which increases with the amount of adsorbed polarizable co-solvent molecules. A remaining untreated issue in their theory is the possibility of the previously mentioned freezing of the orientation of the polarized co-solvent molecules in the strong electric field near the electrode surface. Gongadze and Iglič [128] have developed a mean-field model (GI model) that incorporates the saturation of the orientational ordering of water molecules near the surface and its influence on the relative permittivity. However, it was not the focus of their work and was therefore not investigated in greater detail. Also, the influence on the double layer capacitance was not examined. For future work, a combination of the GI and the BKK model would yield more accurate results than any existing model.



## 6 Polyoxometalate Adsorption on HOPG

The adsorption of POMs is known to be able to improve certain properties of electrodes. For instance, the POM  $\text{H}_3\text{PMo}_{12}\text{O}_{40}$ , adsorbed on activated carbon as a hybrid electrode for supercapacitors, was shown to increase the cell capacitance compared to the pure carbon material, while retaining a good stability over many cycles [143]. Adsorption plays an important role in POM electrochemistry, either unwanted when dissolved POMs are required or intentional as in the previous example. However, many aspects of POM adsorption such as the influence of their charge and of the other ions in the electrolyte are not completely understood. Therefore, an in-depth analysis of several different factors that are known to influence the adsorption behavior. Although STM and SECPM have a better lateral resolution than AFM, AFM was chosen over imaging because the STM/SECPM tip was frequently found to scratch the adsorbed POMs off the imaged area which resulted in images of the uncovered HOPG surface in many measurements. EC-AFM in ScanAsyst mode, while not able to resolve the molecular lattice structure of an adsorbed POM monolayer, was found to be much less invasive and allowed to clearly identify adsorbed POM structures.

The effect of the initial manganese oxidation state in  $\text{Mn}^{\text{II}}_3\text{SiW}_9\text{O}_{34}$  and  $\text{Mn}^{\text{III}}_3\text{SiW}_9\text{O}_{34}$  and of changes in the oxidation state of  $\text{Mn}^{\text{II}}_3\text{SiW}_9$  are studied using a combination of *Cyclic Voltammetry* (CV) and ex-situ AFM. In a following experiment, the potential dependence of  $\text{SiV}_3\text{W}_9\text{O}_{40}$  adsorption on HOPG was measured by recording an image series with *Electrochemical AFM* (EC-AFM). In the second half of the chapter, the influence of different anions and cations in the electrolyte on the adsorption behavior will be analyzed, as well as the differences between several differently charged POMs. In contrast to previous microscope studies that focus on the molecular lattice structure of the adsorbed POM monolayer, the shape and distribution of the larger POM agglomerates will be in the focus of this investigation.

### 6.1 POM Interactions

Polyoxometalates are known to easily adsorb on many electrode surfaces. This effect can be useful for the design of electrochemical sensors [80] and for electrocatalysis, where the immobilization of POMs can help to increase their catalytic activity [144]. Through adsorption, and therefore the conversion of homogeneous into heterogeneous processes, the reactivity and selectivity of POMs can be enhanced [145]–[147]. First high-

resolution SPM images of POMs were published in the early 90s by Keita et al. for which they used STM and AFM to image the surface of POM single crystals [148], [149] and of thin POM layers, adsorbed on HOPG surfaces and deposited by drying a drop of methanolic POM solution on the substrate [149], [150]. The adsorbed POMs arranged in an ordered two-dimensional layer, forming a triangular lattice that resembles in shape the HOPG surface but with intermolecular distances that agree well with the size of the POM molecules. Barteau et al. confirmed these findings in similar experiments with several different POMs [151]. In the I-V curves of simultaneous tunneling spectroscopy measurements on the same samples, they observed a *negative differential resistance* (NDR) that was attributed to a resonant tunneling effect caused by the isolation of the POMs in a double barrier. They also recorded tunneling spectra at two different sites on the adsorbed lattice - the position of an adsorbed POM (Site A) and over a hole between POMs (Site B). The shape of the tunneling spectrum at site B closely resembles the shape of a spectrum recorded on a freshly cleaved HOPG surface (Fig. 6.1).

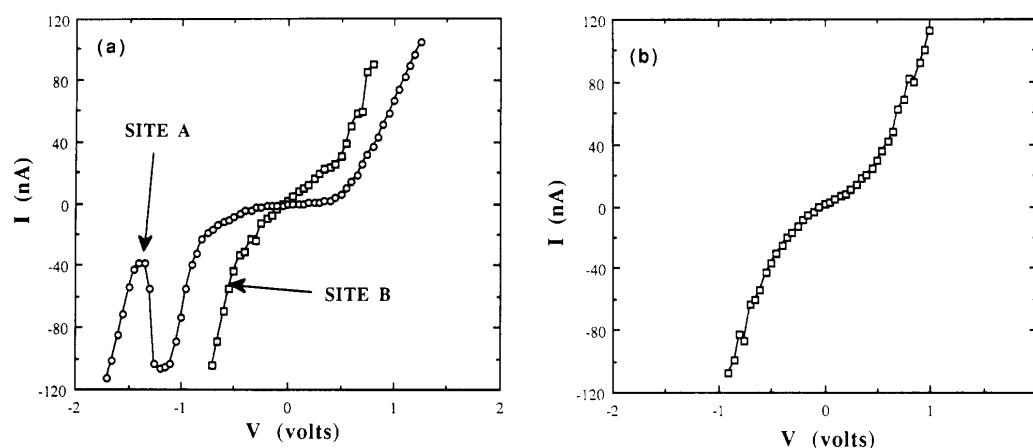


**Fig. 6.1:** (a) Tunneling spectra of  $(\text{NH}_4)_6\text{V}_{10}\text{O}_{28} \cdot 6\text{H}_2\text{O}$ , adsorbed on HOPG. The site A-curve was recorded on top of an adsorbed POM and exhibits the characteristic NDR peak. The site B-curve was recorded over the hole between adsorbed POMs and closely resembles the spectrum measured over a pristine HOPG surface in (b). The images were adapted from [151].

This led to the conclusion that the POMs adsorb in the form of a monolayer since tunneling spectra at site B of a multilayer of POMs would measure underlying POMs and thus still display the NDR peak. Both NDR and ordered POM monolayers have since been repeatedly observed by their group on many different samples [152]–[157]. In-situ STM measurements with simultaneous potential cycling by different groups revealed the electrodeposition of similar monolayer structures when the potential was cycled to strong negative values [158]–[160]. Choi et al. used cyclic voltammetry measurements to compare the adsorption and catalytic activities of four similar Keggin POMs ( $\text{SiW}_{12}\text{O}_{40}$ ,  $\text{SiMo}_{12}\text{O}_{40}$ ,  $\text{PW}_{12}\text{O}_{40}$ ,  $\text{PMo}_{12}\text{O}_{40}$ ,) on HOPG and *glassy carbon* (GC) and found that the molybdate POMs interact much stronger with each surface than the tungstate POMs [161]. In 2006, Alam et al. reported the first sub-molecular resolution images of POMs

with STM and *current-imaging tunneling spectroscopy* (CITS), a technique that combines STM imaging with the recording of a tunneling spectrum at each data point. In measurements of the large, wheel shaped  $\text{Cu}_{28}\text{P}_8\text{W}_{48}$ , they were able to resolve the positions of individual Cu atoms within the molecule, and confirmed the results by comparing the images to X-ray crystallography data [162].

The properties of POMs are known to be affected by the solvent they are dispersed in [163]–[167]. Also, their charge influences the interactions with surfaces, the solvent and other POMs [168]. Therefore, to explain the adsorption behavior, it is important to also understand their aggregation in solution. Alain Chaumont and Georges Wipff have extensively studied different aspects of POM interactions using MD simulations. They examined the influence of different counterions on  $\text{PW}_{12}$  ( $\text{Cs}^+$ ,  $\text{NBU}_4^+$ ,  $\text{UO}_2^{2+}$ ,  $\text{Eu}^{3+}$ ,  $\text{H}_3\text{O}^+$  and  $\text{H}_5\text{O}_2^+$ ) dissolved in water and methanol [169]. Despite their negative charge and expected repulsive electrostatic forces, the POMs were found to aggregate to form dimers and longer chains. Their numbers increase with higher POM concentration and counterion charge. This effect only occurred in aqueous solution and water molecules were found to play a crucial role in the assembly by forming bridges between two  $\text{PW}_{12}$  molecules. Counterions played no direct role and only stabilize the connection via long-range electrostatic interactions. Since ionic aggregation in water often causes an increased surface activity, they also analyzed the behavior of the same POM-counterion combinations at aqueous interfaces with HOPG, different ionic liquids and organic solvents [170]. They observed a strong interaction between the POM and an uncharged HOPG surface with 60 % of the  $\text{PW}_{12}$  molecules accumulating at the interface in the presence of  $\text{H}_3\text{O}^+$  counterions. The POMs do not distribute uniformly at the interface but often aggregate there as well. In another study, they examined the interactions between Keggin POMs dissolved in water and depending on their charge, using the isostructural  $\text{PW}_{12}^{3-}$ ,  $\text{SiW}_{12}^{4-}$  and  $\text{AlW}_{12}^{5-}$  [171]. While the number of dimers and larger oligomers decreased from  $\text{PW}_{12}$  to  $\text{SiW}_{12}$  as expected due to the stronger electrostatic repulsion, the most negative  $\text{AlW}_{12}$  was found to aggregate even more than  $\text{PW}_{12}$ . In this case, a different mechanism is mainly responsible for the POM-POM interactions. Instead of  $\text{H}_2\text{O}$  bridging, the  $\text{AlW}_{12}$  molecules are mainly attached to each other through bridging  $\text{H}_3\text{O}^+$  counterions. Comparing the influence of different counterions, they found that  $\text{Li}^+$  has a similar effect to  $\text{H}_3\text{O}^+$ , but  $\text{Na}^+$  and  $\text{Cs}^+$  do not stabilize  $\text{AlW}_{12}$  dimers due to different specific POM-counterion interactions. Comparing the condensation of all three POMs at the interface with graphite, the results were less conclusive. On average,  $\text{PW}_{12}$  showed a stronger affinity for the graphite surface (6.2 anions at the interface) than both other POMs (3.0 anions each). However,  $\text{AlW}_{12}$  produced the single most populated interface (7 anions) and was found to still form dimers bridged by  $\text{H}_3\text{O}^+$  at the surface. Bera et al. analyzed the same POMs in acidic solution (0.1 M HCl, pH = 1) with MD simulations and experimentally with *Small-Angle X-ray Scattering* (SAXS) [172]. In contrast to the results from Chaumont and Wipff, only  $\text{PW}_{12}$  formed close-contact aggregates while the higher

charged  $\text{SiW}_{12}$  and  $\text{AlW}_{12}$  only interact through non-contact long-range associations due to stronger electrostatic forces. They attributed the difference to Chaumont's and Wipff's observations to the changed pH of the solution [173] and the inclusion of other types of protons (Zundel,  $\text{H}_5\text{O}_2^+$ , Eigen,  $\text{H}_9\text{O}_4^+$ , ions) into their simulations. A control simulation without HCl indicated that the aggregation behavior is influenced by the pH of the system. From the changes of the SAXS correlation peaks with the variation of concentration and temperature, they concluded that  $\text{PW}_{12}$  exists as mixture of non-associated monomers and randomly percolated monomers at higher concentrations and only as non-associated monomers at lower concentrations (Fig. 6.2). The formation of the percolated monomers was attributed to short-range  $\text{PW}_{12}\text{-H}_2\text{O}$  and  $\text{PW}_{12}\text{-H}_3\text{O}^+$  correlations. On the other hand,  $\text{PW}_{12}\text{-Cl}^-$  correlations played no role. At low concentrations, the separation between the POMs is determined by their Debye length which is controlled by the distribution of the smaller protons and chloride ions. The higher charged  $\text{SiW}_{12}$  and  $\text{AlW}_{12}$  were only present as non-associated monomers in all simulations and measurements. Clusters and percolated clusters were not observed for any POM.

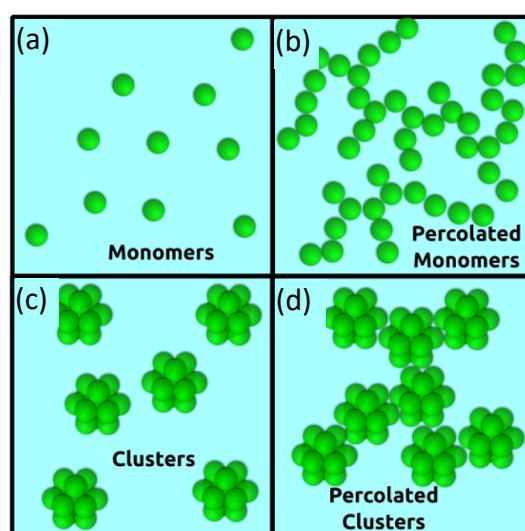


**Fig. 6.2:** Possible correlation states of POMs in solution. (a) Dissociated monomers, (b) randomly percolated monomers, (c) clusters of contacting monomers, and (d) randomly percolated clusters of contacting monomers. The image was adapted from [172].

Serapian and Bo used MD simulations to compare the aggregation behavior of the plenary  $\text{AlW}_{12}^{5-}$  to its monolacunary variation  $\text{AlW}_{11}^{9-}$  and, to analyze the influence of the dipole moment introduced by the lacuna, to the fictitious  $\text{AlW}_{12}^{9-}$  with  $\text{Li}^+$  counterions in aqueous solution [174]. The aggregation of  $\text{AlW}_{12}^{5-}$  was minimal but  $\text{AlW}_{11}^{9-}$  formed stable aggregates. Analysis of the dipole moment's orientation and comparison with the equally charged but symmetrical  $\text{AlW}_{12}^{9-}$  showed that the increased aggregation is not by the dipole moment of the lacunary POM but by the higher negative charge. In agreement with Chaumont and Wipff, they found the increased charge attract counterions that act as an "electrostatic glue". Even as single monomers,  $\text{AlW}_{11}^{9-}$  is surrounded by a much larger

number of  $\text{Li}^+$  than  $\text{AlW}_{12}^{5-}$  which they believe improves the probability of aggregate formation.

It has been shown that STM and AFM are more capable in detecting very small amounts of adsorption than electrochemical methods [158] but most previous studies have been performed on POMs adsorbed by evaporation of a small amount of solution on the substrate. Therefore, the influence of the electrode potential on the adsorption behavior of POMs has only been addressed in few studies, all performed during continuous potential cycling. In the first half of this chapter, the potential dependent adsorption behavior of POMs with in-situ and ex-situ AFM imaging will be investigated in terms of reversibility and the POM's oxidation state. The second half focusses on the different influences on POM aggregation and the sometimes-contradicting findings of previous studies about the role of the POM's charge. For the first time, the effect of different other anions in the solution will also be analyzed.

## 6.2 Potential Dependence of POM Adsorption

### 6.2.1 Comparison of $\text{Mn}^{\text{II}}_3\text{SiW}_9$ and $\text{Mn}^{\text{III}}_3\text{SiW}_9$

Comparing the electrochemical properties of the two tri-Mn substituted POMs  $\text{Mn}^{\text{II}}_3\text{SiW}_9$  and  $\text{Mn}^{\text{III}}_3\text{SiW}_9$ , which only differ in their initial oxidation states, differences in their adsorption behavior on a glassy carbon electrode were observed in their cyclic voltammograms. In this section, the mechanism behind the effect will be analyzed. The results presented here have been published in [7].

For the CVs, each POM was dissolved in a supporting electrolyte that contained a 0.5 mM concentration of the salts of the POMs,  $\text{Na}_{2.5}\text{K}_{4.5}[\text{Mn}^{\text{II}}_3(\text{OH})_3(\text{H}_2\text{O})_3(\alpha\text{-SiW}_9\text{O}_{34})\cdot 15\text{H}_2\text{O}$  and  $\text{Na}_{2.5}\text{K}_{4.5}[\text{Mn}^{\text{III}}_3(\text{OH})_3(\text{H}_2\text{O})_3(\alpha\text{-SiW}_9\text{O}_{34})\cdot 10\text{H}_2\text{O}$ , with 0.5 M  $\text{Li}_2\text{SO}_4$  and 0.02 M sodium acetate buffer from  $\text{CH}_3\text{COOH}$  and  $\text{NaCH}_3\text{COO}$ . It then was pH adjusted using diluted  $\text{H}_2\text{SO}_4$ . As reference electrode, Mercury/Mercurous sulfate in saturated  $\text{K}_2\text{SO}_4$  (MSE, 0.640 V vs. NHE) was used and all potentials were converted to vs. NHE. The 1.6 mm diameter GC electrode was polished before the measurement in a two-step process. First with a 50 nm alumina-particle slurry, followed by a 7 nm silica-particle slurry. After each polishing, the electrode was thoroughly rinsed with de-ionized water. The electrochemical cell was purged with argon gas prior to the experiment for 20 minutes and blanketed with the same gas during the measurement, which was performed with a Bio-Logic SP-300 potentiostat. For the AFM measurements, the POM concentration was reduced to 50  $\mu\text{M}$  to decrease the surface coverage and the GC working electrode was replaced with HOPG, prepared as described in section 3.3.3. Each AFM image was

recorded on a freshly prepared HOPG sample, after the sample was removed from the electrochemical cell, rinsed with water and dried under ambient conditions.

### 6.2.2 Cyclic Voltammetry and AFM

CVs of both POMs in the potential region around the Mn redox reaction are shown in Fig. 6.3. The redox peaks of  $\text{Mn}^{\text{II}}/\text{Mn}^{\text{III}}$  and  $\text{Mn}^{\text{III}}/\text{Mn}^{\text{IV}}$  were identified by comparing the results to studies of  $\text{MnSiW}_{11}$  by Sadakane and Steckhan [175], [176].

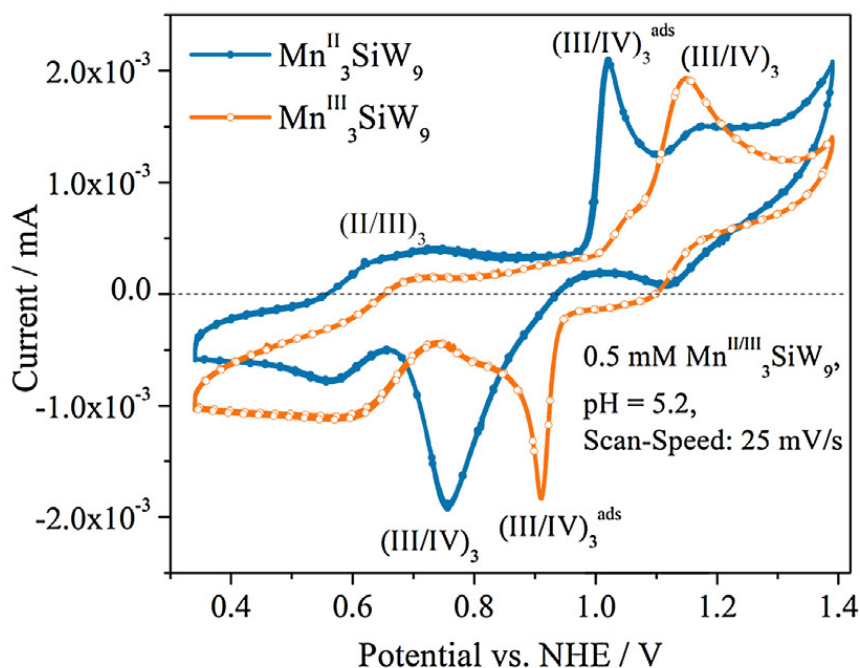


**Fig. 6.3:** CVs of 0.5 mM  $\text{Mn}^{\text{II}}_3\text{SiW}_9$  (blue) and  $\text{Mn}^{\text{III}}_3\text{SiW}_9$  (orange) in supporting electrolyte (pH 5) in the potential region of the Mn redox reaction. This graph has been published in [7].

The main difference between the two CVs is a single peak in each curve that displays the typical shape of adsorbed species, marked by  $(\text{III/IV})_3^{\text{ads}}$ , accompanied by a second peak that appears diffusion controlled and was therefore linked to solvated POMs. For  $\text{Mn}^{\text{II}}_3\text{SiW}_9$ , the peak from adsorbed species is an anodic wave at 1.02 V vs. NHE and for  $\text{Mn}^{\text{III}}_3\text{SiW}_9$  a cathodic wave at 0.91 V vs. NHE. The presence of the two peaks indicates a partial adsorption of  $\text{Mn}^{\text{II}}_3\text{SiW}_9$ . To confirm this hypothesis, the adsorption with AFM in air on an HOPG electrode was imaged by scanning the sample before and after oxidation of the POM (Fig. 6.4). The resulting images show varying amounts of particles adsorbed on the HOPG surface. They are around 5 nm high and have even larger lateral dimensions. Therefore, it can be assumed that the structures are clusters of POMs, not single molecules. Fig. 6.4(b) was measured on an HOPG sample that was immersed into the POM solution at OCP (0.442 V vs. NHE) for 60 seconds, keeping the POMs oxidation state at  $\text{Mn}^{\text{II}}$ . Here, the HOPG step edges are partially covered with the POM clusters while the

terraces are mostly free of adsorbates. After a potential sweep to the vertex potential of 1.29 V vs. NHE (c), the oxidation state is increased to Mn<sup>IV</sup> (c). A much larger number of clusters is adsorbed at the step edges and some can even be found on the terraces. The inset shows a magnification of a large group of POM clusters at a step edge. After a full potential cycle to the vertex potential and back to OCP (d), the oxidation state is returned to Mn<sup>II</sup>. The surface coverage is again much lower, similar to the initial image (b), which shows that the adsorption process indeed depends on the potential and is reversible. Even after several potential cycles within the same limits, no sign of permanent POM deposition was observed.

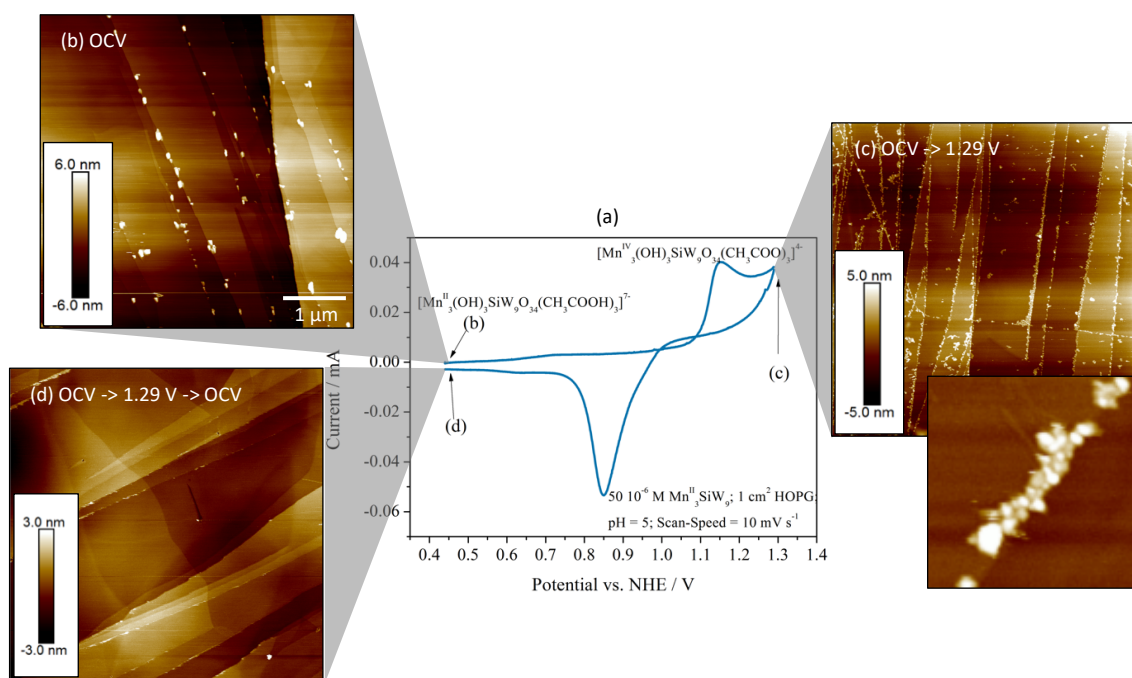


**Fig. 6.4:** (a) CV of a HOPG surface in a 50 μM Mn<sup>III</sup>SiW<sub>9</sub> solution in supporting electrolyte (pH 5). The POM's oxidation states are shown in the graph. (b,c,d) 5 μm x 5 μm AFM images (Scan Asyst mode) of the HOPG sample after removing it from the electrochemical cell. (b) AFM image after the HOPG was immersed in the POM solution at OCV (0.442 V vs. NHE) for 60 s. (c) AFM image after a linear potential sweep from OCV to 1.29 V vs. NHE at 10 mV/s. The inset shows a 400 nm x 400 nm area of the same sample with POM clusters adsorbed at a HOPG step-edge. (d) AFM image after a full CV from OCV to 1.29 V vs. NHE and back to OCV at 10 mV/s. This graph has been adapted from [7].

While most POMs adsorb irreversibly on different surfaces, reversible adsorption has been reported in some cases [7], [177], [178] and molecular dynamics studies by Chaumont and Wipff predict reversible POM interactions with hydrophobic surfaces such as graphite and ionic liquids [171]. In an adsorption study with different Keggin POMs, Choi et al. observed that the interaction of tungstate POMs with carbon surfaces is relatively weak while molybdate POMs adsorb much stronger [161]. To explain the observed differences in the Mn<sup>III</sup>/Mn<sup>IV</sup> oxidation peaks of both POMs and the reversible

adsorption imaged in AFM, it is proposed that  $\text{Mn}^{\text{II}}_3\text{SiW}_9$  POM undergoes a ligand exchange. At oxidation state  $\text{Mn}^{\text{II}}$ ,  $\text{Mn}^{\text{II}}_3\text{SiW}_9$  exchanges its terminal water for  $\text{CH}_3\text{COOH}$  while for  $\text{Mn}^{\text{III}}_3\text{SiW}_9$ , the  $\text{H}_2\text{O}$  ligand remains. A net-conversion from one POM species to the other is not possible in a three-electrode cell. Every electron available for reduction at the working electrode must enter the system through oxidation at the counter electrode and vice versa. In consequence, even when the right potential is applied, only the  $\text{Mn}^{\text{III}}_3\text{SiW}_9$  molecules within the Nernst diffusion layer near the working electrode can perform the exchange, which includes only an insignificantly small portion of all POMs. More detailed information and experimental evidence for the ligand exchange mechanism can be found in our publication [7].

In aqueous solution, hydrophobic materials tend to aggregate to decrease the exposure to water. Therefore, the surface activity of POMs at hydrophobic surfaces such as HOPG and GC increases when they become more hydrophobic. The Born energy of solvation can be used to determine the hydrophobicity of the POM [171], [179]:

$$\Delta G_{\text{Born}} = \frac{z^2 e^2}{8\pi\epsilon_0 a} \left(1 - \frac{1}{\epsilon_r}\right) \quad (6.1)$$

It is proportional to the ratio  $z^2/a$ , where  $z$  is the POM's charge and  $a$  its radius. Therefore, it increases for  $\text{Mn}^{\text{II}}_3\text{SiW}_9$  after the ligand substitution due to the increased effective radius from the larger ligand, rendering the molecule more hydrophilic. In combination with the decreasing charge upon oxidation from -7 at oxidation state  $\text{Mn}^{\text{II}}$  to -4 at  $\text{Mn}^{\text{IV}}$ , the molecule becomes hydrophobic enough to allow adsorption on the investigated carbon surfaces. The smaller  $\text{Mn}^{\text{III}}_3\text{SiW}_9$  on the other hand does not adsorb, even in its oxidized state. This explains why the  $\text{Mn}^{\text{III}}/\text{Mn}^{\text{IV}}$  oxidation peak in the CVs in Fig. 6.3 has the typical shape of adsorbed species for  $\text{Mn}^{\text{II}}_3\text{SiW}_9$  and for solvated species for  $\text{Mn}^{\text{III}}_3\text{SiW}_9$ . The reduction peak of adsorbed species in the CV of  $\text{Mn}^{\text{III}}_3\text{SiW}_9$  has not been investigated yet.

### 6.2.3 In-situ Imaging of $\text{SiV}_3\text{W}_9$

To analyze the influence of the potential on POM adsorption in more detail, the HOPG surface was monitored in-situ with EC-AFM.  $\text{Mn}^{\text{II}}_3\text{SiW}_9$  was exchanged for the tri-vanadium substituted  $\text{SiV}_3\text{W}_9$ , which was found to be less susceptible to removal by the AFM tip in the in-situ measurements.

The POM salt  $\alpha\text{-K}_6\text{HSiV}_3\text{W}_9\text{O}_{40}$  ( $\text{SiV}_3\text{W}_9$ ) was dissolved in 0.1 M sulfuric acid with varying concentration. All potentials were recorded against a Pt-wire quasi-reference electrode (0.92 V vs. NHE) and then converted to vs. NHE. The CV in the external cell was recorded with a Bio-Logic SP-300 potentiostat, for all AFM measurements the microscope's potentiostat was used. As counter electrode, an Au-wire was used in the external cell and

a Pt-wire in the microscope cell. The HOPG samples were prepared as described in section 3.3.3.

### 6.2.4 Cyclic Voltammetry

Before starting the microscopy experiments, a cyclic voltammogram of the system was recorded in a conventional electrochemical cell with a higher  $\text{SiV}_3\text{W}_9$  concentration to achieve a better-quality CV that yields more detailed information about the redox reactions in the system (Fig. 6.5).

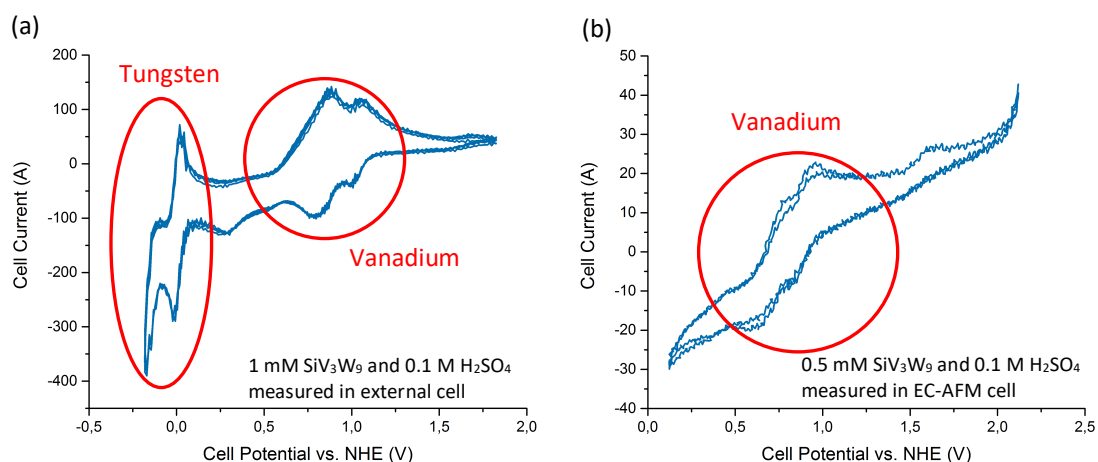


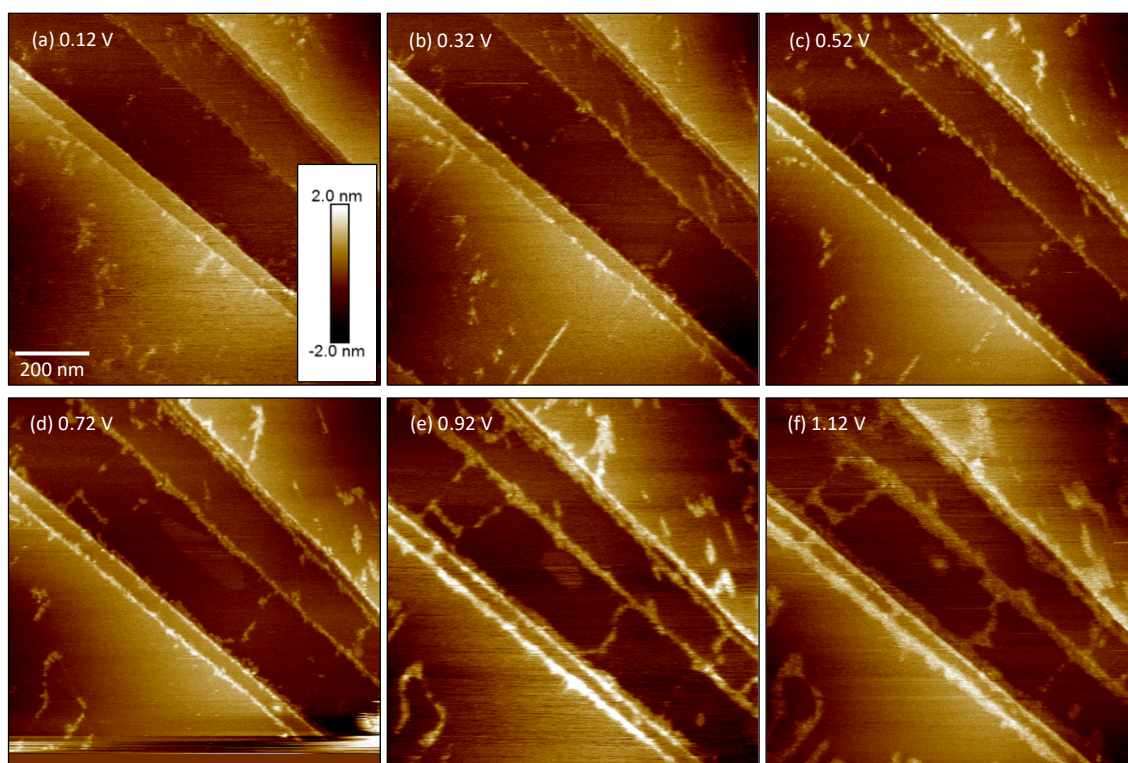
**Fig. 6.5:** (a) Cyclic voltammogram of HOPG in a solution of 1 mM  $\text{SiV}_3\text{W}_9$  and 0.1 M  $\text{H}_2\text{SO}_4$ , recorded at 50 mV/s in a conventional electrochemical cell with the same Pt-wire reference electrode used during the EC-AFM measurements. The set of redox waves around 0 V vs. NHE stem from the tungsten reduction and oxidation, the peaks around 1 V vs. NHE from vanadium, marked by the red circles in the graph. (b) Cyclic voltammogram of 0.5 mM  $\text{SiV}_3\text{W}_9$  in 0.1 M  $\text{H}_2\text{SO}_4$  on HOPG, recorded at 20 mV/s in the EC-AFM cell with a Pt-wire reference electrode. All potentials were converted to vs. NHE.

Two groups of redox waves, separated by several hundred mV, were observed in the CV in the external EC-cell (a). In a study of the same POM for a flow battery, Pratt et al assigned the peaks around 0 V vs. NHE to the tungsten atoms in the POM while the group centered around 1 V is the contribution from the  $\text{V}^{\text{IV}}/\text{V}^{\text{V}}$  redox reaction [180]. The redox wave around 0.8 V was found to be a combination of two peaks with a total transfer of two electrons while the second wave around 1.0 V is the result of a single electron transfer [180], together changing the oxidation state of the POM from  $\text{SiV}^{\text{V}}_3\text{W}^{\text{VI}}_9\text{O}_{40}^{7-}$  to  $\text{SiV}^{\text{IV}}_3\text{W}^{\text{VI}}_9\text{O}_{40}^{10-}$ . The small reduction peak at 0.3 V was attributed to desorption of POMs from the electrode surface [164]. A second CV was recorded in the EC-AFM cell (b) with similar parameters. The observed potential range was chosen to only contain the vanadium redox peaks. They are not as clearly pronounced as in the external cell, which is a result of several changed factors such as a lower scan rate, decreased POM

concentration and a different potentiostat. However, the redox peaks can still be clearly identified.

### 6.2.5 EC-AFM During Potential Steps

The POM concentration was reduced by one order of magnitude to 50  $\mu\text{M}$  to decrease the surface coverage (Fig. 6.6). Covering a potential window from 0.12 V to 1.72 V, the image series was started at the most negative potential where previous images showed only little adsorption. The potential was then increased stepwise by 0.2 V after each image. After reaching 1.72 V, the potential steps were reversed until a full cycle was completed. Between each potential step and the start of the EC-AFM scan, one full image was scanned that was not recorded, only the following second image was saved. This allowed the system to reach an equilibrium, detect possible surface-changes caused by the tip and to manually re-adjust the tip position to compensate for drift. With the scan rate used here, this amounts to a resting period between the presented images of 4:23 minutes and a total of 8:46 minutes at each potential. The unrecorded images showed that the structures on the surface are mostly stable and the influence of the microscope tip is minimal. In Fig. 6.6(a) at 0.12 V, the HOPG surface appears mostly free of adsorbates with only small amounts of POM agglomerations on terraces and step edges. Their height is around 1 nm which indicates that they consist of a monolayer of POMs. The surface does not change much until 0.72 V (d), which is located on the onset of the first oxidation wave in the CV. The only observed change in this potential range is an increasing coverage of the step edges.



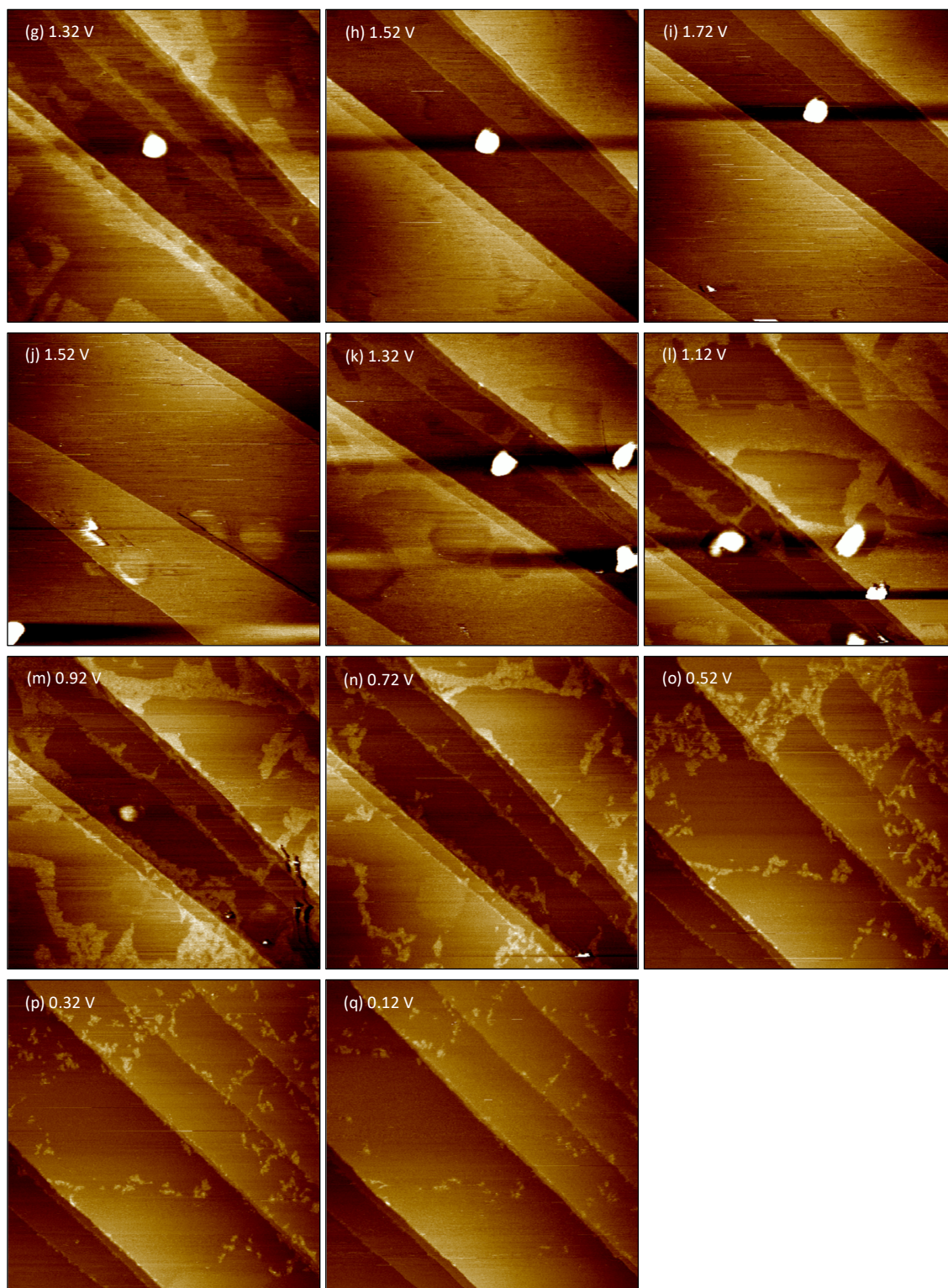


**Fig. 6.6:** Series of EC-AFM images ( $1\ \mu\text{m} \times 1\ \mu\text{m}$ ) of the HOPG surface in a  $50\ \mu\text{M}\ \text{SiV}_3\text{W}_9$  solution in  $0.1\ \text{M}\ \text{H}_2\text{SO}_4$  at different electrode potentials measured against a Pt-wire reference electrode and converted to vs. NHE. The measurement was started at  $0.12\ \text{V}$  vs. NHE with potential steps of  $0.2\ \text{V}$  up to  $1.72\ \text{V}$ , then decreased back to the starting potential. Microscope settings: ScanAsyst mode, scan rate =  $2\ \text{Hz}$ .

As has been shown above, POMs can adsorb at these sites even when no potential is applied. Therefore, it is not surprising that more POMs adsorb there with longer exposure time. Additionally, the increasingly positive electrode potentials reduce electrostatic repulsion between POMs and surface. In images (e) and (f), which were recorded near the maximum of and immediately after the second oxidation wave, the adsorbed structures begin to change. At constant thickness, they grow in lateral size. In images (g) to (l), at potentials positive of the vanadium redox waves, the POM structures have fully converted into large flat islands that cover large regions of the surfaces. At 1.52 V and above, the whole surface is covered by a full monolayer of the molecules. However, the lateral resolution of the measurement is not sufficient to show the ordered lattice structure. After decreasing the potential again below 1.52 V (k), several holes appear in the POM layer, increasing in size and number in the following image (l). In this potential region, few large clusters can be seen on the surface. With a height of several nanometers they are much larger than any of the other adsorbed structures. They are most likely not fully dissolved larger agglomerates of the POMs. Interestingly, when comparing the images of increasing and decreasing potentials, a small hysteresis effect becomes apparent around 1 V. At 1.12 V (f), the POMs still show some smaller clusters while at 1.12 V (l), they still remain in the shape of the large flat islands. This indicates that either the slow time-dependent adsorption still plays a strong role at decreasing potentials or that the potential dependent adsorption and desorption processes generally happen in long time scales. In images (m) and (n), recorded on the onset of the first wave and between first and second wave, the adsorbed structures shrink back into the initial smaller clusters. In the final images (o) to (q), recorded at potentials negative of the redox peaks, they decrease in number and leave a large part of the HOPG surface uncovered. A comparison of the first and last image of the series shows that the adsorption process is largely reversible with a similar surface coverage, shape and size of the  $\text{SiV}_3\text{W}_9$  clusters.

The in-situ EC-AFM measurement allows the continuous monitoring of the HOPG surface and observation of the process of progressively increasing surface coverage, from small adsorbed islands to the formation of a full layer of POMs. Throughout the measurement, the height of the observed structures does not increase, indicating that the full coverage formed at positive potentials consists of a single layer of POMs. This confirms the previous findings of Barteau et al. who came to the same conclusion by comparing the tunneling spectra measured on top of adsorbed POMs and between them [151]. The concept of the Born energy of solvation, which predicts increasing interaction with the surface when the POM becomes more oxidized, can be applied here as well. The AFM images show that the most drastic changes in POM surface coverage happen around the vanadium redox peaks, revealing a clear connection between the oxidation state of  $\text{SiV}_3\text{W}_9$  and its adsorption. In the potential regions both positive and negative of the redox peaks, the microscope images still show an increasing coverage with more positive potentials while the oxidation state of  $\text{SiV}_3\text{W}_9$  remains constant. This can be attributed to the increasing electrostatic

attraction between the negatively charged POMs and the HOPG surface. Comparing the results to the previous measurements of  $\text{Mn}^{\text{II}}_3\text{SiW}_9$ , the largest difference is the formation of a flat monolayer at more positive potentials instead of an increasing number of clusters. However, a direct comparison should not be made because of the different experimental conditions, e.g. the adsorption methods, measurement environment, supporting electrolytes and POMs.

### 6.2.6 Ordered Linear Structures

A more detailed analysis of the EC-AFM images revealed several areas on the surface that are covered by an ordered pattern of parallel lines. Interestingly, they are located on areas of the surface that are not covered by the previously described POM islands. Fig. 6.7 shows two magnified regions from Fig. 6.6(d) at 0.72 V in which large parts of the surface display the linear pattern. Due to the large imaged area of the original EC-AFM scan, the resolution of the individual lines is not ideal, but the pattern is clearly visible in the magnified images (b) and (c). The lines form domains with different orientations. The domains can extend over several 100 nm and are either separated by HOPG step edges or have straight borders between each other. Because different domain directions are present in single AFM line scans, it is unlikely that the pattern is simply the result of an AFM tip oscillation caused by external vibrations.

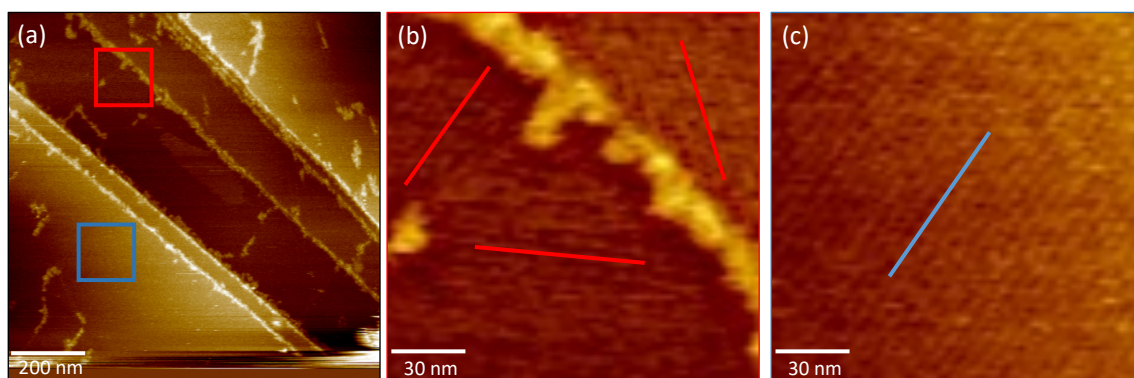


**Fig. 6.7:** (a) EC-AFM image of 50  $\mu\text{M}$   $\text{SiV}_3\text{W}_9$  solution in 0.1 M  $\text{H}_2\text{SO}_4$  on HOPG (from Fig. 6.6(d) at 0.72 V vs. NHE). The red and blue squares mark the areas magnified in images (b) and (c) respectively (150 nm x 150 nm, contrast increased). (b) Three domains of the parallel linear structures on the HOPG surface. The red lines indicate the orientation of the lines in each domain. (c) A large single domain of the linear structures.

This was confirmed by additional measurements at different scan rates in which the line spacing remained unchanged. For a more detailed analysis, higher resolution images were recorded (Fig. 6.8).

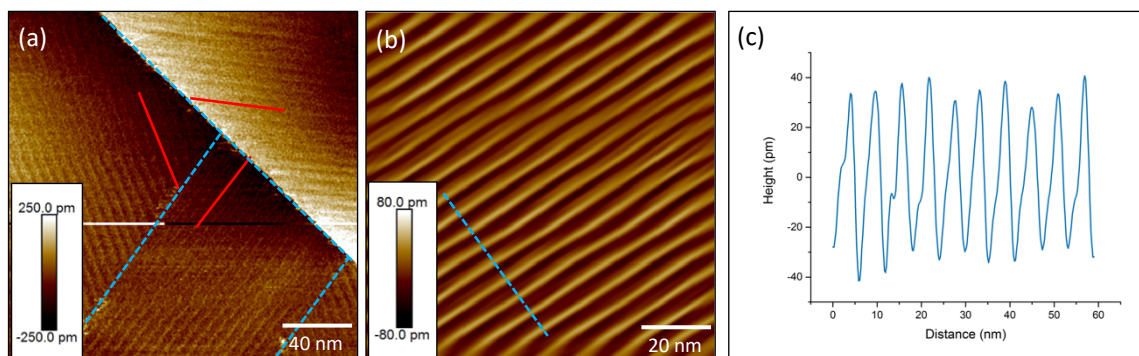


**Fig. 6.8:** (a) EC-AFM image (200 nm x 200 nm) of a HOPG surface in a 50  $\mu\text{M}$   $\text{SiV}_3\text{W}_9$  solution in 0.1 M  $\text{H}_2\text{SO}_4$  at 0.72 V vs NHE. The HOPG surface is covered by linear structures that appear in three different orientational domains. The domain boundaries are marked by the blue dashed lines, the orientation of each domain by the full red lines. (b) EC-AFM image (100 nm x 100 nm) of the linear structures, smoothed and Fourier-filtered. The dashed lines indicate the location of the line profile shown in (c). Microscope settings: ScanAsyst mode, scan rate = 2 Hz.

Fig. 6.8(a) shows the three possible orientations of the domains, rotated by  $120^\circ$  to each other and therefore following the rotational symmetry of the HOPG lattice structure. The top-right corner is separated from the rest of the image by a step edge that also defines a domain boundary. All other domains are located on the same terrace. For an analysis of the size of the linear structures, a higher resolution image (b) was Fourier-filtered before a line profile (c) was measured, averaged over a width of about 10 nm. The distance between two lines is 5.9 nm while their average height is only around 70 pm. Due to the low height of the structures, the AFM tip is not always able to resolve the pattern. In some images, it vanishes during larger parts of the measurements and the surface appears flat. An example for this is shown in Fig. 6.9(a), where the lines suddenly appeared half-way through the image (scan direction bottom to top). No measurement parameters were change while recording the image. Since this effect always happens simultaneously over the whole width of the scan, it is most certainly not a real representation of the surface structure. Instead, it must be caused by small changes in the resolution of the microscope tip. A result of a changed tip geometry due to attachment of particles in the solution such as small pieces of graphite, this is commonly experienced, especially in liquid environments. It is therefore possible that the structures cover the HOPG surface to a larger extent than the AFM images indicate. Fig. 6.9(a), recorded at 1.32 V vs. NHE, also shows that the lines are present at potentials both negative and positive of the vanadium redox reaction. It can be concluded that the formation of the lines is not connected to the vanadium oxidation state. It can be observed in several images that  $\text{SiV}_3\text{W}_9$  prefers the domain boundaries as adsorption sites (Fig. 6.9(b)). Also, the shape of the adsorbed islands often follows the direction of the lines. They assume an elongated rectangular shape with the same orientation as the lines (Fig. 6.9 (c)). This indicates that the pattern is already present on the surface when the POMs begin to adsorb and that it influences their adsorption process.

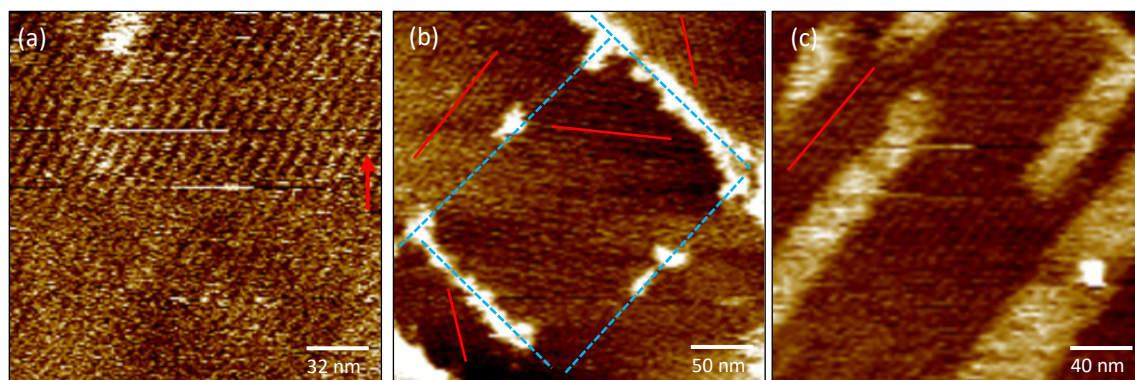


**Fig. 6.9:** EC-AFM scans of different samples of  $50 \mu\text{M SiV}_3\text{W}_9$  solution in  $0.1 \text{ M H}_2\text{SO}_4$ . (a) The linear structures are not always resolved by the AFM tip ( $160 \text{ nm} \times 160 \text{ nm}$ ,  $1.32 \text{ V vs. NHE}$ ). (b) POMs adsorb along domain boundaries (dashed blue lines). The red lines indicate the orientation in each domain (Magnified from Fig. 6.6 (d),  $250 \text{ nm} \times 250 \text{ nm}$ ). (c) The shape and orientation of adsorbed  $\text{SiV}_3\text{W}_9$  islands follows the direction of the lines ( $200 \text{ nm} \times 200 \text{ nm}$ ,  $1.32 \text{ V vs. NHE}$ ). Microscope settings: ScanAsyst mode, scan rate = 2 Hz.

Ordered linear structures have not previously been reported for systems of POMs in a simple electrolyte on HOPG surfaces. The resolution of EC-AFM is not high enough to resolve any internal structure of the lines and several attempts to image the surface with the EC-STM with better-resolution tips only produced images of the pristine HOPG lattice. Since neither the adsorbed POMs nor the linear structures could be found in EC-STM, this was most likely because the tip scratched off any material adsorbed on the surface. Therefore, to find an explanation for the lines, several different scenarios will be considered and their probability evaluated:

1. The lines are formed by  $\text{SiV}_3\text{W}_9$  in interaction with the electrolyte and the HOPG surface
2. The lines consist of one or several components of the electrolyte in interaction with the HOPG surface but do not contain POMs
3. The sample has been contaminated by an additional unidentified substance that forms the lines either alone or in combination with the POMs

In **Scenario 1**, the measured height and spacing of the lines do not match the POMs size of about 1 nm. Also, in all previous AFM and STM studies of Keggin POMs on HOPG the POMs have only been reported to form triangular lattices with an intermolecular spacing of roughly the size of the molecule. The observed potential dependent adsorption of the POMs also does not match this scenario because the lines already cover large areas of the surface at potentials below the vanadium redox reaction. Finally, the solution does not contain any components that have not also been used in other studies before and that could justify the formation of unexpected structures. While it might be a possible coincidence that this specific combination of POM and electrolyte on HOPG behaves

drastically different, in combination with the non-matching size, it is rather unlikely.

In **scenario 2**, the lines would have to consist of one or more of the components already present in the electrolyte: the sulfate anion  $\text{SO}_4^{2-}$ , the counterion  $\text{K}^+$  and water molecules. As in scenario 1, none of these is known to form linear structures on HOPG. The lateral spacing between the lines is an even greater mismatch with the size of these molecules that are much smaller than the POMs. Only the observed low height of the lines speaks for this scenario. It should be mentioned that sulfates are known to form ordered adlayers of parallel lines on metal single crystal surfaces such as Pt(111) in a certain potential range. These were interpreted by Funtikov et al. as a co-adsorbate of sulfate anions and water molecules [181]. However, not only are the conditions on these substrates very different from HOPG but also was the line spacing of this lattice ( $\sqrt{3}$  times the underlying lattice spacing) much smaller than the 5.9 nm observed in the experiments in this work.

Therefore, **scenario 3** must also be considered. The possibility of a contamination of the sample with organic substances is very small. The EC-AFM setup was new and before these experiments it had always only been used with POMs in sulfuric acid. The EC-AFM cell was thoroughly cleaned before experiments on a new material system to prevent cross-contamination. The HOPG surface was freshly cleaved before every measurement and the POM solution was freshly prepared again after the lines were first observed to exclude the possibility of a contaminated sample. Additionally, neither CVs nor an *energy dispersive X-ray spectroscopy* (EDX) analysis of one of the samples showed any indication of contamination. On the other hand, POMs have been reported to form linear structures on HOPG when they were combined with organic surfactants. Wu et al. [182] and Raj et al. [183] have both reported POMs encapsulated by the surfactant *dimethyldioctadecylammonium* (DODA) to form arrays of linear structures on HOPG surfaces. These structures exhibit the same  $120^\circ$  rotational symmetry (Fig. 6.10) as the lines found here. In both cases and in contrast to the measured data, the arrays of lines assume the form of islands between which the underlying pristine HOPG surface is visible. On the other hand, control images of pure DODA adsorbed on HOPG closely resemble the lines observed in this study. In both publications, the spacing of the lines in the images incorporating the POMs matches the size of a POM with an extended DODA molecule attached on each side. Wu et al. state that the organic DODA adlayer increases the barrier for lateral diffusion and therefore forms a template for the adsorption of the POM that leads to the formation of the linear arrays. Speaking against this type of contamination here is the fact that they could not obtain a stable assembly of the pure DODA molecules on the surface in in-situ measurements. According to Raj et al., the close size match of the DODA (0.251 nm) and the HOPG lattice spacing (0.246 nm) leads to the formation of the DODA chains on the surface which then appear as lines in the microscope images. When the ratio of DODA to POMs was increased, they observed both the arrays with POMs and the linear structures of pure DODA on the surface next to each other.

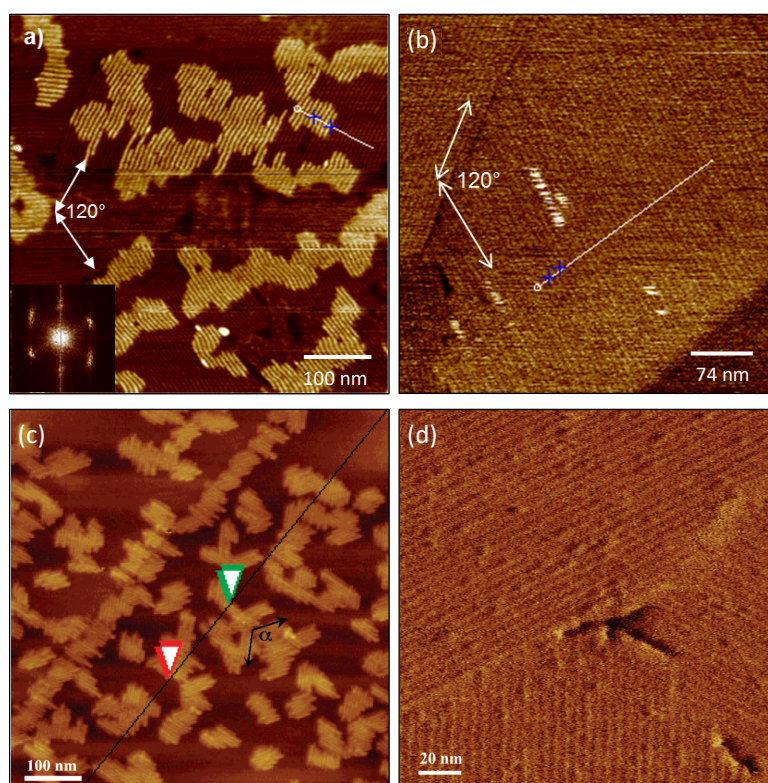


**Fig. 6.10:** AFM images in air, adapted from Raj et al. [183] (top row, evaporated from solution) and Wu et al. [182] (bottom row, spin-coated). They show the formation of linear structures of DODA encapsulated POMs (left) and pure DODA (right) on HOPG surfaces. The POMs used were  $PW_{12}O_{40}$  (a) and  $P_5W_{30}O_{110}$  (c).

Considering all observations, scenario 3, a contamination of the sample with an organic substance of similar size and properties as DODA, would certainly provide the best suited explanation for the effect. It would justify the size of the structures, their orientational behavior and the influence on the adsorption of POMs. On the other hand, in addition to the measures taken to prevent this kind of contamination, there is no evidence for its presence in CVs and EDX. The images from [182] and [183] show a different surface structure when POMs are added to the system and the DODA lines were only observed ex-situ. Also, scenario 2 with the possibility of an ad-lattice of sulfate and water molecules similar to the ones observed on Pt(111) [181] should not be completely dismissed. To understand the origin of the lines, it will therefore be necessary to perform higher-resolution microscopy that resolves their internal structure. A reproduction of the images in a different setting would also allow to dismiss scenario 3 completely.

### 6.3 Influence of Electrolyte Composition and POM Charge

As mentioned before, the influence of electrolyte components and the POM's charge on the adsorption and aggregation behavior have so far mainly been investigated in

simulations and in some cases the results have been inconclusive. To address the problem experimentally, different Keggin POMs were dissolved in several aqueous solutions from which they were adsorbed on HOPG and imaged with AFM.

### 6.3.1 Experimental

50  $\mu\text{M}$  solutions of the POMs were ( $\text{H}_3\text{PW}_{12}\text{O}_{40}$ ,  $\text{H}_4\text{SiW}_{12}\text{O}_{40}$  and  $\text{H}_9\text{PW}_9\text{O}_{34}$ ) were prepared in different aqueous solvents ( $\text{H}_2\text{O}$  or  $\text{H}_2\text{SO}_4$ ,  $\text{H}_3\text{PO}_4$ ,  $\text{HCl}$ ,  $\text{Li}_2\text{SO}_4$  and  $\text{LiClO}_4$  in 0.1 M concentration). The HOPG sample was immersed into the solution for 60 seconds during which it was slowly moved around with a pair of tweezers. The procedure was then repeated in MilliQ water to guarantee only adsorbed POMs remain on the sample. After the sample had fully dried under ambient conditions, tapping mode AFM images were recorded in air. This method proved to have a smaller impact on the adsorbates than ScanAyst mode in the dry measurements. It was also found that larger area scans are less likely to damage the surface. Therefore, scan sizes of several  $\mu\text{m}$  were chosen for an accurate imaging of the adsorbed POMs. Each sample was measured at least three times at different positions, more than 1 mm apart, to obtain results representative of the whole surface.

### 6.3.2 Different POMs

Three different tungsten-based Keggin POMs were used in this experiment: The isostructural  $\text{SiW}_{12}\text{O}_{40}^{4-}$  ( $\text{SiW}_{12}$ ) and  $\text{PW}_{12}\text{O}_{40}^{3-}$  ( $\text{PW}_{12}$ ) as well as its highly charged lacunary  $\text{PW}_9\text{O}_{34}^{9-}$  ( $\text{PW}_9$ ). The same measurements were performed with the POMs dissolved in de-ionized water (Fig. 6.11 top row) and in 0.1 M sulfuric acid (Fig. 6.11 bottom row).

The size and shape of the adsorbed structures differ greatly on each sample. In water,  $\text{PW}_{12}$  (a) forms many irregularly shaped islands of varying size. The magnification shows that the larger islands consist of groups of smaller particles with a measured height between around 1.3 nm which is close to the size of a single POM. Only in few cases, they form higher clusters that reach heights of up to 5 nm. The lateral size of single particles was measured between 10 and 50 nm, indicating that they are agglomerations of POMs. The smallest islands consist of only one of those POM clusters. The HOPG step edge is fully covered by the POM clusters.  $\text{SiW}_{12}$  (b) adsorbs mostly as evenly distributed particles of similar height around 1.3 nm. Their lateral size of 10 - 30 nm is, on average, much smaller than the individual  $\text{PW}_{12}$  clusters. Larger islands are only found at locations where HOPG step edges form sharp corners. The large size difference between these islands and the small particles adsorbed on the basal planes indicates that the POMs in the larger islands are bound to the substrate at least partially through interactions with POMs adsorbed at the step edges. The coverage of the basal plane is much lower than on the

PW<sub>12</sub> sample and is a sign of weaker interaction with the surface, as is expected from the Born energy of solvation introduced in eq. ( 6.1 ). The large flat islands of PW<sub>9</sub> (c) mostly have diameters over 100 nm and are only around 0.7 nm high. The lower height can be explained by the smaller size of the tri-lacunary PW<sub>9</sub>, compared the plenary POMs PW<sub>12</sub> and SiW<sub>12</sub>. The increased surface coverage compared to the SiW<sub>12</sub> sample does not follow the concept of the Born energy of solvation anymore. Because of the smaller size and higher negative charge, the interaction with the surface should be much lower than for the other two POMs. This shows that other factors must be influencing the adsorption behavior. The round shape and large lateral size of the islands also indicates a stronger POM-POM attraction.

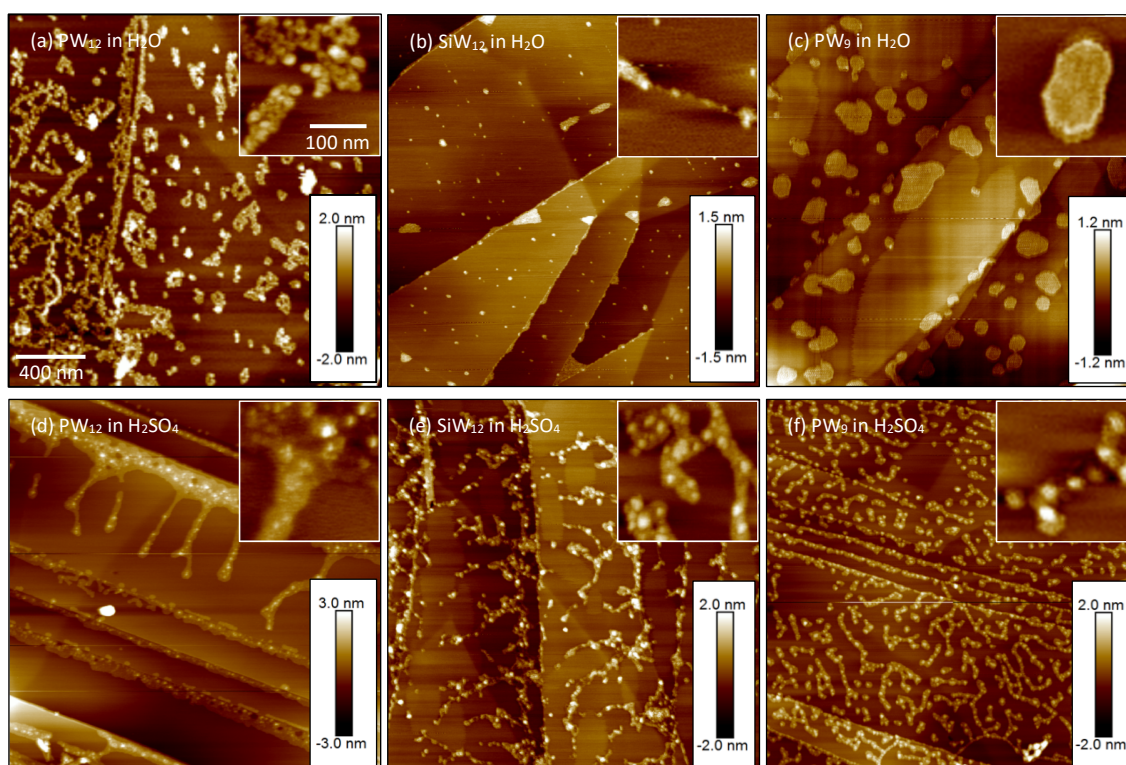


**Fig. 6.11:** AFM image series ( $2 \mu\text{m} \times 2 \mu\text{m}$ ) of different POMs, adsorbed on HOPG surfaces by immersing the sample in a  $50 \mu\text{M}$  solution of the POM in de-ionized water **(a)-(c)** and in  $0.1 \text{ M}$   $\text{H}_2\text{SO}_4$  **(d)-(f)**. The images were recorded after rinsing and drying the sample with the following POMs: **(a),(d)** PW<sub>9</sub>, **(b),(e)** SiW<sub>12</sub> and **(c),(f)** PW<sub>12</sub>. The insets in the top right corner are  $200 \text{ nm} \times 200 \text{ nm}$  magnifications of the adsorbed structures. Microscope settings: TM-AFM, scan rate = 2 Hz.

In  $\text{H}_2\text{SO}_4$ , PW<sub>12</sub> (d) adsorbs almost completely in an up to 200 nm wide zone along the lower side of the step edges. On the larger terraces, several elongated features extend out of this area away from the step edge. The adsorbed structures are around 1.2 nm high and their flat surface is covered by many 2 - 3 nm high smaller particles with lateral sizes between 10 and 20 nm. Compared to the water sample of PW<sub>12</sub>, the coverage of the basal plane has dramatically decreased while it is much higher around the step edges. This could

be caused by a decreased strength of interaction with the surface as well as stronger attraction between POMs. The adsorbed structures of  $\text{SiW}_{12}$  (e) show a similar behavior. Most islands are connected to the step edges and consist of a 1.2 nm high POM monolayer, covered by 2-3 nm high and 10-30 nm wide particles. However, the number of islands has increased and they split into multiple branches on the basal plane, resembling the percolated clusters in Fig. 6.2(d). Unlike in water, the adsorption strength appears to increase here compared to  $\text{PW}_{12}$ . The shapes of the islands formed by  $\text{PW}_9$  (f) resemble those formed by  $\text{SiW}_{12}$ . However, they are shorter and distributed equally over the whole basal plane, often not connected to step edges. Therefore,  $\text{PW}_9$  shows the strongest adsorption of all three POMs. As in water, the height of the  $\text{PW}_9$  islands is lower (0.8 nm) than of the other two POMs and even the particles on top of the islands are smaller (1.2 - 1.4 nm). The two square shaped areas that are free of adsorbates are locations of previous attempts to obtain higher resolution images. During these, the tip removed all adsorbed material. Overall, the  $\text{H}_2\text{SO}_4$  samples differ from the  $\text{H}_2\text{O}$  series in two major points. The presence of small particles that cover the surface of the islands and the elongated, branching island shape.

### 6.3.3 Different Solvents

The previous images show the strong influence of the solvent on the formation of adsorbed islands. To obtain a wider range of data on the influence of anion and cation in the electrolyte, the same deposition method was used to adsorb  $\text{SiW}_{12}$ , dissolved in several more different solvents (Fig. 6.12). As in the previous experiment, each sample formed islands of different shapes on the HOPG surface. The images of  $\text{SiW}_{12}$  in  $\text{H}_2\text{O}$  (a) and  $\text{H}_2\text{SO}_4$  (b) are only shown for comparison, they have already been discussed above. Dissolved in  $\text{Li}_2\text{SO}_4$  (c), the POM forms larger islands that all have a nearly circular shape. With 1.8 nm, they are higher than the islands on any previous sample. However, as the magnified image shows, they are often connected by a lower second layer which is only around 1.0 nm high. This indicates that the islands consist of a double layer of POMs, surrounded or connected by a POM monolayer. In  $\text{HCl}$  (d), adsorption on the basal plane is rather weak and most 1.2 nm high islands are connected to the step edges. In  $\text{LiClO}_4$  (e), the surface coverage is even lower, few islands are adsorbed along the step edges. On the terraces, several smaller islands can be seen with diameters below 50 nm. Both island types have the same height of 1.0 nm. On the  $\text{H}_3\text{PO}_4$  sample (f), in contrast to all other samples, two different regions were found on the surface, separated by a large HOPG step edge. On the left side (Region B), the terraces are covered by many small islands while on the right (Region A), fewer but larger islands dominate. Fig. 6.13 shows separately recorded images of the two different types of regions for a better contrast. In region A (b), the small islands (below 100 nm diameter) are evenly distributed while in region B (c), an affinity towards step edges, where larger islands are found, is recognizable. On average, the islands on the terraces have a larger diameter than in region A but are less

numerous. While all islands in region B are around 1 nm high, the island height in region A varies between 1 nm and 2.5 nm.

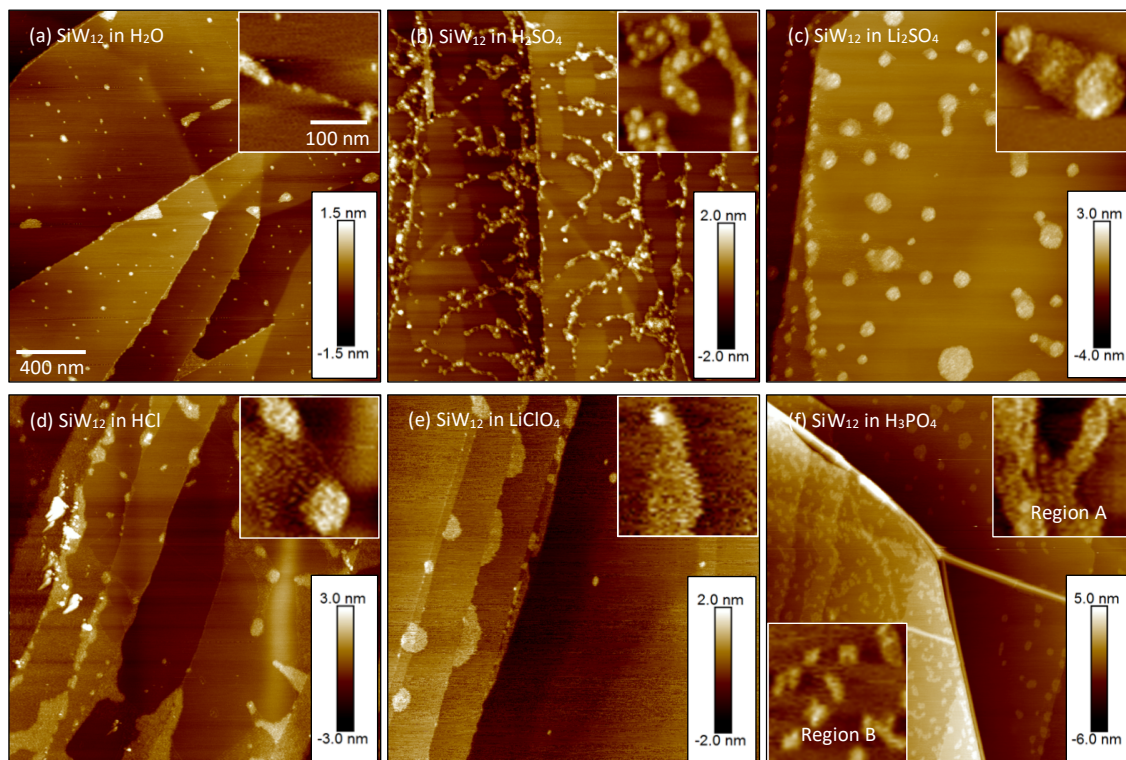


**Fig. 6.12:** AFM image series ( $2 \mu\text{m} \times 2 \mu\text{m}$ ) of  $\text{SiW}_{12}$ , adsorbed on a HOPG surface by immersing the sample in a  $50 \mu\text{M}$  solution of the POM in de-ionized water **(a)** or a  $0.1 \text{ M}$  concentration of **(b)**  $\text{H}_2\text{SO}_4$ , **(c)**  $\text{Li}_2\text{SO}_4$ , **(d)**  $\text{HCl}$ , **(e)**  $\text{LiClO}_4$  and **(f)**  $\text{H}_3\text{PO}_4$ . The images were recorded after rinsing and drying the sample. Microscope settings: TM AFM, scan rate = 2 Hz.

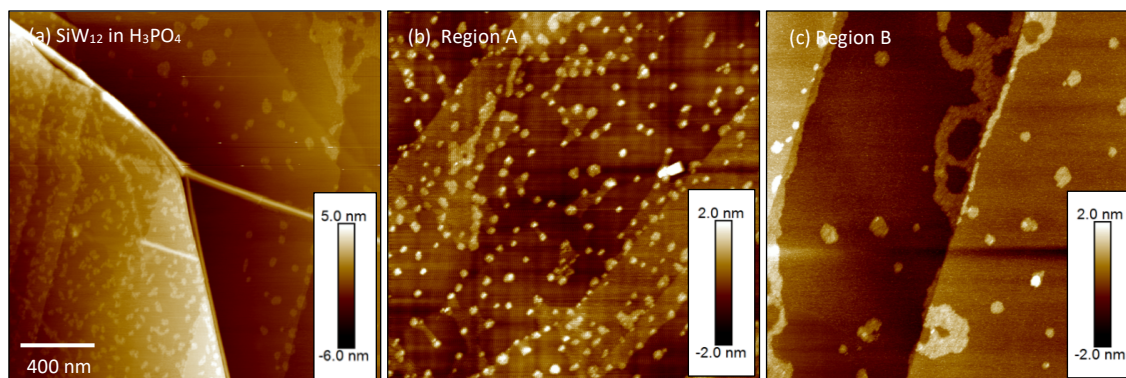


**Fig. 6.13:** Different regions on the  $\text{SiW}_{12}$  in  $\text{H}_3\text{PO}_4$  sample ( $2 \mu\text{m} \times 2 \mu\text{m}$ ). **(a)** is the original image from Fig. 6.12 (f) for comparison, **(b)** and **(c)** were measured at different positions.

To test if any of the observed structures are simply caused by the pure solvent, the measurements were repeated without POMs for some of the solvents (**Fig. 6.14**). None of the pure solvents formed the kind of larger islands that were found on most POM samples. The small clusters encountered instead have diameters below 50 nm. On the  $\text{H}_2\text{SO}_4$  sample (a), the particles appear larger but their odd shape is caused by an effect

known as “multi-tip”. Foreign particles have attached to the tip’s apex, forming several points that equally contribute to the measured signal. Therefore, their actual size is smaller than the image suggests. The particle height in all images is much less uniform than on the POM samples, ranging between 1 and 3 nm. The only exception is the HCl sample (c), where 0.5 nm high particles were also observed. With as small as 10 nm, their diameter is also smaller. The coverage is mostly limited to the step edges. Interestingly, the H<sub>3</sub>PO<sub>4</sub> sample closely resembles region A of the SiW<sub>12</sub> in H<sub>3</sub>PO<sub>4</sub> sample (Fig. 6.13(b)). Not only is the distribution on the surface similar, but also the particle height and size distribution. A possible explanation for the different regions on the SiW<sub>12</sub> on H<sub>3</sub>PO<sub>4</sub> sample is therefore, that region A does not contain any POMs and only region B shows the adsorbed SiW<sub>12</sub> islands.

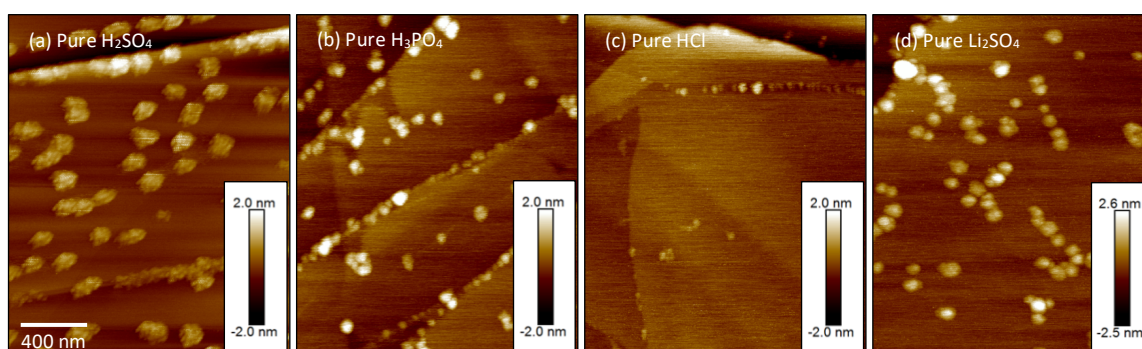


**Fig. 6.14:** AFM images ( $1.6 \mu\text{m} \times 2 \mu\text{m}$ ) of an HOPG surface after immersion into a 0.1 M concentration of different solvents for 60 s followed by rinsing in water. (a) H<sub>2</sub>SO<sub>4</sub>, (b) H<sub>3</sub>PO<sub>4</sub>, (c) HCl and (d) Li<sub>2</sub>SO<sub>4</sub>. Microscope settings: TM AFM, scan rate 2 Hz.

The images in different solvents can be compared by several categories. The type of counterion (Li<sup>+</sup> vs. H<sub>3</sub>O<sup>+</sup>) does not show any direct influence on the adsorbed structures except a possible tendency to form rounder islands in the presence of Li<sup>+</sup>. The type of anion in the solvent was already shown to be important in the previous section and this is further emphasized here. Comparing the H<sub>2</sub>O sample to all others, it appears that the presence of any anion besides the POM results in larger islands and must therefore be a critical factor in their formation. Both sulfate containing samples show structures significantly higher than a POM monolayer which might be a sign that the presence of sulfate encourages three-dimensional growth. However, the particles on the H<sub>2</sub>SO<sub>4</sub> sample differ too much from the dual-layer islands in Li<sub>2</sub>SO<sub>4</sub> to be certain of this effect. No trend is recognizable when comparing the samples by their pH value. Most acidic are the HCl and H<sub>2</sub>SO<sub>4</sub> solutions (pH ≈ 1), followed by H<sub>3</sub>PO<sub>4</sub> (pH ≈ 1.6). The other three samples have a much higher, nearly neutral pH, even though the addition of POMs makes the solutions somewhat more acidic.

### 6.3.4 Analysis of the Results

The unique POM structures observed in the AFM images of each sample show clearly that no single parameter dominates adsorption and aggregation. Instead, a combination of different factors - the POM's charge, the type of counterion and the presence of other anions in the solution – is responsible. These factors all influence the interaction between POMs and HOPG surface as well as from POM to POM and result in a different adsorption behavior for every sample. The only finding common to all samples is the monolayer thickness of most islands. This agrees well with previous STM and AFM studies of POMs adsorbed on HOPG [151], [159]. The lower island height of the PW<sub>9</sub> samples is a direct result of the POM's reduced size.

The much smaller island size of SiW<sub>12</sub> in water compared to PW<sub>12</sub> confirms the simulation results from Chaumont and Wipff [171], Bera et al. [172] and Serapian and Bo [174], that the lower negative charge of PW<sub>12</sub> leads to stronger attraction between the POMs, causing them to form larger clusters on the HOPG surface. The lower surface coverage of SiW<sub>12</sub>, caused by its smaller surface activity, also fits into this picture. The fact that the tri-lacunary PW<sub>9</sub> forms larger islands without holes indicates an even stronger POM-POM attraction than PW<sub>12</sub>. This means that the Born solvation energy alone does not determine the POMs behavior anymore. Instead, the concept of counterion bridging for highly negative anions should be the reason for this behavior [171],[174]. In H<sub>2</sub>SO<sub>4</sub>, the results do not fit into either model. The decreasing island size with increasing negative charge agrees with the findings of Bera et al. [172], where the pH of the analyzed solution was similar to the H<sub>2</sub>SO<sub>4</sub> solution used in this work. This indicates that the, on the first glance contradicting, results of increased POM-POM attraction for the most negative POMs by counterion bridging [171],[174] on the one hand and increasing electrostatic repulsion [172] on the other hand, is the consequence of the different pH values of the analyzed POM solutions. However, it does not explain the higher surface coverage of the more negative POMs nor the island shape of long branching chains with embedded clusters. These characteristics must therefore be caused by the presence of the sulfate anions.

In [169], H<sub>3</sub>O<sup>+</sup> and Li<sup>+</sup> counterions resulted in similar aggregation behavior. However, the shape and size of the adsorbed islands observed here greatly differs on the H<sub>2</sub>SO<sub>4</sub> and Li<sub>2</sub>SO<sub>4</sub> AFM samples which implies that the adsorption behavior is more strongly influenced by the counterion than the aggregation in solution. Even more interesting is the strong influence of the solution's anion on the POM-POM attraction. It becomes evident when comparing the water sample, free of anions besides the POM, to all samples on which the adsorbed islands are invariably much larger. Even in HCl, where Bera et al. did not detect any influence of the chloride anion on adsorbed POMs [172], the differences to SiW<sub>12</sub> in water are clearly visible. The influence of these anions has not been investigated before and should be part of future MD simulations in order to understand

their role in POM aggregation. Further AFM measurements with a wider range of POMs and electrolytes, varying concentrations and other substrates will also help to understand the details of these interactions.

## 7 Discussion and Conclusions

The goal of this work was to show how the combination of high-resolution scanning probe microscopy and electrochemical measurements, either in the form of EC-SPM or in separate electrochemical and SPM experiments, can be applied to create a better understanding of the fundamental processes in energy storage materials. With the possibility to image electrode surfaces in molecular resolution and to directly monitor electrochemical processes, SPM has a unique advantage over other electrochemical methods. With this in mind, in this chapter the findings presented above will be discussed.

### 7.1 Improving the Understanding of SECPM

SECPM can be a powerful tool for the analysis of the electrochemical double layer structure and the electrochemical properties of electrode surfaces as well as the molecules adsorbed on those surfaces. Because a thorough understanding of these factors is crucial when it comes to the development of new battery materials, SECPM should be the method of choice for a large number of experiments in this field of research. A more widespread use is however hindered by the difficult interpretation of the pictures; any analysis method will only be commonly accepted if the results can be properly understood. This was the reason for the decision to focus the research with SECPM on the method itself rather than using it for the investigation of material properties.

The comparison of images recorded in different concentrations of sulfuric acid, as well as the investigation of the step-edge oscillation artifact at different working electrode potentials, showed that the image quality and resolution of SECPM are greatly affected by the Debye length of the electrochemical double layer. The lower ion concentrations at potentials around the PZC result in a flatter potential vs. distance profile which decreases both lateral resolution, because of a greater distance between tip and surface, and z-resolution, due to a resulting flatter potential-distance profile. This behavior is intrinsic to SECPM and it will not be possible to solve the problem completely, the measurements show that the increase of the ion density in the EDL, either through increased electrolyte concentration or simply measuring at different potentials, helps to increase the quality of the images. Additionally, it appears as if the tip itself also plays a role since some tips are more affected by this issue than others. Investigations of the influence of tip shape, coating and material would therefore be an important topic for future investigations. Furthermore, it was found that the oscillation artifact at HOPG step edges is caused by the microscope's feedback loop that most likely overcompensates for changes when adjusting the tip height after passing the step. Interestingly, the oscillations can also be

decreased by generating a steeper potential curve through potential adjustments. Although it has not been tested, changes in electrolyte concentration are therefore expected to have the same effect on the oscillations and the proposed solutions for improved image quality can also be applied here. However, it will still be an important task to perform a thorough analysis of the feedback loop system itself to eliminate the oscillations completely.

The description of SECPM in the microscope's instruction manual states that "*SECPM measures the potential difference between its potentiometric probe and sample, immersed in an electrolyte or polar liquid*" [184]. The successful SECPM imaging in the non-polar and practically ion-free ethylene glycol shows that this statement should be revised. The imaging the atomic structure of the HOPG surface shows a level of resolution that is not expected from the potential mapping mechanism and gives rise to a fundamental question: Is such a high resolution possible if only the potential differences within the electrochemical double layer are displayed? In STM, the high resolution is a result of the exponential dependence of the tunneling current on the distance between tip and sample. In contrast, the relation between potential and distance that defines the resolution of SECPM measurements has been reported to take a sigmoidal shape close to the electrode surface where the measurements take place [55], [56], [61]. With this signal-distance relation, the ability to resolve images on an atomic level cannot naturally be expected and explained.

The discussion started by Traunsteiner et al. [90], in which they conclude that the measured potentials are the result of leakage currents, in particular from electron tunneling, provides a disappointing but plausible alternative explanation for the results. Considering that the microscope's hardware was specifically designed to prevent those currents and the fact that Baier et al. were able to show clear differences between SECPM and EC-STM images [59], the issue is in need of further investigation. For instance, it is possible that an intermediate case is closest to reality, where the tip indeed measures the local potential in the EDL but is influenced by tunneling currents. Assuming that the distance between tip and sample during a measurement is in a similar range in both STM and SECPM (well below 1 nm), the complex structure of the overlapping EDLs of tip and sample must also be considered. With the high input impedance amplifier preventing the flow of currents, another option should be taken into account. The tunneling currents might simply charge and discharge these double layer capacitances instead of flowing through the whole setup, affecting the local environment sufficiently to be detected. However, it is difficult to determine the exact origin of the measured potentials experimentally alone. To solve the problem, it will therefore be an important step to also develop a comprehensive theoretical model that analyzes the effects of a possible tunneling current on the measured potentials and incorporates the previous simulations on the effect of tip shape and EDL overlap by Hamou et al. [86]–[89]. The model should

also be able to accurately describe all available experimental results, including both SECPM images and potential-distance curves. Only when this fundamental mechanism behind SECPM is well understood will it be possible to apply the method more extensively. It can be expected that the contributions of this work to the discussion will help to solve said issues and help SECPM to make the next step forward.

## **7.2 Influence of Water on the Double Layer Capacitance of Ionic Liquids**

The main findings of this chapter are the variations found in the capacitance curves with different water content. All measured capacitance vs. potential curves display a characteristic peak and show a general increase in capacitance at more positive potentials. From these results it can be concluded that the water molecules in the ionic liquid adsorb on the Au(111) surface. This adsorption increases with stronger electrode polarization, confirming the results of previous experimental [127], [128] and theoretical [124]–[126] studies. However, a conclusive interpretation of the curves was only possible with the help of additional EC-STM measurements of the Au(111) surface which showed that the characteristic peak in the curves was not caused by a surface reconstruction instead. Monitoring the electrode in-situ on a scale that can detect a surface reconstruction would not have been possible with conventional electrochemical methods. This constellation is a great example for how EC-SPM can augment other electrochemical measurements to allow a more thorough analysis of the materials.

As mentioned above, the discussion about the exact nature of the EDL in ionic liquids is still very much ongoing and far from conclusion [109], [110], [111], [127], [128]. It would therefore be of significant importance for future progress to further analyze the EDL structure experimentally. The results presented here are considered a first step towards the goal of establishing double layer capacitance measurements as another means to analyze the electrochemical double layer. The method could be greatly enhanced if combined with additional SECPM measurements, in particular potential vs. distance curves. Making an experimental connection between the double layer capacitance on the one hand and the potential distribution on the other hand would be a further step towards a complete understanding of the EDL in ionic liquids.

## **7.3 POM Adsorption**

In the first part of the chapter about the adsorption of POMs, the influence of their oxidation state was analyzed. The combination of measurements in a conventional

electrochemical cell and ex-situ AFM images showed clearly that the Keggin-type POM  $\text{Mn}^{\text{II}}_3\text{SiW}_9$  only adsorbs on HOPG surfaces when the Mn atoms are oxidized to  $\text{Mn}^{\text{IV}}$ . It could be deduced from the cyclic voltammograms that the size (due to ligand exchange) and charge (due to oxidation/ reduction) determine if the molecules adsorb on the HOPG surface or not. However, it was only because of the accompanying AFM images that the hypothesis could be proved by showing the actual surface coverage at the different oxidation states and the reversibility of the adsorption. The experiment is another representation of how the high resolution of SPM can gather additional information that helps to confirm and explain the results of other measurements. Making full use of the microscopes capabilities to performing in-situ electrochemical measurements, the influence of the oxidation state of POMs was analyzed in more detail in the an EC-AFM image series of  $\text{SiV}_3\text{W}_9$ . In these experiments, the influence of Vanadium oxidation was explored in great detail. The direct observation of the effect of potential changes showed not only a clear increase in the number of adsorbed POMs once after they were fully oxidized but also an additional, much slower adsorption process. This slow adsorption is either caused by increased electrostatic interactions between POM and surface or is completely independent on the applied potential and purely time-based instead. The effect manifests itself in slowly increasing coverage of the surface as well as a small hysteresis effect upon reversal of the direction of potential steps. A large difference in the distribution of the adsorbed POMs was found between the in-situ and ex-situ AFM images. While the POMs on the dry samples were almost exclusively found at and around the step-edges of the HOPG surface, the in-situ measurements confirmed that they also adsorb in large amounts on the HOPG basal plane and eventually even cover the whole surface at more positive potentials. Some difference can of course be expected because of the different POMs used in the two experiments. However, the removal from the electrolyte and the following drying process are likely to influence the distribution of the POMs on the surface because of their weak interaction with the HOPG basal plane. Both the slow adsorption process and the coverage of the basal plane could only be detected in the in-situ measurements which shows how important it is to measure electrochemical processes directly where they occur if the goal of the experiment is to understand the fundamental details.

In the second part of the chapter, the influence of several properties of POMs and solvent on their adsorption was analyzed, comparing the Keggin POMs  $\text{PW}_9^{9-}$ ,  $\text{PW}_{12}^{3-}$  and  $\text{SiW}_{12}^{4-}$  in different solvents with AFM on dried POM samples. The images revealed a great variation in the structures of POM agglomerates, influenced by the POMs' charge as well as the type of anions and cations in the electrolyte they are dissolved in. Only with the high-resolution AFM images could the unique structures formed by each combination of POMs and electrolyte be investigated. While it is not possible to fully explain all details from such a limited number of analyzed material combinations and the dependence on many different factors, the results show that the adsorption is also strongly influenced by

the interactions between the POMs and not only between POMs and surface. The measurements also showed that the anions in the solution can play a big role in the formation the POM agglomerates. The different findings in these experiments also show that many influences on the adsorption of POMs are still unknown or at least not fully understood and it is expected that the results of the AFM studies will serve as a starting point for further investigations of more material combinations and in-situ measurements to be eventually able to predict how a POM would behave in a specific electrolyte.

## 7.4 Concluding Remarks

As mentioned in the introduction in chapter 1, it is crucial for the development of truly novel batteries to understand material properties and electrochemical processes on a fundamental level. The findings in this work show that the combination of highly resolved images and direct in-situ observations in almost real-time that is provided only by electrochemical SPM methods is able to reveal properties that would remain undetected with other experimental techniques. The discoveries in both the areas of polyoxometalates and ionic liquids show what the use of SPM can achieve when it comes to the in-depth analysis of battery materials, be it in the combination with other electrochemical methods or on its own. Therefore, it is expected that the investigations of scanning electrochemical potential microscopy presented in this work and the concluding suggestions on how to achieve a better resolution and image quality, as well as the eventual conclusion of the discussion about the mechanisms behind the measured potentials, will help to achieve the establishment of SECPM as a common analysis method for battery materials. Directly probing the potential profile of the double layer in ILs could greatly improve the understanding of the structure and formation of the EDL and in-situ monitoring of POM adsorption will enable the direct observation of changes in the molecule's oxidation state and will further enhance the understanding of those versatile molecules. When SECPM finally becomes fully established, it will be of great help to the progress of battery research, one of the most important scientific fields of our times.



## 8 Bibliography

- [1] G. Binnig, H. Rohrer, C. Gerber, and E. Weibel, "Surface Studies by Scanning Tunneling Microscopy," *Physical Review Letters*, vol. 49, pp. 57–61, 1982.
- [2] R. Sonnenfeld and P. K. Hansma, "Atomic-resolution microscopy in water.," *Science*, vol. 232, pp. 211–213, 1986.
- [3] K. Itaya and E. Tomita, "Scanning tunneling microscope for electrochemistry - a new concept for the in situ scanning tunneling microscope in electrolyte solutions," *Surf. Sci.*, vol. 201, no. 3, pp. 507–512, 1988.
- [4] V. Lockett, M. Horne, R. Sedev, T. Rodopoulos, and J. Ralston, "Differential capacitance of the double layer at the electrode/ionic liquids interface," *Phys. Chem. Chem. Phys.*, vol. 12, pp. 12499–12512, 2010.
- [5] T. Pajkossy and D. M. Kolb, "The interfacial capacitance of Au(100) in an ionic liquid, 1-butyl-3-methyl-imidazolium hexafluorophosphate," *Electrochem. commun.*, vol. 13, pp. 284–286, 2011.
- [6] H. Wang, S. Hamanaka, Y. Nishimoto, S. Irle, T. Yokoyama, H. Yoshikawa, and K. Awaga, "In operando X-ray absorption fine structure studies of polyoxometalate molecular cluster batteries: Polyoxometalates as electron sponges," *J. Am. Chem. Soc.*, vol. 134, pp. 4918–4924, 2012.
- [7] J. Friedl, R. Al-Oweini, M. Herpich, B. Keita, U. Kortz, and U. Stimming, "Electrochemical studies of tri-manganese substituted Keggin Polyoxoanions," *Electrochim. Acta*, vol. 141, pp. 357–366, 2014.
- [8] H. Gerischer and W. Ekardt, *Fermi Levels in Electrolytes and the Absolute Scale of Redox Potentials*, vol. 43. 1983.
- [9] N. D. Lang and W. Kohn, "Theory of Metal Surfaces: Work Function," *Phys. Rev. B*, vol. 3, pp. 1215–1223, 1971.
- [10] M. Methfessel, D. Hennig, and M. Scheffler, "Trends of the surface relaxations, surface energies, and work functions of the 4d transition metals," *Phys. Rev. B*, vol. 46, pp. 4816–4829, 1992.
- [11] N. D. Lang, "The Density-Functional Formalism and the Electronic Structure of Metal Surfaces," in *Solid State Physics*, vol. 28, H. Ehrenreich, F. Seitz, and D. Turnbull, Eds. Academic Press, 1974, pp. 225–300.
- [12] J. Bardeen, "Theory of the Work Function II. The Surface Double Layer," *Phys. Rev.*, vol. 49, pp. 653–663, 1936.
- [13] S. Trasatti, "The Concept and Physical Meaning of Absolute Electrode Potential," *J. Electroanal. Chem.*, vol. 139, pp. 1–13, 1982.
- [14] H. L. Lord, W. Zhan, and J. Pawliszyn, *Fundamentals and applications of needle trap devices*, vol. 2. New York: John Wiley and Sons, 2012.
- [15] H. Reiss and A. Heller, "The Absolute Potential of the Standard Hydrogen Electrode: A New Estimate," *J. Phys. Chem.*, vol. 89, pp. 4207–4213, 1985.
- [16] R. W. Ramette, "Outmoded Terminology: The Normal Hydrogen Electrode," *Textb. forum*, vol. 64, p. 885, 1987.
- [17] H. Helmholtz, "Ueber einige Gesetze der Vertheilung elektrischer Ströme in körperlichen Leitern mit Anwendung auf die thierisch-elektrischen Versuche," *Ann. Phys. Chem.*, vol. 165, pp. 353–377, 1853.
- [18] L. G. Gouy, "Sur la Constitution de la Charge Electrique a la Surface d'un

- Electrolyte," *J. Phys. Theor. Appl*, vol. 9, pp. 457–468, 1910.
- [19] D. L. Chapman, "LI. A contribution to the theory of electrocapillarity," *Philos. Mag. Ser. 6*, vol. 25, pp. 475–481, 1913.
- [20] O. Stern, "Zur Theorie der Elektrolytischen Doppelschicht," *Berichte der Bunsengesellschaft für Phys. Chemie*, vol. 30, pp. 508–516, 1924.
- [21] M. Ciobanu, J. P. Wilburn, M. L. Krim, and D. E. Cliffler, "Fundamentals," in *Handbook of Electrochemistry*, 1st ed., C. G. Zoski, Ed. Amsterdam, Oxford: Elsevier, 2007, pp. 01–30.
- [22] D. C. Grahame, "The Electrical Double Layer and the Theory of Electrocapillarity," *Chem. Rev.*, vol. 41, pp. 441–501, 1947.
- [23] M. V. Fedorov and A. A. Kornyshev, "Ionic Liquids at Electrified Interfaces," *Chem. Rev.*, vol. 114, pp. 2978–3036, 2014.
- [24] A. A. Kornyshev, "Double-Layer in Ionic Liquids: Paradigm Change?," *J. Phys. Chem. B*, vol. 111, pp. 5545–5557, 2007.
- [25] N. Georgi, A. A. Kornyshev, and M. V. Fedorov, "The anatomy of the double layer and capacitance in ionic liquids with anisotropic ions: Electrostriction vs. lattice saturation," *J. Electroanal. Chem.*, vol. 649, pp. 261–267, 2010.
- [26] M. Z. Bazant, B. D. Storey, and A. A. Kornyshev, "Double Layer in Ionic Liquids: Overscreening versus Crowding," *Phys. Rev. Lett.*, vol. 106, pp. 6–9, 2011.
- [27] M. V. Fedorov, N. Georgi, and A. A. Kornyshev, "Double layer in ionic liquids: The nature of the camel shape of capacitance," *Electrochem. commun.*, vol. 12, pp. 296–299, 2010.
- [28] M. V. Fedorov and A. A. Kornyshev, "Towards understanding the structure and capacitance of electrical double layer in ionic liquids," *Electrochim. Acta*, vol. 53, pp. 6835–6840, 2008.
- [29] D. Boda, D. Henderson, K.-Y. Chan, and D. T. Wasan, "Low temperature anomalies in the properties of the electrochemical interface," *Chem. Phys. Lett.*, vol. 308, pp. 473–478, 1999.
- [30] D. Boda and D. Henderson, "The capacitance of the solvent primitive model double layer at low effective temperatures," *J. Chem. Phys.*, vol. 112, pp. 8934–8938, 2000.
- [31] H. Löwen, J.-P. Hansen, and P. A. Madden, "Nonlinear counterion screening in colloidal suspensions," *J. Chem. Phys.*, vol. 98, pp. 3275–3289, 1993.
- [32] P. A. Bopp, A. A. Kornyshev, and G. Sutmann, "Static Nonlocal Dielectric Function of Liquid Water," *Phys. Rev. Lett.*, vol. 76, pp. 1280–1283, 1996.
- [33] L. Cheng, P. Fenter, K. L. Nagy, M. L. Schlegel, and N. C. Sturchio, "Molecular-scale Density Oscillations in Water Adjacent to a Mica Surface.," *Phys. Rev. Lett.*, vol. 87, p. 156103, 2001.
- [34] K. R. Painter, P. Ballone, M. P. Tosi, P. J. Grout, and N. H. March, "Capacitance of Metal-Molten-Salt Interfaces," *Surf. Sci.*, vol. 133, pp. 89–100, 1983.
- [35] M. Mezger, H. Schröder, H. Reichert, S. Schramm, J. S. Okasinski, S. Schröder, V. Honkimäki, M. Deutsch, B. M. Ocko, J. Ralston, M. Rohwerder, M. Stratmann, and H. Dosch, "Molecular Layering of Fluorinated Ionic Liquids at a Charged Sapphire (0001) Surface," *Science*, vol. 322, pp. 424–428, 2008.
- [36] R. Hayes, N. Borisenko, M. K. Tam, P. C. Howlett, F. Endres, and R. Atkin, "Double Layer Structure of Ionic Liquids at the Au(111) Electrode Interface: An Atomic Force Microscopy Investigation," *J. Phys. Chem. C*, vol. 115, pp. 6855–6863, 2011.

- [37] M. V. Fedorov and A. A. Kornyshev, "Ionic Liquid Near a Charged Wall: Structure and Capacitance of Electrical Double Layer," *J. Phys. Chem. B Lett.*, vol. 112, pp. 11868–11872, 2008.
- [38] A. M. Smith, K. R. J. Lovelock, N. N. Gosvami, P. Licence, A. Dolan, T. Welton, and S. Perkin, "Monolayer to Bilayer Structural Transition in Confined Pyrrolidinium-Based Ionic Liquids," *J. Phys. Chem. Lett.*, vol. 4, pp. 378–382, 2013.
- [39] M. M. Islam, M. T. Alam, T. Okajima, and T. Ohsaka, "Electrical Double Layer Structure in Ionic Liquids: An Understanding of the Unusual Capacitance-Potential Curve at a Nonmetallic Electrode," *J. Phys. Chem. C Lett.*, vol. 113, pp. 3386–3389, 2009.
- [40] Y. Z. Su, Y. C. Fu, J. W. Yon, Z. Bin Chen, and B. W. Mao, "Double Layer of Au(100)/Ionic Liquid Interface and Its Stability in Imidazolium-Based Ionic Liquid," *Angew. Chemie - Int. Ed.*, vol. 48, pp. 5148–5151, 2009.
- [41] W. Schmickler and W. Vielstich, "ELECTRON TRANSFER RATES IN THE LEVICH AND DOGONADZE THEORY OF REDOX REACTIONS," *Electrochim. Acta*, vol. 18, pp. 883–888, 1973.
- [42] V. G. Levich, R. R. Dogonadze, E. D. German, A. M. Kuznezov, and Y. I. Kharkats, "Theory of homogeneous reactions involving proton transfer," *Electrochim. Acta*, vol. 15, pp. 353–367, 1970.
- [43] V. G. Levich, "Present state of the theory of oxidation reduction in solution (bulk and electrode reactions)," *Adv. Electrochem. Electrochem. Eng.*, vol. 4, pp. 249–371, 1966.
- [44] R. A. Marcus, "Exchange Reactions and Electron Transfer Reactions Including Isotopic Exchange - Theory of Oxidation-Reduction Reactions Involving Electron Transfer," *Discuss. Faraday Soc.*, vol. 29, pp. 21–31, 1960.
- [45] H. Gerischer, "Kinetik der elektrolytischen abscheidung und auflösung von metallen in wässriger lösung," *Electrochim. Acta*, vol. 2, pp. 1–18, 1960.
- [46] J. Franck, "Elementary Processes of Photochemical Reactions," *Trans. Faraday Soc.*, vol. 21, p. 536, 1926.
- [47] E. Condon, "A Theory of Intensity Distribution in Band Systems," *Phys. Rev.*, vol. 28, pp. 1182–1201, 1926.
- [48] K. J. Vetter, *Elektrochemische Kinetik*, 1st ed. Berlin, Heidelberg: Springer-Verlag, 1967.
- [49] A. J. Bard, R. Parsons, and J. Jordan, *Standard Potentials in Aqueous Solution*. New York, Basel: CRC Press, 1985.
- [50] U. Retter and H. Lohse, "Electrochemical Impedance Spectroscopy," in *Electroanalytical Methods*, F. Scholz, Ed. Berlin, Heidelberg: Springer-Verlag, 2005, pp. 149–166.
- [51] J. Friedl, C. M. Bauer, A. Rinaldi, and U. Stimming, "Electron transfer kinetics of the  $VO^{2+} / VO_2^+$  - Reaction on multi-walled carbon nanotubes," *Carbon N. Y.*, vol. 63, pp. 228–239, 2013.
- [52] C. J. Brug, A. L. G. van den Eeden, M. Sluyters-Rehbach, and J. H. Sluyters, "The Analysis of Electrode Impedances Complicated by the Presence of a Constant Phase Element," *J. Electroanal. Chem.*, vol. 176, pp. 275–295, 1984.
- [53] M. Razavy, *Quantum Theory of Tunneling*. Singapore: World Scientific Publishing Co. Pte. Ltd, 2003.
- [54] S. Badger, "Novel SPM imaging modes: Torsional resonance mode imaging and

- scanning electrochemical potential microscopy,” in *Excerpt from the Proceedings of Scanning Probe Microscopy 2004 Nizhny Novgorod*, 2004, pp. 19–23.
- [55] D. Woo, J. Yoo, S. Park, I. C. Jeon, and H. Kang, “Direct Probing into the Electrochemical Interface Using a Novel Potential Probe : Au ( 111 ) Electrode / NaBF<sub>4</sub> Solution Interface,” *Bull. Korean Chem. Soc.*, vol. 25, pp. 577–580, 2004.
- [56] C. Hurth, C. Li, and A. J. Bard, “Direct probing of electrical double layers by scanning electrochemical potential microscopy,” *J. Phys. Chem. C*, vol. 111, pp. 4620–4627, 2007.
- [57] Y. H. Yoon, D. H. Woo, T. Shin, T. D. Chung, and H. Kang, “Real-space investigation of electrical double layers. Potential gradient measurement with a nanometer potential probe,” *J. Phys. Chem. C*, vol. 115, no. 35, pp. 17384–17391, 2011.
- [58] C. Corbella, E. Pascual, G. Oncins, C. Canal, J. L. Andújar, and E. Bertran, “Composition and morphology of metal-containing diamond-like carbon films obtained by reactive magnetron sputtering,” *Thin Solid Films*, vol. 482, no. 1–2, pp. 293–298, 2005.
- [59] C. Baier and U. Stimming, “Imaging single enzyme molecules under in situ conditions,” *Angew. Chemie - Int. Ed.*, vol. 48, pp. 5542–5544, 2009.
- [60] H. Wolfschmidt, C. Baier, S. Gsell, M. Fischer, M. Schreck, and U. Stimming, “STM, SECPM, AFM and electrochemistry on single crystalline surfaces,” *Materials (Basel)*, vol. 3, pp. 4196–4213, 2010.
- [61] C. Traunsteiner, K. Tu, and J. Kunze-Liebhäuser, “High-Resolution Imaging of the Initial Stages of Oxidation of Cu(111) with Scanning Electrochemical Potential Microscopy,” *ChemElectroChem*, vol. 2, pp. 77–84, 2015.
- [62] R. F. Hamou, P. U. Biedermann, M. Rohwerder, and A. T. Blumeneau, “FEM Simulation of the Scanning Electrochemical Potential Microscopy ( SECPM ),” in *Excerpt from the Proceedings of the COMSOL Conference 2008 Hannover*, 2008, pp. 1–6.
- [63] R. F. Hamou, P. U. Biedermann, A. Erbe, and M. Rohwerder, “Screening Effects in Probing the Electric Double Layer by Scanning Electrochemical Potential Microscopy (SECPM),” in *Excerpt from the Proceedings of the COMSOL Conference 2009 Milan*, 2009, pp. 1–5.
- [64] R. F. Hamou, P. U. Biedermann, A. Erbe, and M. Rohwerder, “Numerical simulation of probing the electric double layer by scanning electrochemical potential microscopy,” *Electrochim. Acta*, vol. 55, pp. 5210–5222, 2010.
- [65] R. F. Hamou, P. U. Biedermann, A. Erbe, and M. Rohwerder, “Numerical analysis of Debye screening effect in electrode surface potential mapping by scanning electrochemical potential microscopy,” *Electrochem. commun.*, vol. 12, pp. 1391–1394, 2010.
- [66] E. J. F. Dickinson and R. G. Compton, “Diffuse Double Layer at Nanoelectrodes,” *J. Phys. Chem. C*, vol. 113, pp. 17585–17589, 2009.
- [67] *MultiMode 8 Instruction Manual -B (004-1033-000)*. Bruker Corporation, 2004.
- [68] K. E. Johnson, “What’ s an Ionic Liquid?,” *Electrochem. Soc. Interface*, vol. Spring 2007, pp. 38–41, 2007.
- [69] M. Galinski, A. Lewandowski, and I. Stepniak, “Ionic liquids as electrolytes,” *Electrochim. Acta*, vol. 51, pp. 5567–5580, 2006.
- [70] R. D. Rogers and K. R. Seddon, “Ionic Liquids - Solvents of the Future?,” *Science*, vol. 302, pp. 792–793, 2003.

- [71] M. Armand, F. Endres, D. R. MacFarlane, H. Ohno, and B. Scrosati, "Ionic-liquid materials for the electrochemical challenges of the future.," *Nat. Mater.*, vol. 8, pp. 621–629, 2009.
- [72] P. Walden, "Molecular weights and electrical conductivity of several fused salts," *Bull. Russ. Acad. Sci.*, vol. 1800, pp. 405–422, 1914.
- [73] C. Graenacher, "Cellulose Solution," 1,943,176, 1934.
- [74] R. J. Gale, B. Gilbert, and R. A. Osteryoung, "Raman spectra of molten aluminum chloride: 1-butylpyridinium chloride systems at ambient temperatures," *Inorg. Chem.*, vol. 17, pp. 2728–2729, 1978.
- [75] D. Appleby, C. L. Hussey, K. R. Seddon, and J. E. Turp, "Room-temperature ionic liquids as solvents for electronic absorption spectroscopy of halide complexes," *Nature*, vol. 324, pp. 614–616, 1986.
- [76] M. Yoshizawa, W. Xu, and C. A. Angell, "Ionic Liquids by Proton Transfer: Vapor Pressure, Conductivity, and the Relevance of  $\Delta pK_a$  from Aqueous Solutions," *J. Am. Chem. Soc.*, vol. 125, pp. 15411–15419, 2003.
- [77] C. Müller, K. Németh, S. Vesztergom, T. Pajkossy, and T. Jacob, "The interface between HOPG and 1-butyl-3-methyl-imidazolium hexafluorophosphate," *Phys. Chem. Chem. Phys.*, vol. 18, pp. 916–925, 2016.
- [78] A. Lewandowski and A. Świdarska-Mocek, "Ionic liquids as electrolytes for Li-ion batteries-An overview of electrochemical studies," *J. Power Sources*, vol. 194, pp. 601–609, 2009.
- [79] M. T. Pope and A. Müller, "Introduction to Polyoxometalate Chemistry : From Topology via Self- Assembly to Applications," in *Polyoxometalate Chemistry From Topology via Self-Assembly to Applications*, M. T. Pope and A. Müller, Eds. New York, Boston, Dordrecht, London, Moscow: Kluwer Academic Publishers, 2002, pp. 1–6.
- [80] M. Ammam, "Polyoxometalates: formation, structures, principal properties, main deposition methods and application in sensing," *J. Mater. Chem. A*, vol. 1, pp. 6291–6312, 2013.
- [81] A. Müller, E. Krickemeyer, J. Meyer, H. Bögge, F. Peters, W. Plass, E. Diemann, S. Dillinger, F. Nonnenbruch, M. Randerath, and C. Menke, "[ $\text{Mo}_{154}(\text{NO})_{14}\text{O}_{420}(\text{OH})_{28}(\text{H}_2\text{O})_{70}]^{(25\pm 5)-}$ ]: A Water-Soluble Big Wheel with More than 700 Atoms and a Relative Molecular Mass of About 24000," *Angew. Chemie Int. Ed. English*, vol. 34, pp. 2122–2124, 1995.
- [82] A. Müller, E. Beckmann, H. Bögge, M. Schmidtman, and A. Dress, "Inorganic Chemistry Goes Protein Size:  $\text{AMo}_{368}$  Nano-Hedgehog Initiating Nanochemistry by Symmetry Breaking," *Angew. Chemie Int. Ed.*, vol. 41, pp. 1162–1167, 2002.
- [83] J. Berzelius, "The preparation of phosphomolybdate ion [ $\text{PMo}_{12}\text{O}_{40}$ ] $^{3-}$ ," *Ann. Phys. Chem.*, vol. 82, pp. 800–804, 1826.
- [84] A. Rosenheim and O. Liebknecht, "Zur Kenntniss der Jodsäure und Ueberjodsäure," *Justus Liebigs Ann. Chem.*, vol. 3, p. 5, 1899.
- [85] J. F. Keggin, "Structure of the Molecule of 12-Phosphotungstic Acid," *Nature*, vol. 131, pp. 908–909, 1933.
- [86] W. G. Klemperer, "Keggin Structure," 2007. [Online]. Available: [https://en.wikipedia.org/wiki/Keggin\\_structure#/media/File:Anion2.png](https://en.wikipedia.org/wiki/Keggin_structure#/media/File:Anion2.png). [Accessed: 31-Oct-2017].
- [87] M. T. Pope, *Heteropoly and Isopoly Oxometalates*. Berlin, Heidelberg: Springer-

- Verlag, 1983.
- [88] L. C. W. Baker, V. S. Baker, K. Eriks, M. T. Pope, M. S. Orville, W. Rollins, J. H. Fang, and L. L. Koh, "A new general structural category of heteropolyelectrolytes. Unusual magnetic and thermal contraction phenomena," *J. Am. Chem. Soc.*, vol. 88, pp. 2329–2331, 1966.
- [89] U. Kortz, "Polyoxometalates," *Eur. J. Inorg. Chem.*, vol. 2009, p. 5056, 2009.
- [90] J. Friedl, "Advanced Materials for Redox Flow Batteries," PhD thesis, Technische Universität München, 2014.
- [91] R. L. McCreery, "Advanced Carbon Electrode Materials for Molecular Electrochemistry," *Chem. Rev.*, vol. 108, pp. 2646–2687, 2008.
- [92] N. F. Graves, A. W. Moore, and S. L. Strong, "9th Biennial Conference of the American Carbon Society," in *Structure, Properties and Applications of Highly Oriented Graphite*, 1969.
- [93] AIST-NT SPM accessories, "HOPG." [Online]. Available: [http://nanoprobes.aist-nt.com/apps/HOPG info.htm](http://nanoprobes.aist-nt.com/apps/HOPG%20info.htm). [Accessed: 05-Jul-2016].
- [94] P. Batra, N. Garcia, H. Rohrer, H. Salemk, E. Stoll, and S. Ciraci, "A Study of Graphite Surface with STM and Electronic Structure Calculations," *Surf. Sci.*, vol. 181, pp. 126–138, 1987.
- [95] L. Kibler, "Preparation and Characterization of Noble Metal Single Crystal Electrode Surfaces," Review of Dissertations, University of Ulm, 2003.
- [96] Kittel, *Introduction to Solid State Physics*, 8th ed. New Jersey: Wiley, 2004.
- [97] J. V. Barth, H. Brune, G. Ertl, and R. J. Behm, "Scanning tunneling microscopy observations on the reconstructed Au(111) surface: Atomic structure, long-range superstructure, rotational domains, and surface defects," *Phys. Rev. B*, vol. 42, pp. 9307–9318, 1990.
- [98] T. Michely and G. Comsa, "Temperature dependence of the sputtering morphology of Pt ( 111 )," *Surf. Sci.*, vol. 256, pp. 217–226, 1991.
- [99] F. Hanke and J. Björk, "Structure and local reactivity of the Au(111) surface reconstruction," *Phys. Rev. B*, vol. 15, pp. 1497–508, 2013.
- [100] Y. Hasegawa and P. Avouris, "Manipulation of the reconstruction of the Au (111) surface with the STM," *Science*, vol. 258, pp. 1763–1765, 1992.
- [101] O. M. Magnussen, J. Hageböck, J. Hotlos, and R. J. Behm, "In situ scanning tunnelling microscopy observations of a disorder-order phase transition in hydrogensulfate adlayers on Au(111)," *Faraday Discuss.*, vol. 94, p. 329, 1992.
- [102] J. Wang, B. M. Ocko, A. J. Davenport, and H. S. Isaacs, "In situ x-ray-diffraction and -reflectivity studies of the Au(111)/electrolyte interface: Reconstruction and anion adsorption," *Phys. Rev. B*, vol. 46, pp. 10321–10338, 1992.
- [103] J. Friedl, I. Markovits, M. Herpich, G. Feng, A. A. Kornyshev, and U. Stimming, "Interface between a single crystal and an ionic liquid: The influence of water on the double layer capacitance - in preparation," *ChemElectroChem*, no. 111, 2016.
- [104] C. Baier, "Electron Transfer Phenomena in Interfacial Bioelectrochemistry," PhD thesis, Technische Universität München, 2010.
- [105] P. Fenter and S. S. Lee, "Hydration layer structure at solid–water interfaces," *MRS Bull.*, vol. 39, pp. 1056–1061, 2014.
- [106] J. O. Bockris and A. Gonzalez-Martin, "The Advancing Frontier in the Knowledge of the Structure of Interphases," in *Spectroscopic and Diffraction Techniques in Interfacial Electrochemistry*, C. Gutierrez and C. Melendres, Eds. Dordrecht:

- Springer, 1990, pp. 1–54.
- [107] M. Ito, “Structures of water at electrified interfaces: Microscopic understanding of electrode potential in electric double layers on electrode surfaces,” *Surf. Sci. Rep.*, vol. 63, pp. 329–389, 2008.
- [108] E. M. Stuve, “Ionization of water in interfacial electric fields: An electrochemical view,” *Chem. Phys. Lett.*, vol. 519–520, pp. 1–17, 2012.
- [109] M. A. Gebbie, M. Valtiner, X. Banquy, E. T. Fox, W. A. Henderson, and J. N. Israelachvili, “Ionic liquids behave as dilute electrolyte solutions,” *Proc. Natl. Acad. Sci.*, vol. 110, pp. 9674–9679, 2013.
- [110] A. A. Lee, C. S. Perez-Martinez, A. M. Smith, and S. Perkin, “Underscreening in concentrated electrolytes,” *Faraday Discuss.*, vol. 199, pp. 239–259, 2017.
- [111] Z. A. H. Goodwin and A. A. Kornyshev, “Underscreening, overscreening and double-layer capacitance,” *Electrochem. commun.*, vol. 82, pp. 129–133, 2017.
- [112] M. Gnahn, T. Pajkossy, and D. M. Kolb, “The interface between Au(111) and an ionic liquid,” *Electrochim. Acta*, vol. 55, pp. 6212–6217, 2010.
- [113] J. Friedl, I. I. E. Markovits, M. Herpich, G. Feng, A. A. Kornyshev, and U. Stimming, “Interface between an Au(111) surface and an ionic liquid: The influence of water on the double layer capacitance,” *ChemElectroChem*, 2016.
- [114] K. R. Seddon, A. Stark, and M.-J. Torres, “Influence of chloride, water, and organic solvents on the physical properties of ionic liquids,” *Pure Appl. Chem.*, vol. 72, pp. 2275–2287, 2000.
- [115] A. M. O’Mahony, D. S. Silvester, L. Aldous, C. Hardacre, and R. G. Compton, “Effect of Water on the Electrochemical Window and Potential Limits of Room-Temperature Ionic Liquids,” *J. Chem. Eng. Data*, vol. 53, pp. 2884–2891, 2008.
- [116] J. L. Anthony, E. J. Maginn, and J. F. Brennecke, “Solution Thermodynamics of Imidazolium-Based Ionic Liquids and Water,” *J. Phys. Chem. B*, vol. 105, pp. 10942–10949, 2001.
- [117] S. Baldelli, “Influence of water on the orientation of cations at the surface of a room-temperature ionic liquid: a sum frequency generation vibrational spectroscopic study,” *J. Phys. Chem. B*, vol. 107, pp. 6148–6152, 2003.
- [118] S. Rivera-Rubero and S. Baldelli, “Influence of Water on the Surface of Hydrophilic and Hydrophobic Room-Temperature Ionic Liquids,” *J. Am. Chem. Soc. Commun.*, vol. 126, pp. 11788–11789, 2004.
- [119] L. P. N. Rebelo, V. Najdanovic-Visak, Z. P. Visak, M. Nunes da Ponte, J. Szydłowski, C. A. Cerdeiriña, J. Troncoso, L. Román, J. M. S. S. Esperanza, H. J. R. Guedes, and H. C. de Sousa, “A detailed thermodynamic analysis of [C4mim][BF4] + water as a case study to model ionic liquid aqueous solutions,” *Green Chem.*, vol. 6, p. 369, 2004.
- [120] L. Cammarata, S. G. Kazarian, P. A. Salter, and T. Welton, “Molecular states of water in room temperature ionic liquids,” *Phys. Chem. Chem. Phys.*, vol. 3, pp. 5192–5200, 2001.
- [121] N. Sieffert and G. Wipff, “The BMI Tf2N ionic liquid/water binary system: A molecular dynamics study of phase separation and of the liquid-liquid interface,” *J. Phys. Chem. B*, vol. 110, pp. 13076–13085, 2006.
- [122] M. Moreno, F. Castiglione, A. Mele, C. Pasqui, and G. Raos, “Interaction of water with the model ionic liquid [bmim][BF4]: Molecular dynamics simulations and comparison with NMR data,” *J. Phys. Chem. B*, vol. 112, pp. 7826–7836, 2008.

- [123] R. Hayes, S. Imberti, G. G. Warr, and R. Atkin, "How water dissolves in protic ionic liquids," *Angew. Chemie - Int. Ed.*, vol. 51, pp. 7468–7471, 2012.
- [124] W. Jiang, Y. Wang, and G. A. Voth, "Molecular dynamics simulation of nanostructural organization in ionic liquid/water mixtures," *J. Phys. Chem. B*, vol. 111, pp. 4812–4818, 2007.
- [125] Y. Jeon, J. Sung, D. Kim, C. Seo, H. Cheong, Y. Ouchi, R. Ozawa, and H. Hamaguchi, "Structural Change of 1- Butyl- 3- methylimidazolium Tetrafluoroborate + Water Mixtures Studied by Infrared Vibrational Spectroscopy," *J. Phys. Chem. B*, vol. 112, p. 923, 2008.
- [126] G. Feng, X. Jiang, R. Qiao, and A. A. Kornyshev, "Water in Ionic Liquids at Electrified Interfaces : The Anatomy of Electrosorption," *ACS Nano*, vol. 8, pp. 11685–11694, 2014.
- [127] Y. A. Budkov, A. L. Kolesnikov, and M. G. Kiselev, "On the theory of electric double layer with explicit account of a polarizable co-solvent," *J. Chem. Phys.*, vol. 144, pp. 184703-1-184703–8, 2016.
- [128] E. Gongadze and A. Iglič, "Asymmetric size of ions and orientational ordering of water dipoles in electric double layer model - an analytical mean-field approach," *Electrochim. Acta*, vol. 178, pp. 541–545, 2015.
- [129] K. Motobayashi and M. Osawa, "Potential-dependent condensation of Water at the Interface between ionic liquid [BMIM][TfSA] and an Au electrode," *Electrochem. commun.*, vol. 65, pp. 14–17, 2016.
- [130] Y. Zhong, J. Yan, M. Li, L. Chen, and B. Mao, "Electric Double Layer in Ionic Liquid Incorporated with Water Molecules: An AFM Force Curve Study," *ChemElectroChem*, vol. 3, pp. 1–7, 2016.
- [131] M. T. Alam, M. M. Islam, T. Okajima, and T. Ohsaka, "Measurements of differential capacitance in room temperature ionic liquid at mercury, glassy carbon and gold electrode interfaces," *Electrochem. commun.*, vol. 9, pp. 2370–2374, 2007.
- [132] F. Silva, C. Gomes, M. Figueiredo, R. Costa, A. Martins, and C. M. Pereira, "The electrical double layer at the [BMIM][PF6] ionic liquid/electrode interface - Effect of temperature on the differential capacitance," *J. Electroanal. Chem.*, vol. 622, pp. 153–160, 2008.
- [133] R. Atkin, N. Borisenko, M. Drüschler, F. Endres, R. Hayes, B. Huber, and B. Roling, "Structure and dynamics of the interfacial layer between ionic liquids and electrode materials," *J. Mol. Liq.*, vol. 192, pp. 44–54, 2014.
- [134] R. P. Swatloski, J. D. Holbrey, and R. D. Rogers, "Ionic liquids are not always green: hydrolysis of 1-butyl-3-methylimidazolium hexafluorophosphate," *Green Chem.*, vol. 5, p. 361, 2003.
- [135] B. Hirschorn, M. E. Orazem, B. Tribollet, V. Vivier, I. Frateur, and M. Musiani, "Determination of effective capacitance and film thickness from constant-phase-element parameters," *Electrochim. Acta*, vol. 55, pp. 6218–6227, 2010.
- [136] S. Eisele, M. Schwarz, B. Speiser, and C. Tittel, "Diffusion coefficient of ferrocene in 1-butyl-3-methylimidazolium tetrafluoroborate - concentration dependence and solvent purity," *Electrochim. Acta*, vol. 51, pp. 5304–5306, 2006.
- [137] L. G. Lin, Y. Wang, J. W. Yan, Y. Z. Yuan, J. Xiang, and B. W. Mao, "An in situ STM study on the long-range surface restructuring of Au(111) in a non-chloroaluminated ionic liquid," *Electrochem. commun.*, vol. 5, pp. 995–999,

- 2003.
- [138] Q. Guo, F. Yin, and R. E. Palmer, "Beyond the herringbone reconstruction: Magic gold fingers," *Small*, vol. 1, pp. 76–79, 2005.
- [139] F. Yin, R. Palmer, and Q. Guo, "Nanoscale surface recrystallization driven by localized electric field," *Phys. Rev. B*, vol. 73, pp. 73405-1-73405-4, 2006.
- [140] A. A. Kornyshev and I. Vilfan, "Phase Transitions at the Electrochemical Interface," *Electrochim. Acta*, vol. 40, pp. 109–127, 1995.
- [141] R. Atkin, N. Borisenko, M. Drüscher, S. Z. El-Abedin, F. Endres, R. Hayes, B. Huber, and B. Roling, "An in situ STM/AFM and impedance spectroscopy study of the extremely pure 1-butyl-1-methylpyrrolidinium tris(pentafluoroethyl)trifluorophosphate/Au(111) interface: potential dependent solvation layers and the herringbone reconstruction.," *Phys. Chem. Chem. Phys.*, vol. 13, pp. 6849–6857, 2011.
- [142] A. A. Kornyshev, "Correction to 'Double-layer in ionic liquids: Paradigm change?,'" *J. Phys. Chem. B*, vol. 111, pp. 5545–5557, 2007.
- [143] V. Ruiz, J. Suárez-Guevara, and P. Gomez-Romero, "Hybrid electrodes based on polyoxometalate-carbon materials for electrochemical supercapacitors," *Electrochem. commun.*, vol. 24, pp. 35–38, 2012.
- [144] M. Sadakane and E. Steckhan, "Electrochemical Properties of Polyoxometalates as Electrocatalysts," *Chem. Rev.*, vol. 98, pp. 219–237, 1998.
- [145] M. V. Vasylyev and R. Neumann, "New Heterogeneous Polyoxometalate Based Mesoporous Catalysts for Hydrogen Peroxide Mediated Oxidation Reactions," *J. Am. Chem. Soc.*, vol. 126, pp. 884–890, 2004.
- [146] E. Fontananova, L. Donato, E. Drioli, L. C. Lopez, P. Favia, and R. D'Agostino, "Heterogenization of polyoxometalates on the surface of plasma-modified polymeric membranes," *Chem. Mater.*, vol. 18, pp. 1561–1568, 2006.
- [147] N. Mizuno and M. Misono, "Heterogeneous Catalysis," *Chem. Rev.*, vol. 98, pp. 199–217, 1998.
- [148] B. Keita, L. Nadjo, and K. Kjoller, "Surface characterization of a single crystal of sodium decatungstocerate (IV) by the AFM," *Surf. Sci.*, vol. 256, pp. L613–L617, 1991.
- [149] B. Keita, F. Chauveau, F. Theobald, D. Belanger, and L. Nadjo, "Imaging of sodium decatungstocerate (IV) by scanning tunneling and atomic force microscopy," *Surf. Sci.*, vol. 264, pp. 271–280, 1992.
- [150] B. Keita and L. Nadjo, "High resolution scanning tunneling microscopy imaging of tungstophosphoric acid," *Surf. Sci.*, vol. 254, pp. L443–L447, 1991.
- [151] B. A. Watson, M. A. Barteau, L. Haggerty, A. M. Lenhoff, and R. S. Weber, "Scanning tunneling microscopy and tunneling spectroscopy of ordered hetero- and isopolyanion arrays on graphite," *Langmuir*, vol. 8, pp. 1145–1148, 1992.
- [152] M. S. Kaba, I. K. Song, and M. A. Barteau, "Ordered array formation and negative differential resistance behavior of cation-exchanged heteropoly acids probed by scanning tunneling microscopy," *J. Phys. Chem.*, vol. 100, pp. 19577–19581, 1996.
- [153] M. S. Kaba, I. K. Song, D. C. Duncan, C. L. Hill, and M. A. Barteau, "Molecular Shapes, Orientation, and Packing of Polyoxometalate Arrays Imaged by Scanning Tunneling Microscopy.," *Inorg. Chem.*, vol. 37, pp. 398–406, 1998.
- [154] I. K. Song, R. B. Shnitser, J. J. Cowan, C. L. Hill, and M. A. Barteau, "Nanoscale characterization of redox and acid properties of Keggin-type heteropolyacids by

- scanning tunneling microscopy and tunneling spectroscopy: Effect of heteroatom substitution," *Inorg. Chem.*, vol. 41, pp. 1292–1298, 2002.
- [155] I. K. Song, M. S. Kaba, and M. A. Barteau, "Nanoscale investigation of mixed arrays of Keggin-type and Wells-Dawson-type heteropolyacids (HPAs) by scanning tunneling microscopy (STM)," *Langmuir*, vol. 18, pp. 2358–2362, 2002.
- [156] I. K. Song and M. A. Barteau, "Scanning tunneling microscopy (STM) and tunneling spectroscopy (TS) of heteropolyacid (HPA) self-assembled monolayers (SAMS): connecting nano properties to bulk properties," *Korean J. Chem. Eng.*, vol. 19, no. 4, pp. 567–573, 2002.
- [157] I. K. Song, M. S. Kaba, K. Nomiya, R. G. Finke, and M. A. Barteau, "Scanning tunneling microscopy (STM) and tunneling spectroscopy (TS) studies of polyoxometalates (POMs) of the Wells-Dawson structural class," *J. Mol. Catal. A Chem.*, vol. 262, pp. 216–226, 2007.
- [158] B. Keita and L. Nadjo, "Scanning tunnelling microscope monitoring of the surface morphology of the basal plane of highly oriented pyrolytic graphite during the cyclic voltammetry," *J. Electroanal. Chem.*, vol. 354, pp. 295–304, 1993.
- [159] L. Nadjo and B. Keita, "Electrode Surface Modified with Heteropoly or Isopoly-Anions - STM and AFM Characterization," *J. Phys. IV*, vol. 4, pp. 329–336, 1994.
- [160] B. Zhang and E. Wang, "In situ scanning tunnelling microscopy image of a highly oriented pyrolytic graphite electrode modified with potassium bis(11-molybdosilicato) dysprosate(III) in sodium sulphate solution," *J. Electroanal. Chem.*, vol. 388, pp. 207–213, 1995.
- [161] S. Choi and J. Kim, "Adsorption properties of Keggin-type polyoxometalates on carbon based electrode surfaces and their electrocatalytic activities," *Bull. Korean Chem. Soc.*, vol. 30, pp. 810–816, 2009.
- [162] M. S. Alam, V. Dremov, P. Müller, A. V Postnikov, S. S. Mal, F. Hussain, and U. Kortz, "STM / STS Observation of Polyoxoanions on HOPG Surfaces : the Wheel-Shaped  $[\text{Cu}_{20}\text{Cl}(\text{OH})_{24}(\text{H}_2\text{O})_{12}(\text{P}_8\text{W}_{48}\text{O}_{184})]^{25-}$  and the Ball-Shaped  $[\{\text{Sn}(\text{CH}_3)_2(\text{H}_2\text{O})\}_{24}\{\text{Sn}(\text{CH}_3)_2\}_{12}(\text{A}-\text{PW}_9\text{O}_{34})_{12}]^{36-}$ ," *Inorg. Chem.*, vol. 45, pp. 2866–2872, 2006.
- [163] L.-H. Bi, U. Kortz, S. Nellutla, A. O. Stowe, J. van Tol, N. S. Dalal, B. Keita, and L. Nadjo, "Structure , Electrochemistry , and Magnetism of the Iron ( III ) - Substituted Keggin Dimer,  $[\text{Fe}_6(\text{OH})_3(\text{A}-\alpha-\text{GeW}_9\text{O}_{34}(\text{OH})_3)_2]^{11-}$ ," *Inorg. Chem.*, vol. 44, no. 4, pp. 896–903, 2005.
- [164] C. Li, Y. Zhang, K. P. O'Halloran, J. Zhang, and H. Ma, "Electrochemical behavior of vanadium-substituted Keggin-type polyoxometalates in aqueous solution," *J. Appl. Electrochem.*, vol. 39, pp. 421–427, 2009.
- [165] E. Abdeljalil, B. Keita, L. Nadjo, and R. Contant, "STM and AFM characterization of thin metal oxide films electrodeposited from  $[\text{O}_2\text{M}_{18}\text{O}_{62}]^{6-}$ ," *J. Solid State Chem.*, vol. 5, pp. 94–106, 2001.
- [166] V. A. Grigoriev, D. Cheng, C. L. Hill, and I. A. Weinstock, "Role of alkali metal cation size in the energy and rate of electron transfer to solvent-separated 1 : 1  $[(\text{M}^+)(\text{Acceptor})]$  ( $\text{M}^+ = \text{Li}^+, \text{Na}^+, \text{K}^+$ ) ion pairs," *J. Am. Chem. Soc.*, vol. 123, no. 22, pp. 5292–5307, 2001.
- [167] F. Leroy, P. Miró, J. M. Poblet, C. Bo, and J. Bonet Avalos, "Keggin polyoxoanions in aqueous solution: ion pairing and its effect on dynamic properties by molecular dynamics simulations.," *J. Phys. Chem. B*, vol. 112, pp. 8591–8599, 2008.

- [168] S.-S. Wang and G.-Y. Yang, "Recent Advances in Polyoxometalate-Catalyzed Reactions," *Chem. Rev.*, vol. 115, pp. 4893–4962, 2015.
- [169] A. Chaumont and G. Wipff, "Ion aggregation in concentrated aqueous and methanol solutions of polyoxometallates Keggin anions: the effect of counterions investigated by molecular dynamics simulations.," *Phys. Chem. Chem. Phys.*, vol. 10, pp. 6940–6953, 2008.
- [170] A. Chaumont and G. Wipff, "Polyoxometalate Keggin Anions at Aqueous Interfaces with Organic Solvents, Ionic Liquids, and Graphite: A Molecular Dynamics Study," *J. Phys. Chem. C*, vol. 113, pp. 18233–18243, 2009.
- [171] A. Chaumont and G. Wipff, "Interactions Between Keggin Anions in Water: The Higher Their Charge, the Higher Their Condensation? A Simulation Study," *Eur. J. Inorg. Chem.*, vol. 2013, pp. 1835–1853, 2013.
- [172] M. K. Bera, B. Qiao, S. Seifert, B. P. Burton-Pye, M. Olvera de la Cruz, and M. R. Antonio, "Aggregation of Heteropolyanions in Aqueous Solutions Exhibiting Short-Range Attractions and Long-Range Repulsions," *J. Phys. Chem. C*, vol. 120, pp. 1317–1327, 2016.
- [173] M. K. Bera, B. Qiao, S. Seifert, B. P. Burton-Pye, M. Olvera de la Cruz, and M. R. Antonio, "Supporting Information for Aggregation of Heteropolyanions in Aqueous Solutions Exhibiting Short-Range Attractions and Long-Range Repulsions," *J. Phys. Chem. C*, vol. 120, pp. 1317–1327, 2016.
- [174] S. A. Serapian and C. Bo, "Simulating the Favorable Aggregation of Monolacunary Keggin Anions," *J. Phys. Chem. B*, vol. 120, pp. 12959–12971, 2016.
- [175] M. Sadakane and E. Steckhan, "Investigation of the manganese-substituted  $\alpha$ -Keggin-heteropolyanion  $K_6SiW_{11}O_{39}Mn(H_2O)$  by cyclic voltammetry and its application as oxidation catalyst," *J. Mol. Catal. A Chem.*, vol. 114, pp. 221–228, 1996.
- [176] M. Sadakane and E. Steckhan, "Co-solvent Effects on the Redox Potentials of Manganese-substituted  $\alpha$ -Keggin-type Silicon Polyoxotungstate  $K_6SiW_{11}O_{39}Mn(H_2O)$ : First Electrochemical Generation of the Manganese(V) Redox System in an Aqueous Environment," *Acta Chem. Scand.*, vol. 53, pp. 837–841, 1999.
- [177] B. Keita, L. Nadjo, D. Belanger, C. P. Wilde, and M. Hilaire, "Electrochemical quartz crystal microbalance: evidence for the adsorption of heteropoly and isopoly anions on gold electrodes," *J. Electroanal. Chem.*, vol. 384, pp. 155–169, 1995.
- [178] A. Kuhn and F. C. Anson, "Adsorption of Monolayers of  $P_2Mo_{18}O_{62}^{6-}$  and Deposition of Multiple Layers of  $Os(bpy)_3^{2+}$ - $P_2Mo_{18}O_{62}^{6-}$  on Electrode Surfaces," *Langmuir*, vol. 12, pp. 5481–5488, 1996.
- [179] M. Born, "Volumen und Hydratationswärme der Ionen," *Zeitschrift für Phys.*, vol. 1, pp. 45–48, 1920.
- [180] H. D. Pratt, N. S. Hudak, X. Fang, and T. M. Anderson, "A polyoxometalate flow battery," *J. Power Sources*, vol. 236, pp. 259–264, 2013.
- [181] A. M. Funtikov, U. Stimming, and R. Vogel, "Anion adsorption from sulfuric acid solutions on Pt(111) single crystal electrodes," *J. Electroanal. Chem.*, vol. 428, pp. 147–153, 1997.
- [182] P. Wu, D. Volkmer, B. Bredenkötter, D. G. Kurth, and J. P. Rabe, "Isolated and linear arrays of surfactant-encapsulated polyoxometalate clusters on graphite," *Langmuir*, vol. 24, pp. 2767–2771, 2008.

- [183] G. Raj, C. Swalus, E. Arendt, P. Eloy, M. Devillers, and E. M. Gaigneaux, "Controlling the dispersion of supported polyoxometalate heterogeneous catalysts: Impact of hybridization and the role of hydrophilicity-hydrophobicity balance and supramolecularity," *Beilstein J. Nanotechnol.*, vol. 5, pp. 1749–1759, 2014.
- [184] *Electrochemical SPM Manual*. Bruker Corporation, 2011.

# Appendix

## A1 Abbreviations

AFM	Atomic Force Microscopy/Microscope
BKK	Budkov-Kolesnikov-Kiselev Model
BMP-TFSA	1-Butyl-1-Methyl Pyrrolidinium bis(trifluoromethylsulfonyl)amide
BMP-TFSI	1-Butyl-1-Methylpyrrolidinium Bis(Trifluoromethylsulfonyl)imide
CE	Counter Electrode
CITS	Current Imaging Tunneling Spectroscopy
CPE	Constant Phase Element
CV	Cyclic Voltammetry/Voltammogram
DFT	Density Functional Theory
DI-water	De-ionized Water
DODA	Dimethyldioctadecylammonium
DOS	Density of State
EC-AFM	Electrochemical Atomic Force Microscopy
EC-STM	Electrochemical Scanning Tunneling Microscopy
EDL	Electrochemical Double Layer
EIS	Electrochemical Impedance Spectroscopy
fcc	face centered cubic lattice structure
GC	Glassy Carbon
GC Model	Gouy-Chapman Model
GCS Model	Gouy-Chapman-Stern Model
HOPG	Highly Oriented Pyrolytic Graphite
i gain	Integral Gain
IHP	Inner Helmholtz Plane
IL	Ionic Liquid
MD	Molecular Dynamics
ML	Monolayer
NDR	Negative Differential Resistance
NHE	Normal Hydrogen Electrode
NU	Newcastle University
OCP	Open Circuit Potential
OHP	Outer Helmholtz Plane
p gain	Proportional Gain
POM	Polyoxometalate
PZC	Potential of Zero Charge
RE	Reference Electrode
RTIL	Room Temperature Ionic Liquid

SAXS	Small-Angle X-ray Scattering
SECPM	Scanning Electrochemical Potential Microscopy
SHE	Standard Hydrogen Electrode
SPM	Scanning Probe Microscopy
STM	Scanning Tunneling Microscopy
TM	Tapping Mode
TS	Tunneling Spectroscopy
TUM	Technische Universität München
WE	Working Electrode

## A2 Symbols

In certain cases, one symbol was used for several meanings. This happened when conventions were followed in equations and descriptions. However, the duplicates never occur in a single section to avoid confusion.

$A$	Electrochemically Active Surface Area
$a$	Electrochemical Activity
$c$	Concentration of Species in Solution
$C_{Debye}$	Debye Capacitance
$C_{DL}$	Double Layer Capacitance
$C_{GC}$	Gouy-Chapman Capacitance
$C_H$	Helmholtz Capacitance
$C_{max}$	Maximum Possible Ion Concentration
$d$	Distance between two Objects
$E_a$	Activation Energy
$E_\mu$	Energy of State $\mu$
$e$	Electric Charge of an Electron
$F$	Faraday Constant
$f$	Frequency
$I_0$	Exchange Current
$I_F$	Faradaic Current
$I_{SP}$	Setpoint Current in STM
$I_T$	Tunneling Current
$k$	Decay Coefficient of Wave Function
$k_0$	Electron Transfer Constant
$k_B$	Boltzmann Constant
$M_{\mu\nu}$	Matrix Element
$m$	Mass of Electron
$n$	Charge of Ion Species
$n$	Number of Transferred Electrons
$Ox$	Oxidized Species
$w_{\mu\nu}$	Transition Probability
$Q$	Constant Phase Element
$q$	Electric Charge
$R$	Gas Constant
$R_{CT}$	Charge Transfer Resistance
$Red$	Reduced Species
$R_{Ohm}$	Ohmic Resistance
$r$	Radius
$r$	Microscope Scan Rate

$T$	Absolute Temperature
$T$	Kinetic Energy
$U$	Electrostatic Potential
$U$	Potential Energy
$U_0$	Equilibrium Potential
$U^\theta$	Characteristic Standard Potential of Redox Couple
$U_{bias}$	Bias Voltage in STM
$U_{OCP}$	Potential at Open Circuit
$U_{SP}$	Setpoint Potential
$U_{WE}$	Working Electrode Potential
$V_i$	Electrostatic Potential
$W$	Work Function
$X$	Water Content in IL
$x$	Distance from Electrode
$Z$	Impedance
$\alpha_a$	Anodic Electron Transfer Coefficient
$\alpha_c$	Cathodic Electron Transfer Coefficient
$\chi$	Dipole Barrier
$\chi^2$	Goodness of Fit
$\Delta G_{Born}$	Born energy of solvation
$\Delta U$	Volta Potential Difference
$\varepsilon$	Dielectric Constant
$\varepsilon_*$	High Frequency Dielectric Constant
$\varepsilon_*$	Effective Polarizability of Ionic Liquid
$\varepsilon_0$	Dielectric Permittivity of Free Space
$\varepsilon_r$	Specific Dielectric Constant
$\varphi(z)$	Galvani Potential
$\phi$	Tunnel Barrier Height
$\gamma$	Compacity Parameter
$\hbar$	Planck Constant
$\eta$	Overpotential
$\kappa$	Inverse Debye Length
$\lambda_D$	Debye Length
$\mu_e$	Chemical Potential
$\overline{\mu_e}$	Electrochemical Potential
$\nu$	Sweep Rate of Cyclic Voltammetry
$\nu_{eff}$	Effective Oscillation Frequency
$\nu$	Average Volume of Ion in IL
$\Psi_\mu$	Wave Function of State $\mu$

$\rho$	Density of States
$\sigma_i$	Standard Deviation
$\sigma$	Charge Density

## A3 Publications

1. J. Friedl, R. Al-Oweini, M. Herpich, B. Keita, U. Kortz, and U. Stimming, "Electrochemical studies of tri-manganese substituted Keggin Polyoxoanions," *Electrochim. Acta*, vol. 141, pp. 357–366, 2014.
2. M. Herpich, J. Friedl, and U. Stimming, "Scanning Electrochemical Potential Microscopy (SECPM) and Electrochemical STM (EC-STM)," in *Surface Science Tools for Nanomaterials Characterization*, Berlin, Heidelberg: Springer-Verlag, 2015, pp. 1–67.
3. J. Friedl, I. Markovits, M. Herpich, G. Feng, A. A. Kornyshev, and U. Stimming, "Interface between a single crystal and an ionic liquid: The influence of water on the double layer capacitance", *ChemElectroChem*, no. 111, 2016.
4. M. Herpich, L. Seidl, J. Gu, Y. Liang, O. Schneider, U. Stimming, "Understanding SECPM", in preparation

## A4 Acknowledgements

Before I end this dissertation, I would like to thank all the great people without whom it would not have been possible to achieve all of this.

Firstly, I want to thank my supervisor Prof. Dr. Ulrich Stimming, who guided me throughout my work with his advice and ideas, even when he was on the other side of the world.

The work on the SECPM was a great group effort and I would like to thank Lukas Seidl and Yunchang Liang for hosting me in Munich and doing experiments together, as well as Dr. Jingying Gu for doing the same in Newcastle. And of course, I want to thank all of them and Dr. Oliver Schneider for the countless discussions and Skype meetings to make sense of all the results.

I want to thank Dr. Jochen Friedl and Dr. Iulius Markovits for introducing me to ionic liquids and electrochemical impedance spectroscopy as well as Prof. Dr. Guang Feng and Prof. Dr. Alexei Kornyshev for their contributions to the study.

Special thanks go to Dr. Jochen Friedl for convincing me to go to Singapore in the first place, as well as for helping me with my first steps in electrochemistry and for the fun hours spent in the lab together.

All my colleagues from RP1 and RP7 at TUM CREATE I want to thank for their help with my many questions about chemistry, especially Prof. Dr. Harry Hoster, Dr. Günter Scherer, Dr. Han Yi Chen, Dr. Nicolas Bucher and Dr. Steffen Hartung.

A very big thank you also goes to my parents, who gave me a home and so much more during the final months of my work.

Finally, the most important thank you is for my awesome wife Marina, who believed in me the whole time and supported me with love and patience while being stuck in a cold, foreign country where people speak a very difficult language.

Everyone else who I could not name here in person of course I also want to thank.